Physical, Chemical, & Nano Sciences Center

Research Briefs

2006

Sandia National Laboratories
Albuquerque, New Mexico

A Multiprogram Laboratory

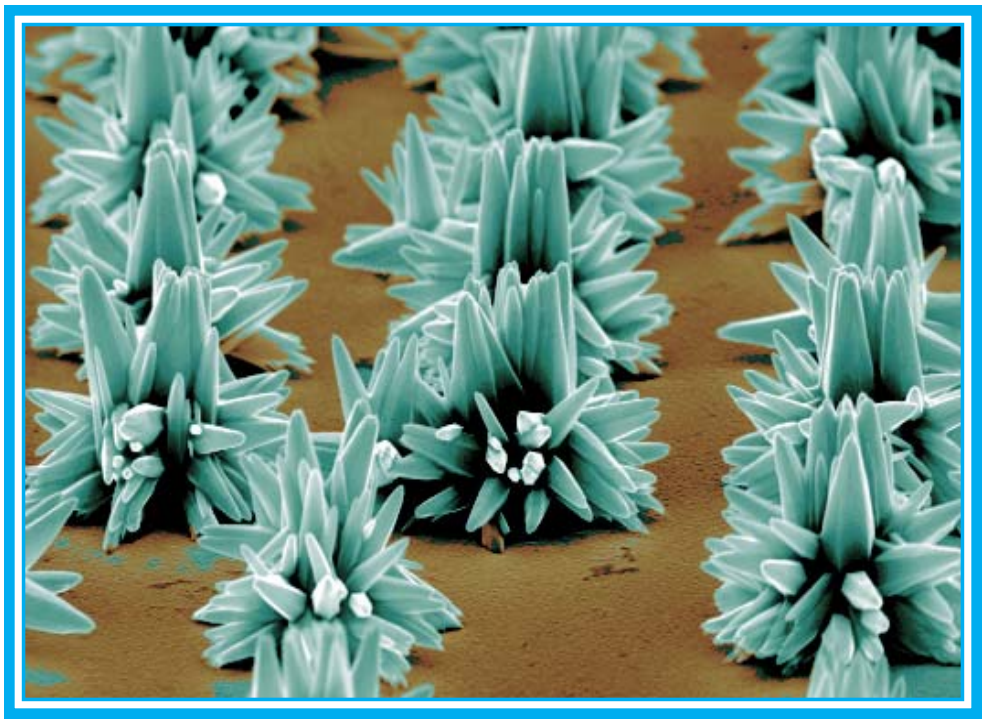

Research Briefs for the Physical, Chemical, & Nano Sciences Center is published by Sandia National Laboratories, a multiprogram laboratory operated by Sandia Corporation, a Lockheed Martin Company, for the United States National Nuclear Security Administration and the Department of Energy under Contract DE-AC04-94AL85000.

Additional complimentary copies are available by contacting:

Julia M. Phillips
Physical, Chemical, & Nano Sciences Center, 1100
Sandia National Laboratories
Albuquerque, NM 87185-1427

Phone: (505) 844-1071
Fax: (505) 844-6098
E-mail: jmphill@sandia.gov
url: http://www.sandia.gov/pcnsc

Research Briefs

Editors
J. M. Phillips
Jerry A. Simmons
Robert Hwang

Production
M. Sheila Wilson

Cover Page: "Complex ZnO nanostructures clustered at 10-micron square lattices." (See page 31.)

Message from the Director

The Physical, Chemical, & Nano Sciences Center creates new scientific knowledge in support of Sandia's mission areas – nuclear weapons; energy, resources, & nonproliferation; defense systems & assessments; and homeland security & defense. We provide science-based solutions for the mission needs of our parent agency, the National Nuclear Security Administration (NNSA), particularly in areas where we have unique expertise. Of equal importance, we also perform focused long-term research in areas that are most likely to have impact on future Sandia missions and national security, particularly in the physical, chemical, and nano sciences that will enable future microsystems. This volume highlights representative research in our areas of emphasis, including Nanoelectronics & Nitride Semiconductors; Nanomaterials; Nanomechanics; Electromagnetic Radiation: Generation, Detection, & Spectroscopy; and Materials in Extreme Environments.

The activities of the Physical, Chemical, & Nano Sciences Center are supported by a diverse set of funding sources that reflect the broad impact of our work, both scientifically and programmatically. The research described in this volume illustrates the importance of a strong science base in the physical, chemical, & nano sciences for the success of the Department of Energy's missions. Throughout this work, we have benefited immeasurably from our partnerships with colleagues across the labs, in universities, and in industry. We gratefully acknowledge their collaboration.

We appreciate your interest in our work and welcome your comments and inquiries.

Julia M. Phillips
Director

Table of Contents

Nanoelectronics & Nitride Semiconductors

Evidence of Bloch Oscillations in Two-dimensional Quantum Dot Arrays (W. Pan, et al.) 6

Analysis of the Quantum-Confined Stark Effect in InGaN Single Quantum Wells (S. R. Lee, et al.) 8

Highly Aligned Arrays of GaN Nanowires Achieved via Selection of Substrate Orientation, Catalyst Concentration, and Growth Temperature (George T. Wang, et al.) 10

Novel AlN Growth Processes for High Performance Deep UV Optoelectronics (A. A. Allerman, et al.) 12

Microwave Dissipation in Carbon Nanotubes and Silicon Nanowires (Mark Lee, et al.) 14

Photoluminescence Dynamics of Broadband Emission from Cadmium Sulfide (CdS) Quantum Dots (J. E. Martin and L. E. Shea-Rohwer) 16

Self-assembled Quantum Dots for Detectors and Emitters in the Long-wavelength Infrared (Jeffrey G. Cederberg and Eric A. Shaner) 18

Nanomaterials

Active Transport of Carbon Nanotubes Using Motor Proteins (B. C. Bunker, et al.) 22

Chain Transfer to a Surface—a Novel Method for Forming Polymer Nanofilms (D. L. Huber and B. C. Bunker) 24

Controlled Growth of Single- and Multi-Wall Carbon Nanotube Arrays (M. Siegal, et al.) 26

Crawler for Microfluidic Systems Based on Switchable Polymers (B. C. Bunker, et al.) 28

Growth, Assembly, and Characterization of Zinc Oxide Nanostructures (J. W. P. Hsu, et al.) . . .30

Porphyrin-Based Nanostructures for Electronic Applications (J. A. Shelnutt, et al.) 32

Oxidation of the Copper (100) Surface Induced by Local Alkalization (N. Vasiljevic, et al.) 34

Nanomechanics

Correlating Atomic Structure and Material Properties in Erbium Tritide (R. R. Wixom and D. R. Jennison) 38

Mechanical Properties of Aging Erbium Tritide Films (J. A. Knapp and J. F. Browning) 40

Dynamical and Mechanical Behavior of Reversible Protein Hydrogels
(Gary S. Grest, et al.) 42

Abnormal Grain-Growth in Nanocrystalline Nickel (D. M. Follstaedt, et al.) 44

Studies of the Nanotribology of Interfacial Water (J. E. Houston, et al.) 46

Electromagnetic Radiation: Generation, Detection, & Spectroscopy

Optical Damage Characterization of Pure and Yb^{3+}-doped Fused Silica
(Arlee V. Smith and Binh T. Do) 50

High Efficiency Ultraviolet Light Generation (D. J. Armstrong & A. V. Smith) 52

Gas-phase Absorption Spectrum of 2, 4 DNT Explosive from 0.05 to 1.5 THz Using THz Time-Domain Spectroscopy (R. Foltynowicz and R. E. Allman) 54

Single Quantum Well THz Split Grating-Gate Detectors (E. A. Shaner) 56

Microelectronic Terahertz Receiver-Transeiver (Mark Lee, et al.) 58

Materials in Extreme Environments

Using Large-Scale Simulations to Advance Understanding of Defects in Silicon
(A. F. Wright and N. A. Modine) 62

Measurements of Defects in Neutron-Irradiated Silicon Bipolar Transistors Using Capacitance Spectroscopy (R. M. Fleming, et al.) 64

Modeling Neutron-Irradiated Transistors—From Atomic Collisions to Carrier Flow
(S. M. Myers and W. R. Wampler) 66

Dielectric Properties of PZT 95/5 During Shock Compression at High Fields
(R. E. Setchell, et al.) 68

Ion Beam Induced (IBIC) Studies of SiGe Heterojunction Bipolar Transistors (HBTs)
(G. Vizkelethy, et al.) 70

The Relaxational Properties and Phase Behavior of $Pb(Sc_{0.5}Ta_{0.5})0_3$
(E. L. Venturini and G. A. Samara) 72

Ion-Neutron Equivalence—Ion Beam Laboratory (IBL) and Los Alamos Neutron Science Center (LANSCE) (E. Bielejec, et al.) 74

Table of Contents Cont'd

Recent Awards & Prizes 78

Government Advisory Boards & Professional Societies 84

Resources & Capabilities 91

Physical, Chemical, & Nano Sciences Center FY06 Budget 97

Nanoelectronics & Nitride Semiconductors

Evidence of Bloch Oscillations in Two-dimensional Quantum Dot Arrays

by **W. Pan, R. G. Dunn, S. K. Lyo, J. L. Reno, and J. A. Simmons**

Motivation—We investigate in this project the physics and device applications of Bloch oscillations (BOs) of electrons, engineered in high mobility quantum wells patterned into two-dimensional quantum dot arrays, i.e. quantum dot superlattices (QDSL). A BO occurs when an electron moves out of the Brillouin zone (BZ) in response to a DC electric field, undergoes Bragg reflection, and consequently, executes oscillating motion. Many efforts have been devoted to understanding and detecting BOs over the years. The main motivation behind this work is its huge potential for novel device applications; the BO frequency can fall into the terahertz (THz) regime when the magnitude of the electric field and the period of QDSL are carefully chosen. From a fundamental science perspective, studying BOs will enable us to probe high frequency many-body quantum dynamics, coherent electron transport, and energy and charge transfer. To date, no direct evidence of BO has ever been observed using electronic transport measurements. The primary reason for this is the fast damping of BOs, caused by strong electron-optical phonon scattering. We tackle this challenge by employing a new device structure, the so-called QDSL, fabricated by an interferometric lithography technique. This project is ambitious and involves both large scale nano patterning and low temperature transport measurements at DC and radio-to-THz frequencies.

Accomplishment—We have carried out current-voltage (I-V) and magnetotransport measurements in QDSL structures. In the non-linear I-V measurements, negative differential conductance (NDC) is observed. In Fig. 1, we show the I-V curve in two different samples of different electron potential modulation strength (3% vs. 15% of the Fermi energy). The observation of NDC is encouraging since it may represent the first step towards the definitive establishment of electron self-oscillations in our 2D quantum dot arrays. To understand the physical origin of NDC, theoretical simulations have been carried out. Assuming Bragg scattering for the 2D electrons at the boundary of the Brillouin zone and a relaxation time approximation, the theoretically obtained I-V curve (red) is shown in Fig. 2. The deviation from experiment at high fields may be due to the neglect of full 2D elastic scattering, or other mechanisms such as 2D domain formation.

In magnetotransport studies, a resistance spike indicative of a resonance is observed. At the present time, we believe that this resonance behavior is caused by the edge magnetoplasmon resonance. In contrast to previous experiments on edge magnetoplasmon resonances, our experiment did not apply external radiation to the quantum dot array samples. The required high frequency radiation, we speculate, is provided by the self-oscillation of electrons (i.e., Bloch oscillation) under large DC electric fields.

This research was done in collaboration with D. Li and S.R.J. Brueck at the CHTM at UNM.

Significance—We demonstrate, for the first time, negative differential conductance and evidence of Bloch oscillations in two-dimensional quantum dot arrays. This could eventually lead to the realization of frequency-tunable, solid-state THz emitters and detectors.

Sponsors for various phases of this work include: DOE Office of Basic Energy Sciences and Laboratory Directed Research & Development

Contact: Wei Pan, Semiconductor Material & Device Sciences, Dept. 1123
Phone: (505) 284-9545 and (505) 844-3178, Fax: (505) 844-3211, E-mail: wpan@sandia.gov

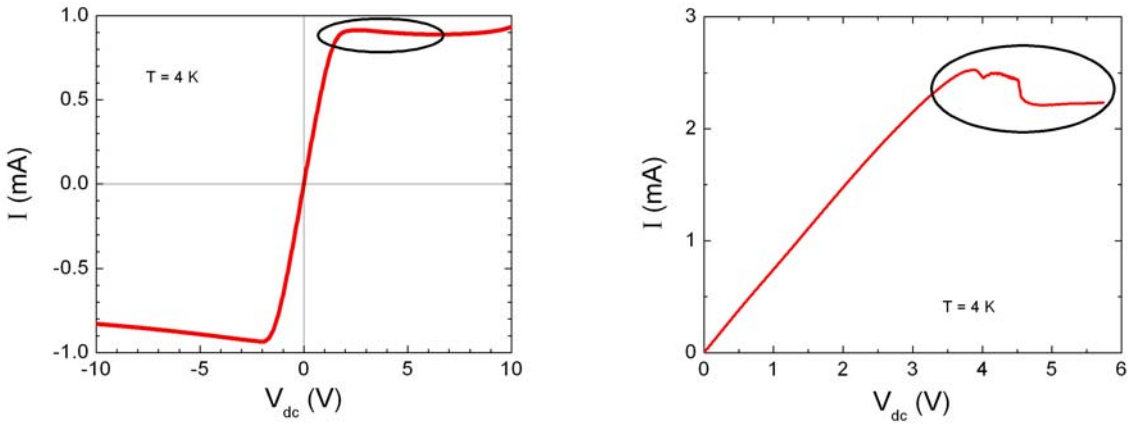

Figure 1. I-V characteristics for two samples of different electron potential modulations; a) 3% and b) 15% of the Fermi energy. In both samples, the negative differential conductance region (highlighted by circle) is seen. Current steps are also observed in the NDC region for the 15% sample. Interestingly, the I-V curve shows different characteristics in two samples. This suggests that the I-V characteristics, and probably the 2D electron dynamics, can be manipulated in a controllable way.

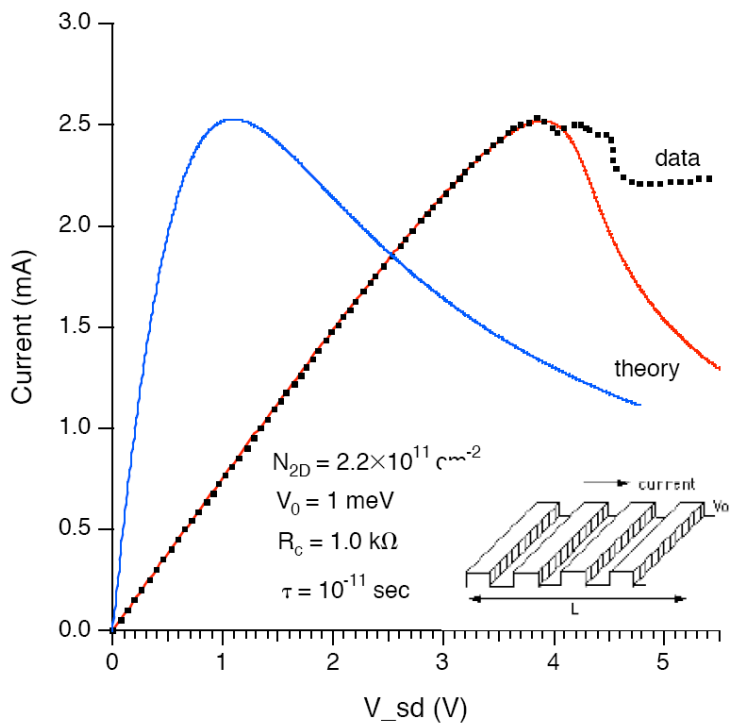

Figure 2. Theoretical result based on a relaxation-time approximation and on a 1D potential modulation, as shown in the inset. Elastic scattering is ignored. Other parameters are chosen according to real samples. The blue curve shows the result assuming no load resistance. The red curve shows the results when a proper load resistance of 1.0 kΩ is taken into account. V_0 = 1 meV corresponds to 15% modulation of the conduction band edge.

Analysis of the Quantum-Confined Stark Effect in InGaN Single Quantum Wells

by **R. J. Kaplar, S. R. Kurtz, D. D. Koleske, and S. R. Lee**

Motivation—The InGaN/GaN quantum well (QW) system has recently attracted much attention due to its central role in the development of green, blue, and ultraviolet optoelectronics. Based on the wurtzite crystal structure, large (MV/cm) polarization-induced electric fields are known to exist in strained InGaN quantum wells grown on the basal plane of GaN; these fields influence optical-device performance by altering the electron and hole wave-function overlap. A number of authors have confirmed the existence of such fields, but reported measurements of the field differ, even for structures of similar indium composition. In general, measured Stark shifts are much smaller than expected from theory, and since InGaN/GaN QW polarization fields have typically been inferred from the measured Stark shifts via band-structure theory, polarization fields are usually underestimated as well.

Accomplishment—The present research resolves these discrepancies using a new approach where QW polarization fields are directly measured by capacitance-voltage (CV) techniques. By combining these direct measurements of the field with standard optical measurements of the QW emission energy, we can compare the dependence of Stark shift on the polarization field to fully independent band-structure theory. These unique comparisons yield new insights into carrier-recombination efficiency in InGaN/GaN QWs.

Here, we examine $In_xGa_{1-x}N$ (x=0.11-0.14) single quantum wells (SQWs) embedded in the n-side of GaN p^+n junctions. Electron density profiles obtained from CV measurements reveal sharp peaks associated with charge storage in the SQWs, with total QW charge consistent with calculated values (Fig. 1). Photocurrent and electroreflectance spectra were separately measured as a function of applied field, and we observe a blue shift due to the quantum-confined Stark effect (Fig. 2). Unlike many prior results where the inferred polarization fields are too small, our direct measurements of the SQW polarization fields show good agreement with Schrödinger-Poisson calculations performed using *ab-initio* values for the polarization. Nonetheless, the presently observed Stark shifts remain much less than predicted, as in the previous studies (Fig. 3 – see ideal model vs experimental data).

By comparing further band-structure calculations to the measured Stark shift versus electric field, we show that *without decreasing the SQW polarization field* a simple model incorporating hole localization in the SQW removes much of the observed Stark-shift discrepancy (Fig. 3 – see localized-hole model vs. experimental data). The operative hole-localization mechanism could arise from indium-rich domains, defect states, or intrinsic hole-wavefunction localization produced by the ionic character of the bonding in wurtzite-structure III-V nitrides.

Significance—If holes are in fact localized, the electron-hole wave-function overlap in InGaN/GaN QWs is larger than currently believed. Thus, improvements in brightness expected from InGaN-QW emitters grown on non-polar GaN may be less than presently anticipated, while emitters grown on the polar basal-plane of GaN may ultimately become more efficient than now thought possible. These new scientific findings alter the pathway forward to energy-efficient solid-state lighting.

Sponsors for various phases of this work include: DOE Office of Basic Energy Sciences and Nuclear Weapons/Science & Technology

Contact: Stephen R. Lee, Semiconductor Material & Device Sciences, Dept. 1123
Phone: (505) 844-7307, Fax: (505) 844-3211, E-mail: srlee@sandia.gov

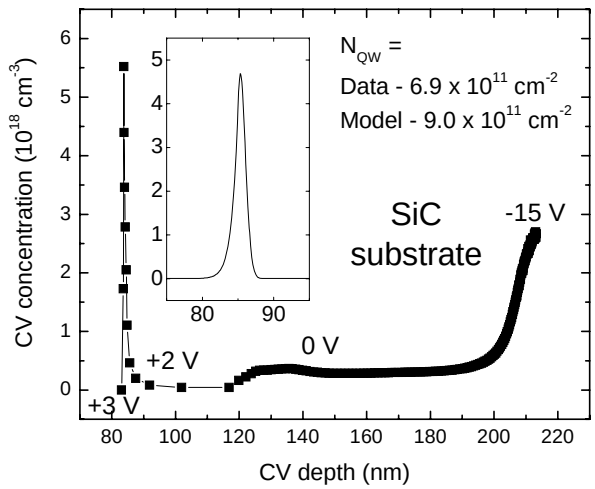

Figure 1. Differential CV measurements of the electron density depth profile and the total integrated QW charge (N_{QW}). The QW is 2.5 nm thick and consists of $In_{0.14}Ga_{0.86}N$. Inset: Calculated electron density profile over the SQW region at +3 V bias. The inset axes have the same units as the main axes.

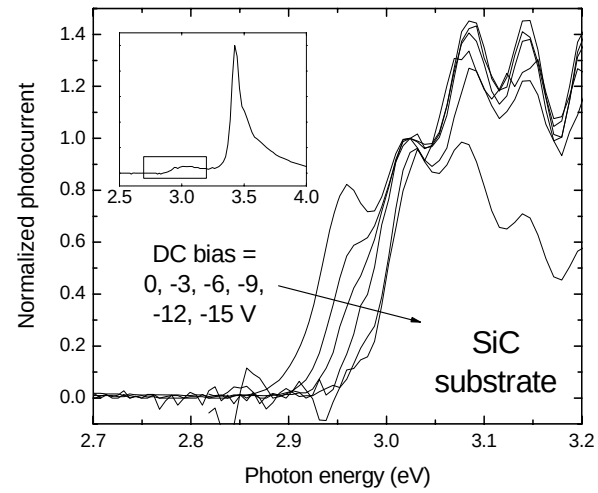

Figure 2. Normalized photocurrent spectra in the vicinity of the SQW absorption edge, measured at 77K using the bias values indicated. The same $In_{0.14}Ga_{0.86}N$ QW as in Fig. 1 is examined. Inset: Zero-bias photocurrent measured over a wide spectral range. The inset axes have the same units as the main axes.

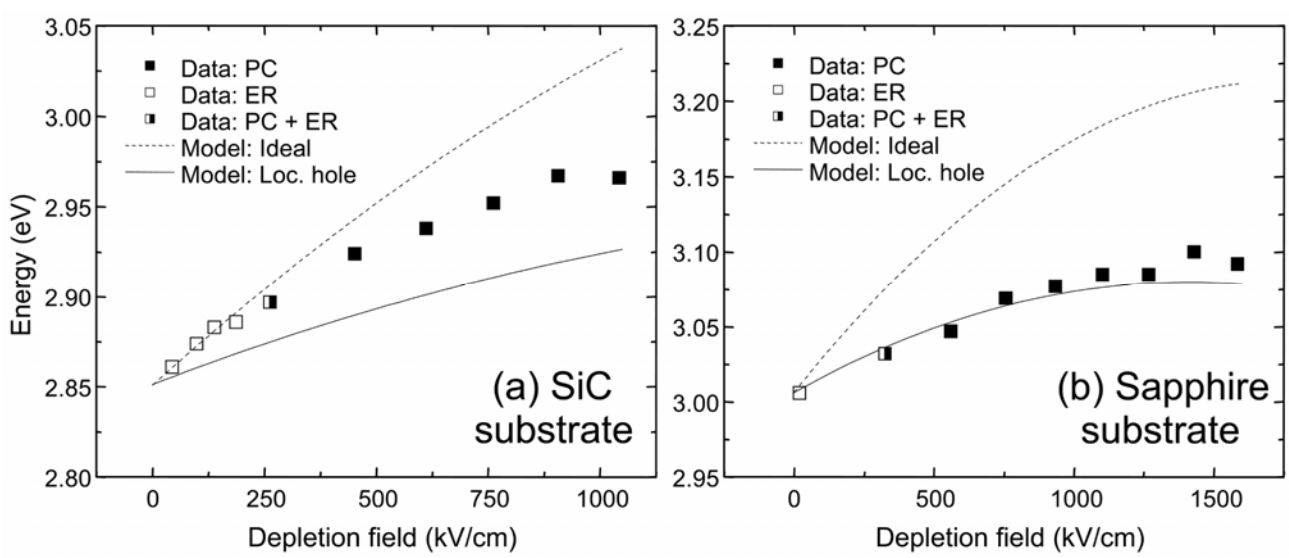

Figure 3. Energy of the SQW absorption edge versus the diode depletion field in the SQW. Solid and open squares indicate experimental points obtained from photocurrent (PC) and electroreflectance (ER), respectively. Smooth curves show the theoretical Stark shift vs. field calculated using ideal and localized-hole Schrödinger-Poisson models. Models are offset to the experimental energy at zero field to facilitate direct comparisons of the experimental and theoretical *energy shifts* produced by the quantum-confined Stark effect. These small offsets remove field-independent differences in energy arising from experimental uncertainties in the SQW composition and thickness, imprecise knowledge of the exact energy level of the localizing state, and similar effects. Note that the localized-hole model substantially improves the overall agreement between theory and experiment.

Highly Aligned Arrays of GaN Nanowires Achieved via Selection of Substrate Orientation, Catalyst Concentration, and Growth Temperature

by **George T. Wang, J. Randall Creighton, A. Alec Talin, and Don Werder**

Motivation—A lack of understanding of vapor-liquid-solid (VLS) based nanowire growth has frustrated rational approaches for controlling size, optical and electrical properties, and morphology. In particular, the ordered growth of vertical nanowire arrays with controlled density, uniformity, anisotropy, and coupled interactions is of interest for potential novel device applications.

Accomplishment—We have demonstrated the growth of dense, highly aligned arrays of single crystalline GaN nanowires on untemplated, unpatterned r-plane (1-102) sapphire substrates via VLS catalyzed metal-organic chemical vapor deposition (MOCVD). Scanning electron microscopy (SEM) and transmission electron microscopy (TEM) analysis indicate that the nanowires share a common [11-20] growth direction and have aligned facets. This growth direction is the same as the observed (11-20) GaN film growth on r-plane sapphire, with a relatively low in-plane lattice mismatch of 1.15% in the [0001] GaN direction, leading to ordered, vertical growth. In contrast, nanowires grown on c-plane (0001) sapphire also most commonly exhibit a [11-20] growth direction, rather than the [0001] growth direction observed for film growth, and do not exhibit a high degree of ordering.

Interestingly, we find that the degree of alignment and size uniformity is highly dependent on the catalyst concentration applied to the substrate. Optimal density, alignment, and size uniformity occurs when the $Ni(NO_3)_2$ concentration is ~20 times more dilute than typically used for VLS-based nanowire and carbon nanotube growth, as shown in Fig. 1. Additional experiments show that the average catalyst nanocluster size decreases and size uniformity increases with decreasing catalyst concentration, suggesting orientation is dependent on particle size. Surprisingly, analysis shows that the majority of the aligned nanowires grown on r- plane sapphire do not have a catalyst droplet at the tip (Figs. 1 and 2), in contrast to GaN nanowires grown on c-plane sapphire and SiO_2, even though the presence of catalyst is necessary for nanowire growth. Further investigation of this observation is underway.

The effect of growth temperature on nanowire properties was also studied. Characterization using a Sandia-developed platform reveals that nanowires grown at 900 °C show a greater than 50 times increase in the absolute band edge peak intensity (Fig. 3) and approximately three orders of magnitude lower resistivity versus those grown at 800 °C. We propose that these effects are caused by increased carbon incorporation as the nanowire growth temperature is decreased.

Significance—The ability to use inexpensive, large area, and process compatible sapphire wafers for the growth of aligned, vertical arrays of GaN nanowires by MOCVD and without the use of templates or patterning represents an important step towards realizing devices based on vertically integrated III-nitride nanowires. Our results suggest that the alignment of VLS-grown nanowires may be influenced not only by substrate orientation, but also by catalyst particle size. Additionally, we find that the growth temperature is a critical factor for controlling the nanowire properties, due most likely to its effect on impurity incorporation.

Sponsors for various phases of this work include: DOE Office of Basic Energy Sciences and Laboratory Directed Research & Development

Contact: George T. Wang, Advanced Materials Sciences, Dept. 1126
Phone: (505) 284-9212, Fax: (505) 844-3211, E-mail: gtwang@sandia.gov

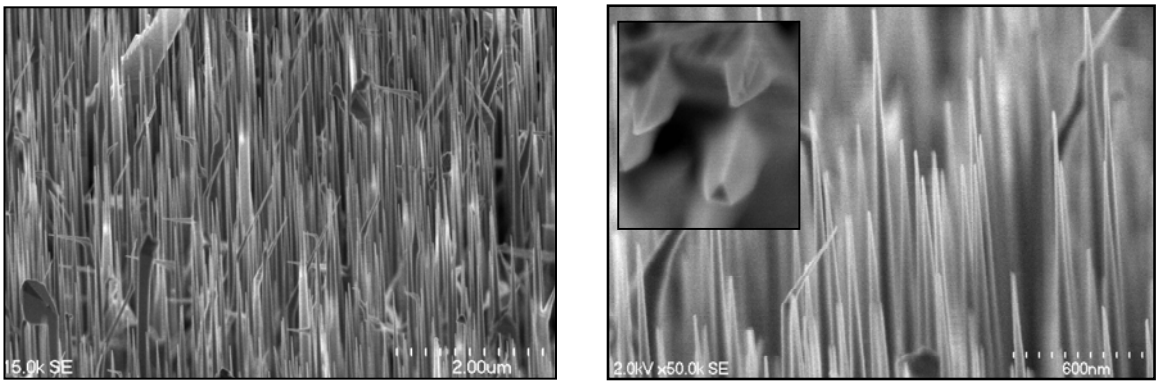

Figure 1. SEM images of highly aligned GaN nanowires grown on r-plane sapphire at 800 °C using 0.0005 M nickel nitrate solution. Inset shows that facets of different wires are aligned.

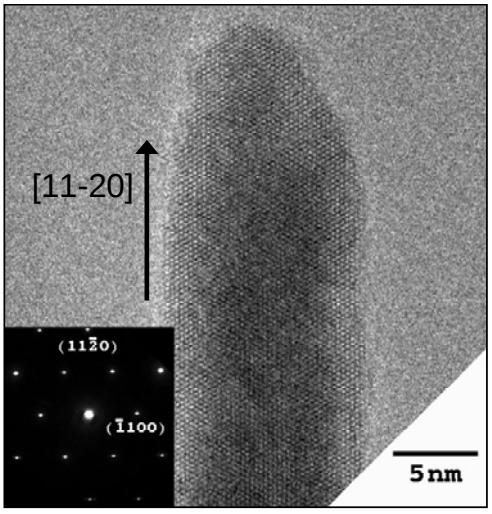

Figure 2. High resolution TEM image and selected area electron diffraction (SAED) patterns (inset) of single crystalline GaN nanowire grown at 800 °C. Note lack of catalyst nanocluster at tip.

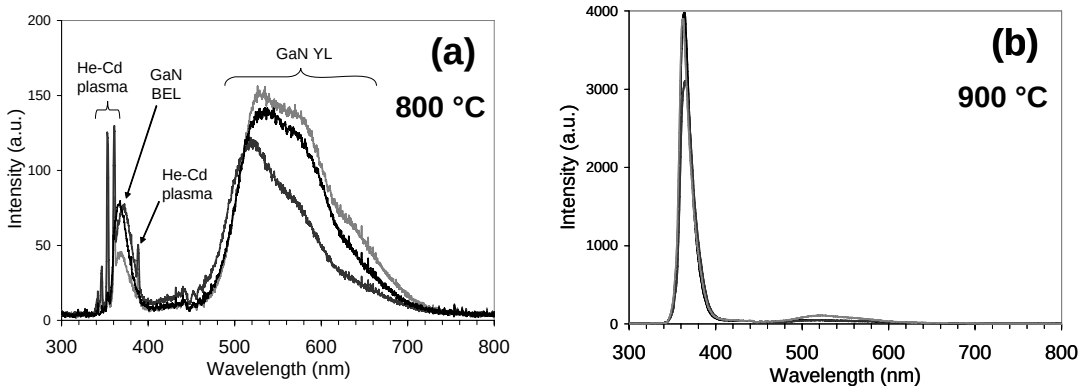

Figure 3. Representative photoluminescence (PL) spectra of GaN nanowires grown on r-plane sapphire at (a) 800 °C and (b) 900 °C.

Novel AlN Growth Processes for High Performance Deep UV Optoelectronics

by **A. A. Allerman, M. H. Crawford, K. H. A. Bogart, S. R. Lee, D. M. Follstaedt, N. A. Missert, and P. P. Provencio**

Motivation—AlGaN semiconductors have emerged as materials of great technological importance. With direct energy bandgaps that are tunable throughout much of the ultraviolet (UV) region of the spectrum (200-365 nm), these alloys have recently enabled compact, solid-state, solar-blind detectors as well as UV light emitting diodes (LEDs) and laser diodes. Relevant applications for these devices include flame and missile plume detection, fluorescence-based biological agent detection, non-line-of-sight communication, and portable water purification.

A major challenge of achieving high performance AlGaN optoelectronic devices is the lack of commercially available native substrates. Growth of AlGaN alloys is typically performed on lattice-mismatched sapphire or SiC substrates, resulting in high (> 10^{10} cm^{-2}) densities of threading dislocations. Our previous research has shown that the electrical and optical performance of deep UV emitters is critically limited by threading dislocations. Therefore, a major emphasis of our research has been to investigate methods to lower the dislocation density of AlGaN device structures by controlling the AlGaN growth process on lattice-mismatched substrates.

Accomplishment—To date, our best AlGaN device structures have been nucleated on AlN epilayers grown on sapphire substrates. Our studies have revealed that the crystal quality of AlGaN-based device layers is largely determined by the nucleation and growth conditions of the AlN epilayer. We have developed a growth process for AlN epilayers that utilizes a morphologically complex "transitional" AlN layer between the sapphire or SiC substrate and the conventionally grown AlN epilayer. This transitional layer consists of a self-organized, denticulated surface structure that is revealed by the atomic force microscopy image in Fig. 1. The structure is created by the application of lower growth temperatures and careful selection of the partial pressures of hydrogen, ammonia and trimethylaluminum.

The overgrowth of a high temperature AlN layer on an AlN surface similar to Fig. 1 enables the recovery of a smooth surface morphology suitable for device structures and results in a significant reduction of dislocation density. The full width half max (FWHM) of two complementary x-ray diffraction (XRD) measurements of AlN epilayers with and without the transitional layer is shown in Fig. 2. Improved crystal quality is indicated by narrower FWHM of the x-ray linewidths. The application of this denticulated layer has specifically enabled dislocation densities of < $1x10^9$ cm^{-2}, compared to densities of 2-5 x 10^{10} cm^{-2} achieved without this transitional layer. This novel AlN growth process and its application to improved AlGaN devices is the subject of a patent application that has recently been filed by the Sandia team.

Significance—The reduction of dislocation density in AlN films is expected to improve the performance of UV emitters and detectors by improving the electrical and optical properties of the overlying AlGaN device layers. With improved performance, AlGaN optoelectronic devices will replace photomultiplier tubes, mercury lamps and/or large frame lasers and enable a new generation of compact, robust and portable systems for sensing, communications and water purification.

Sponsors for various phases of this work include: Defense Advanced Research Projects Agency/Semiconductor Ultraviolet Optical Sources, Laboratory Directed Research & Development, and Nuclear Weapons/Science & Technology

Contact: Andrew A. Allerman, Advanced Materials Sciences, Dept. 1126
Phone: (505) 845-3697, Fax: (505) 844-3211, E-mail: aaaller@sandia.gov

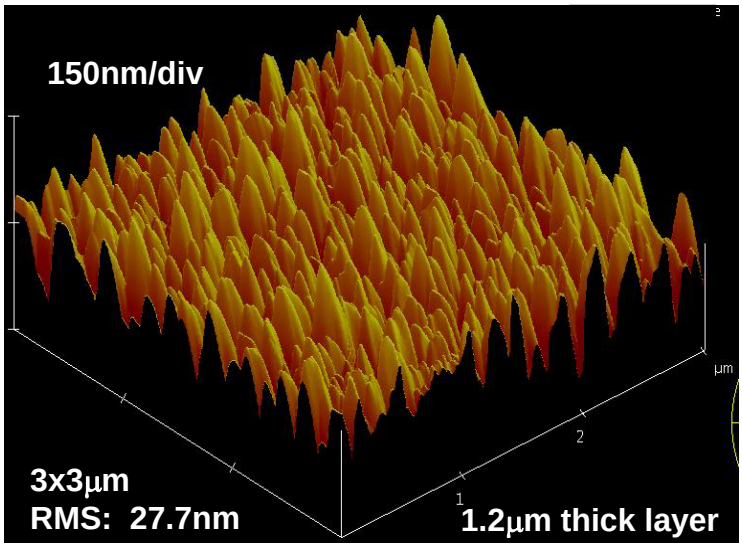

Figure 1. An atomic force microscopy image of the surface of an AlN transitional layer showing the self-organized, denticulated structure formed under specific growth conditions. This structure is responsible for the reduction in the density of threading dislocations of the overgrown, high temperature AlN layer.

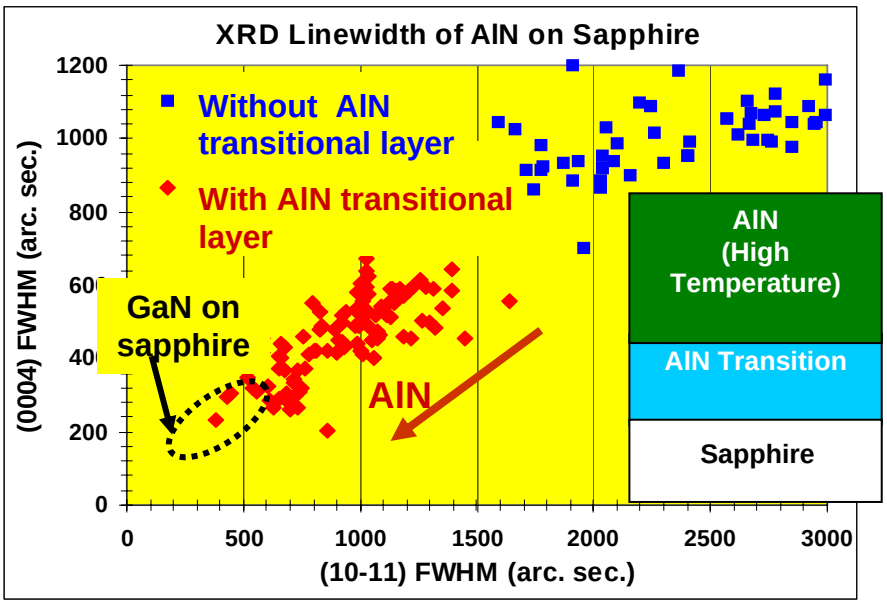

Figure 2. A significant reduction in the full width half max (FWHM) of the x-ray diffraction (XRD) linewidths of the high temperature AlN layer is achieved when an AlN transitional layer, similar to Fig. 1, is grown before the high temperature AlN layer. The smaller FWHM linewidth indicates improved crystalline quality. Through application of this transition layer, the quality of AlN films on sapphire is approaching that of GaN epilayers that are commonly used in commercial blue LEDs.

Microwave Dissipation in Carbon Nanotubes and Silicon Nanowires

by **Clark Highstrete, Mark Lee, and Alec Talin**

Motivation—Single-wall carbon nanotubes (SWCNTs) and silicon nanowires (SiNWs) are predicted to have novel electrodynamic properties that could be exploited to push nanotechnology into the microwave frequency domain. For example, there are claims in the literature that short, pure SWCNTs and SiNWs support ballistic charge transport at room temperature, meaning that electrons cross these nanomaterials without scattering. From the point of view of microwave response, ballistic transport implies a "magic" microwave material with no high-frequency power dissipation. Such dissipationless behavior has some experimental as well as theoretical support in the literature, but the signal-to-noise levels in reported empirical work are poor and remain controversial. It remains unclear whether nanomaterials such as SWCNTs and SiNWs are truly "magic" or whether they have microwave loss characteristics that are simply too small to be detected by the methods reported.

Accomplishment—We succeeded in using AC dielectrophoresis (ACDEP) directed self-assembly to incorporate arrays of between 10^2 to 10^4 SWCNTs or *n*-doped SiNWs onto a broadband co-planar waveguide (CPW) microwave measurement platform. These nanomaterials are assembled in such a way that they are parallel to the electric field polarization of the propagating microwave mode on the CPW, maximizing their interaction with the electromagnetic field. Figure 1 shows an optical microscope image of SiNWs assembled across the signal-to-ground plane gaps of a CPW.

The CPW's complex reflection and transmission coefficients before and after ACDEP assembly of nanomaterials were measured using a precisely calibrated vector network analyzer on a broadband probe station. Most importantly we developed a carefully calibrated and controlled measurement procedure that yielded signal-to-noise and systematic reproducibility that is a factor of 10 to 100 times better than what has been reported in the literature.

Because of this very high measurement quality, we were able to reliably calculate from the measured data the change in power loss as a function of frequency between having nanomaterials assembled on a CPW and the original CPW without nanomaterials. Such additional power loss is attributable to high-frequency dissipation by the nanomaterials.
Figure 2 shows the microwave loss coefficient α as a function of frequency measured for three different samples with SWCNT arrays and one with an *n*-doped SiNW array. The loss coefficient is always positive and frequency-dependent, proving that these nanomaterials dissipate microwave power.

Significance—The data shown in Fig. 2 are the first reliable measurements of frequency-dependent microwave power loss in SWCNTs and SiNWs. This proves that, at least at room temperature, these are not lossless "magic" microwave materials, contradicting several prominent claims in the existing literature. However, an estimate of the loss per nanotube or per nanowire shows that the high-frequency loss in a single nanotube/wire is nonzero but extremely small. Thus these nanomaterials are an extremely good microwave material.

Sponsor for various phases of this work include: Laboratory Directed Research & Development

Contact: Mark Lee, Semiconductor Material & Device Sciences, Dept. 1123
Phone: (505) 844-5462, Fax: (505) 844-4045, E-mail: mlee1@sandia.gov

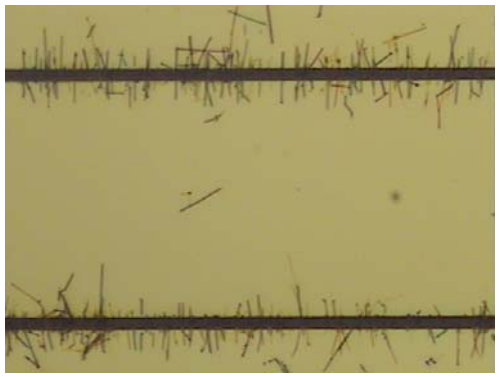

Figure 1. Optical microscope image of an array of n-doped silicon nanowires assembled via the ACDEP process across the gaps of a broadband microwave co-planar waveguide. The gap width between signal line (center gold strip) and the outer ground planes is 5 µm.

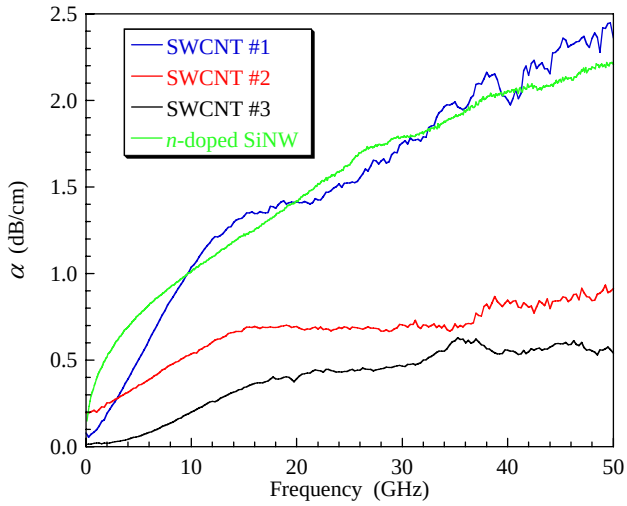

Figure 2. Microwave loss coefficient measured as a function of frequency for three different SWCNT arrays with different numbers of nanotubes and one array of *n*-doped SiNWs. A positive value for α means that the material dissipated microwave power.

Photoluminescence Dynamics of Broadband Emission from Cadmium Sulfide (CdS) Quantum Dots

by **J. E. Martin and L. E. Shea-Rohwer**

Motivation—CdS quantum dots typically have a narrow bandwidth emission that is accompanied by a photoluminescent lifetime on the order of a few ns. This fast decay is attributed to direct electron-hole recombination. Both the emission bandwidth and the PL lifetime can increase dramatically upon the addition of surface ligands. The nature of the decay can also become strongly non-exponential, and these three characteristics are thought to be due to the formation of surface trap states. Surface functionalized CdS QDs can be made following the reverse micellar synthesis developed by Lianos and Thomas. The surfactant dioctyl sulfosuccinate sodium salt (AOT) acts as the surface ligand, and the resulting 2 nm QDs have nearly white emission. Our interest is in characterizing and understanding the decay dynamics of this complex emission and how this is affected by UV photolysis. Our goal is to determine whether the PL lifetime can be controlled in such a way that QDs can be used as taggants that have both emission color and lifetime as identifying characteristics.

Accomplishment—CdS quantum dots were prepared in reverse micelles in heptane and were purified by cooling to -30°C and cold-filtering out the ice that formed. The purified solutions were then photolyzed with UV light, which is known to increase the emission intensity. Both the quantum yield (QY) and the PL lifetime were monitored during photolysis. Significantly, the emission spectrum is only slightly changed by photolysis. The QY was found to increase with photolysis, reaching a maximum value of 24%. This high value, which is twice that reported in the literature, is due to the purification before photolysis. The PL lifetime was found to increase in proportion to the quantum yield, Fig. 1, demonstrating that control of the lifetime is possible without altering the emission color. The proportionality of the lifetime and QY can be explained by a simple model of parallel radiative and non-radiative decay channels, where the non-radiative lifetime increases with photolysis. Studies at -70°C show that the quantum yield and the lifetime increase to more than twice their ambient values, which is consistent with trap state emission. Further evidence of trap states comes from the form of the PL decay, which is well described by a stretched exponential with an exponent of 0.5, Fig. 2. This decay is consistent with an exponential distribution of lifetimes, which is expected for trap states. Finally, the lifetime and the quantum yield were found to decrease significantly with the addition of alkane thiols, with only a modest red-shift in the emission, so the addition of these ligands can be used to control the lifetime.

Significance—In understanding the trap state emission in quantum dots we have shown that it is possible to control the PL lifetime independently of emission color. Lifetime control can be accomplished by photolysis or by the addition of surface-active ligands, such as alkanethiols. This discovery demonstrates that QDs can be used as two-dimensional taggants, which greatly increases the number of distinguishable taggants that can be synthesized. With the development of UV LEDs it is now possible to make a compact device for measuring the PL lifetime, based on the phase-shift method, so lifetime tagging may become a practical reality.

Sponsors for various phases of this work include: DOE Office of Basic Energy Sciences and Laboratory Directed Research & Development

Contact: James E. Martin, Nanostructure & Semiconductor Physics, Dept. 1112
Phone: (505) 844-9125, Fax: (505) 844-4045, E-mail: jmartin@sandia.gov

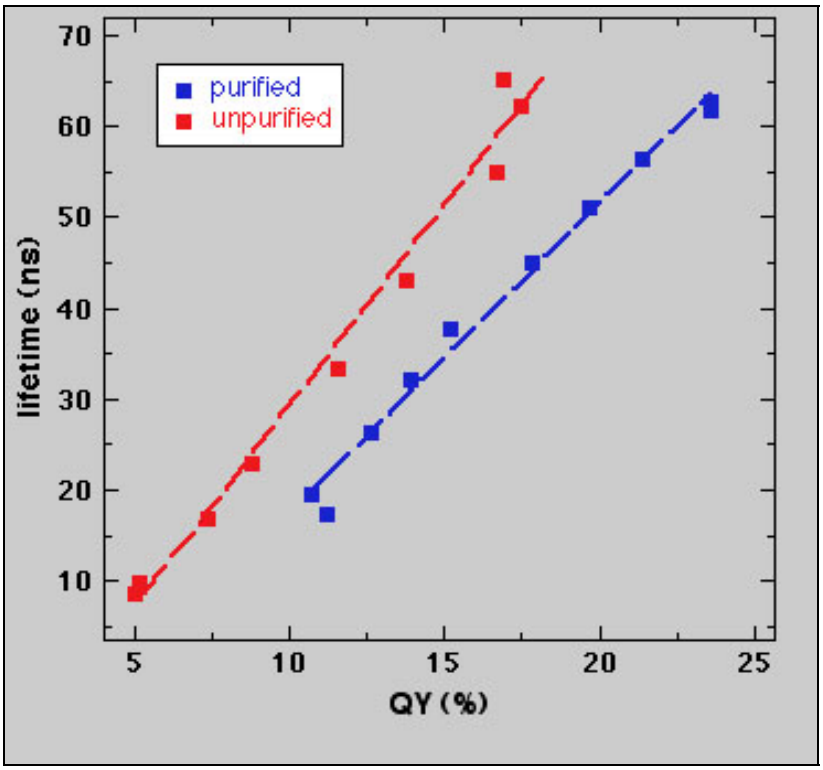

Figure 1. For both purified and unpurified CdS samples the lifetime is proportional to the quantum yield, although the purified sample has a considerably larger QY. The QY increases with photolysis.

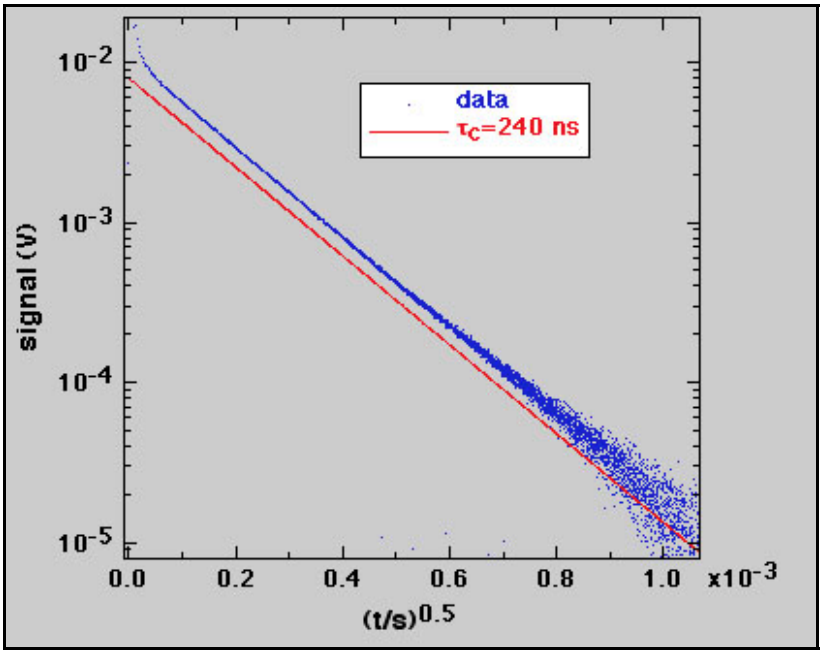

Figure 2. The PL decay of broadband-emitting CdS quantum dots is well described by a stretched exponential decay with an exponent of 0.5. This is consistent with a broad, exponential distribution of lifetimes. The characteristic time of this decay is 240 ns.

Self-assembled Quantum Dots for Detectors and Emitters in the Long-wavelength Infrared

by **Jeffrey G. Cederberg and Eric A. Shaner**

Motivation—Self-assembled quantum dots (SAQD) have unique optical properties that make them promising for potential long-wavelength infrared (LWIR) applications. Unlike quantum well infrared photodetectors (QWIPs), detectors utilizing the electrons populating the conduction subband, introduced by doping the SAQD, can readily couple to surface-normal incident radiation. The electron promoted to a higher conduction band state can tunnel through potential barriers under applied voltage and be sensed as a photocurrent. Emitters require injection of electrons into an excited state and a radiative transition to the ground state of the SAQD. We are utilizing the intersubband transitions of SAQD to develop detectors and emitters. SAQD have several advantages over quantum well analogs. The quantum mechanical selection rules for a SAQD allows them to emit or sense radiation with all polarizations. For emitters this eliminates the need to engineer a grating structure to extract light out of a cascade laser based on quantum wells. This characteristic makes the detector structure sensitive to normal incidence radiation.

Accomplishment—We have undertaken the development of LWIR emitters. For efficient emitter operation, the ground state of the SAQD must be above the conduction bandedge of GaAs. The conduction band diagram in Fig. 1 shows this can be achieved by increasing the potential around the SAQD using an AlAs matrix. A prerequisite for SAQD growth is a smooth morphology of the underlying layer. While this has been reported by molecular beam epitaxy, this structure has not been reported by metal-organic chemical vapor deposition (MOCVD). Our use of a low decomposition temperature metal-organic precursor allowed us to achieve smooth AlAs surfaces at temperatures as low as 480°C (Fig. 2a). The root mean square roughness of the AlAs layer is 0.6 nm. The growth of InAs SAQD on AlAs challenged our paradigm developed for InAs SAQD on GaAs. For the InAs on GaAs system, a post-growth purge has been shown to be essential to facilitate the surface mass transfer needed for SAQD formation. The short post-growth purge of two seconds was found to have a negative influence on InAs SAQD grown on AlAs (Fig. 2b) resulting in large, faceted islands (20 nm high). Eliminating the post-growth purge from the growth sequence produced small (2 nm high), dense islands (Fig. 2c).

Significance—Success in finding appropriate conditions for InAs SAQD growth on AlAs provides an internal source of material for LWIR emitters and detectors. Future efforts will generate cavity structures to look at resonant cavities with and without two-dimensional photonic crystals etched into the surface. This success impacts not only emitter fabrication, but it extends the wavelengths over which detectors are sensitive. Shorter wavelength detector sensitivity should be achieved with InAs SAQD in high Al content AlGaAs matrices compared to current GaAs based designs. The long term goal of this effort is to demonstrate a surface emitting quantum cascade laser structure, which would be a significant advancement for this technology.

Sponsor for various phases of this work include: Laboratory Directed Research & Development

Contact: Jeffrey G. Cederberg, Advanced Materials Sciences, Dept. 1126
Phone: (505) 284-5456, Fax: (505) 844-3211, E-mail: jgceder@sandia.gov

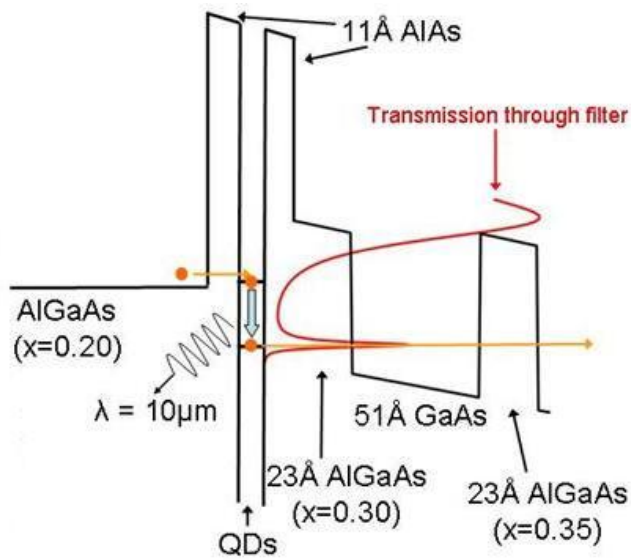

Figure 1. Conduction band diagram of intersubband emitter structure using SAQD as the active media. By placing the InAs SAQD between AlAs layers, the ground state is raised above the GaAs conduction bandedge, a necessary condition for depopulation of the ground state.

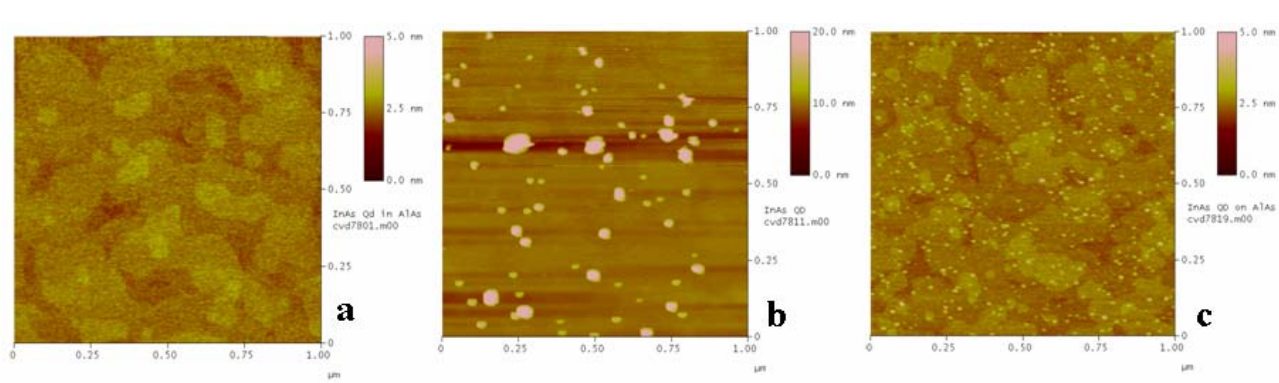

Figure 2. Atomic force microscopy images of surfaces: a) AlAs grown at 480°C with a RMS roughness of 0.6 nm, b) InAs SAQD on AlAs purged for 2 sec without AsH_3 present in growth chamber, c) InAs SAQD not subjected to any time without AsH_3 during their growth.

Nanomaterials

Active Transport of Carbon Nanotubes Using Motor Proteins

by **B. C. Bunker, E. D. Spoerke, J. Hendricks, and G. D. Bachand (SNLA); Professor Robert Haddon (University of California, Riverside)**

Motivation—Parallel and directed assembly of nanoscale building blocks is required to create nanodevices of practical significance. We are exploring the use of energy-consuming "nano-robots" – motor proteins and microtubules – for the active transport, assembly, reconfiguration, and healing of nanocomposites in artificial environments. As a model system, we are currently collaborating with Professor Robert Haddon's research group at the University of California, Riverside, to learn how to use motor proteins to manipulate single-wall carbon nanotubes (SWNTs) in microfluidic systems. The ultimate goal of the collaboration is to learn how to create arrays of programmable conductive interconnects.

Accomplishment—The geometry we have selected for promoting the active transport and assembly of carbon nanotubes (Fig. 1) is the so-called inverted motility assay. In this geometry, self-assembled monolayers containing the motor protein kinesin (pink) are anchored to an array of gold electrodes such that the mobile "feet" of the motors are available for binding to short segments of microtubules called shuttles (green). In the presence of adenosine triphosphate (ATP) "fuel", the motors propel the shuttles and any associated "cargo" across the substrate surface. Haddon's group has functionalized their carbon nanotubes (blue) with streptavidin (red arc), which forms a strong linkage with microtubules that we have functionalized with biotin (red ovals). As both the microtubules (25 nm diameter) and the typical bundles of carbon nanotubes (5-10 nm diameter) are too small to observe under normal circumstances, both components have been labeled with fluorescent dyes that allow them to be observed under a fluorescence microscope. We recently received the functionalized SWNTs from the Haddon group and have been able to: (1) disperse the SWNTs, which are normally agglomerated, (2) attach the SWNTs to our microtubules in solution, (3) adsorb the microtubules onto patterned gold electrodes, and (4) examine the adsorption and motility of the microtubule-SWNT constructs under the microscope. Images obtained to date (Fig. 2) clearly show that (1) the microtubules are almost exclusively adsorbed onto the gold electrodes by the motor protein monolayers, (2) the carbon nanotubes are bound exclusively to the microtubules (no free nanotubes are present), (3) single microtubules (which can be over 10 microns long) can span the gaps between electrodes, bridging the gaps with conductive carbon nanotubes, and (4) (not shown) although coated with SWNTs, the microtubules remain active and are propelled by the motor proteins in the presence of ATP fuel. Work will now progress to determining the electrical conductivity of the microtubule-SWNT bridges and learning how to program the microtubules to create and remove bridges on command.

Significance—SWNTs are regarded by many as the ultimate nanomaterial because of their unique electrical, optical, and mechanical properties. If we can learn how to manipulate SWNTs with motor proteins, we should be able to create and reconfigure complex, responsive networks of SWNTs using biomimetic strategies that are more versatile and controllable that existing techniques. For example, it is difficult to create such networks using current methods that involve physically picking up and placing each nanotube using nanomanipulators such as scanning probe systems.

Sponsors for various phases of this work include: DOE Office of Basic Energy Sciences/Center for Integrated Nanotechnologies (CINT)

Contact: Bruce C. Bunker, Chemical Synthesis and Nanomaterials, Dept. 1816
Phone: (505) 284-6892, Fax: (505) 844-9781, E-mail: bcbunke@sandia.gov

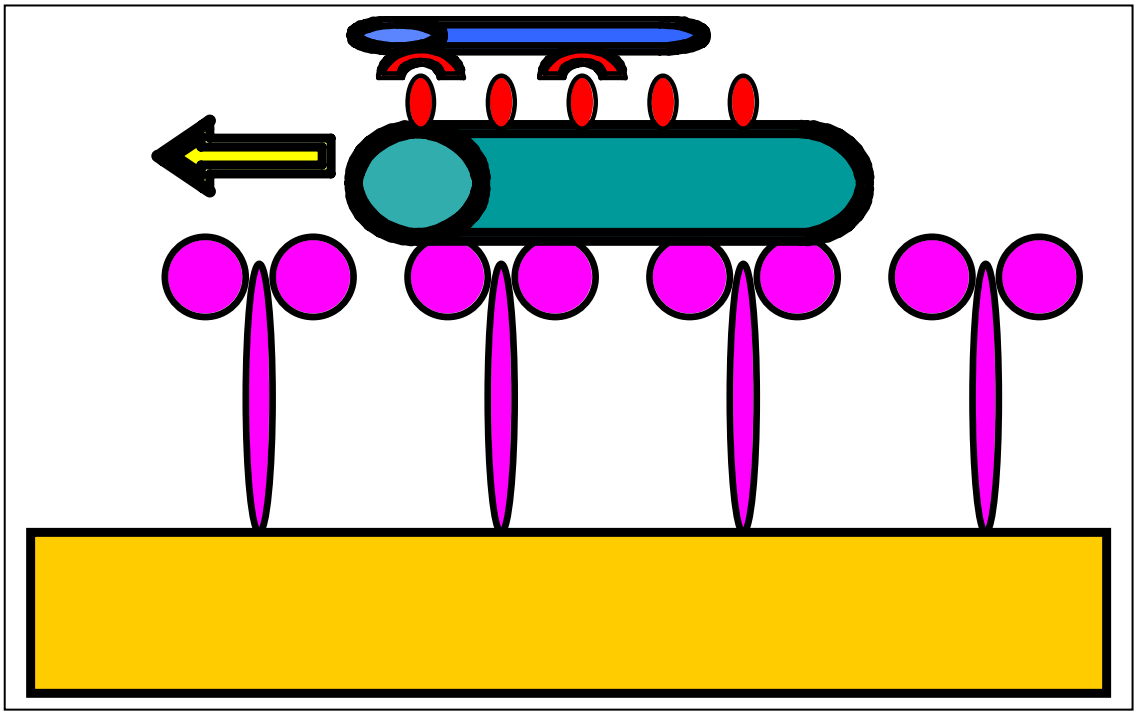

Figure 1. Depiction of the system used for the active transport of carbon nanotubes (blue) attached to microtubules (green) via the biotin-streptavidin linkage (red ovals to red arcs). Motion is provided when the "feet" of tethered motor proteins (pink) "walk" along and thereby propel the microtubule shuttles.

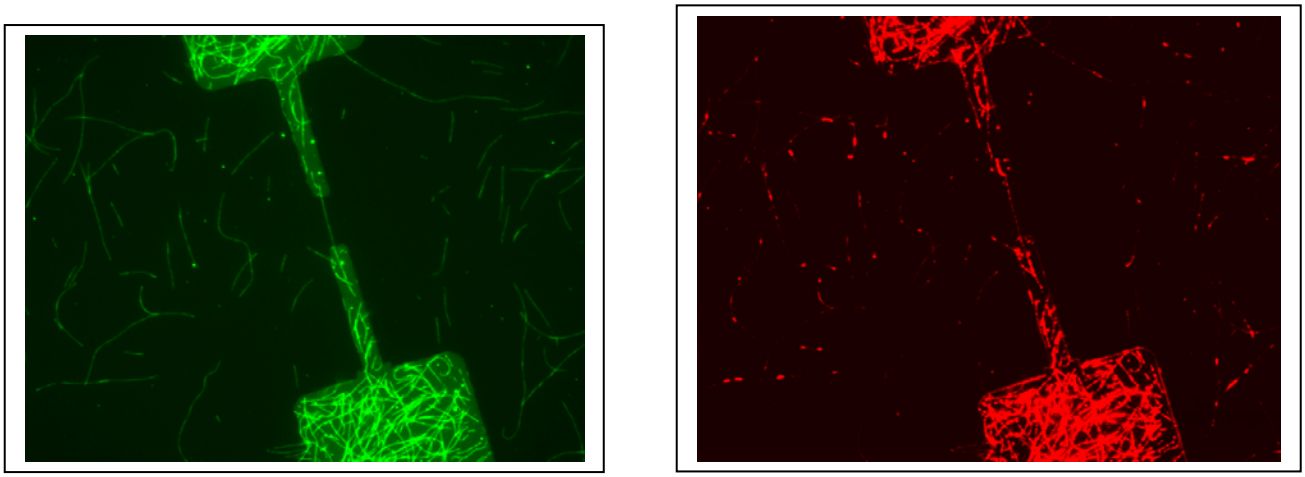

Figure 2. Fluorescence micrographs of microtubule-SWNT constructs bound via motor proteins to gold electrodes (square region is 25 microns across). Left – Fluorescence signal from the microtubules. Note that one microtubule spans the gap between the top and bottom electrodes. Right – Fluorescence signal from the carbon nanotubes. Note that all carbon nanotubes are associated with microtubules.

Chain Transfer to a Surface—a Novel Method for Forming Polymer Nanofilms

by **D. L. Huber and B. C. Bunker**

Motivation—One of the hallmarks of nanomaterials is their high surface area. Controlling surface properties are therefore critical to their synthesis, processing, and often their usefulness. Polymers have long been a popular coating for modifying surface properties of a wide range of materials. The surface properties of a polymer are generally dictated by the top few nanometers, but it is difficult to synthesize pinhole-free nanoscopic polymer films. The ability to grow, through an *in-situ* polymerization, ultrathin polymer films opens a wide range of surface functionalizations for nanoparticles and nanomaterials. Applications include solubilization and compatibilization of nanomaterials, and synthesis of active polymer films with extremely fast kinetics.

Accomplishment—We have developed a method of functionalization a wide range of surfaces, with an equally wide range of polymers. Any surface that can support a self-assembled monolayer can be functionalized by any polymer capable of undergoing a radical polymerization.

The basic synthetic scheme is shown in Fig. 1, using a silicon oxide surface with a silane coupling agent as an example. A monolayer coating of a chain transfer agent is applied to the substrate and a solution of monomer and free radical initiator covers the surface. The radical initiator is initiated, and a fraction of the initiators that are near the surface when they become free radicals are able to transfer their free radical to the surface. The surface bound radical is then able to initiate the growth of a surface bound polymer. This polymer grows for a very short time before undergoing a chain termination event, whether chain transfer, recombination, or some side reaction. The kinetics of the steps in this polymerization are critical to the resultant polymer film.

Figure 2 shows a plot of film thickness for the synthesis of two polymers, poly(N-isopropyl acrylamide) (pNIPAM) and poly(methyl methacrylate) (PMMA), using this method. The film thicknesses in the pNIPAM system reveals an interesting behavior based upon the system's kinetics. The linear increase at low monomer concentrations is due to the expected linear increase in polymer molecular weight. At higher concentrations, the viscosity of the solution becomes an issue. This viscosity increase slows the diffusion of free radicals to the surface, lowering the graft density. The net effect of the reaction kinetics is that the reaction is self-limiting. Film synthesized by this method is necessarily nanoscopic, and are generally pinhole-free.

Significance—A simple and versatile method to form continuous ultrathin polymer films using only commercially available reagents has been developed. This synthetic technique has a multitude of applications to microfluidics, biotechnology, nanomaterials preparation and funtionalization, etc. Traditional techniques for forming *in-situ* polymer films have required laborious synthesis of custom initiators, and carefully controlled reaction conditions (concentrations, purities, inert atmospheres, etc.). This method requires none of these. Using this technique, a minimally skilled lab worker can prepare a wide range of high quality surface bound polymer films on most of the commonly encountered surfaces and particles.

Sponsors for various phases of this work include: DOE Office of Basic Energy Sciences and Laboratory Directed Research & Development

Contact: Dale L. Huber, CINT Science, Dept. 1132
Phone: (505) 844-9194, Fax: (505) 284-7778, E-mail: dlhuber@sandia.gov

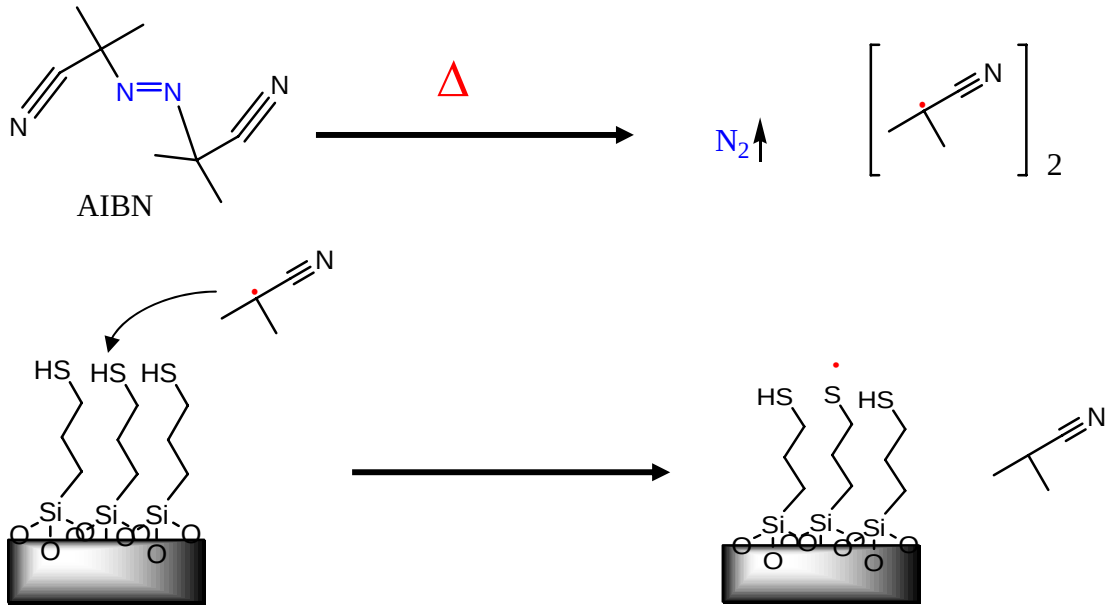

Figure 1. Reaction scheme for a chain transfer to a surface. Free radicals are generated in solution, and transferred to the surface via proton abstraction. The surface bound radical is then capable of initiating a surface bound polymer.

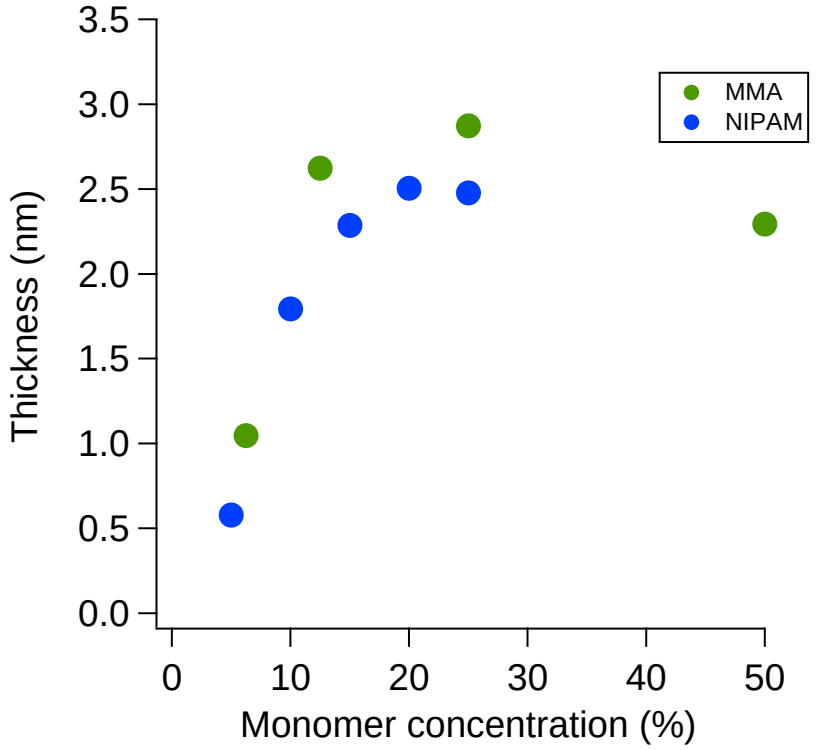

Figure 2. Thickness of polymer films as a function of the monomer concentration, with all other reaction conditions held constant. At low monomer concentration the thickness increases due to increasing molecular weight, while at high monomer concentration the thickness decreases due to decreasing graft density.

Controlled Growth of Single- and Multi-Wall Carbon Nanotube Arrays

by **M. P. Siegal, P. P. Provencio and D. L. Overmyer**

Motivation—Carbon nanotubes (CNTs), perhaps the prototypical nano-material, demonstrate intriguing physical properties and promise a plethora of potential applications, ranging from room-temperature cold-cathode electron field-emitters (pulsed-power, µ-mass spectrometers, low-voltage flat-panel displays) to nanoelectrodes for electrochemical sensing to nm-sized hollow tubes for mass separation and filtration to thermal conducting heat pipes for cooling various platforms. Many of these applications require arrays of highly-crystalline CNTs, to minimize electron and phonon scattering, on a substrate surface with uniform diameters and controlled spacings, and grown preferably at the lowest possible temperatures.

Accomplishment—Arrays of single-wall CNTs (metallic or semiconducting) grow at temperatures > 800 ˚C. Multiwall CNTs grow at lower temperatures and are always electrical conductors, advantageous for most of the above listed applications. Previously, using thermal chemical vapor deposition (CVD), we showed independent control of CNT diameters ranging from 7 – 350 nm (via growth temperatures from 630 – 790 ˚C) and the average spacing apart in arrays from nm's to µm's (via the metal catalyst residual stress and the chemical reactivity of the hydrocarbon feed gas). Only CNTs with diameters < 10 nm were found to consist purely of concentric graphene cylinders.

Recently, we explored CNT growth down to 530 ˚C. These CNTs have superb crystallinity and can result in arrays primarily consisting of single and double-wall CNTs. This is the first demonstration of such small diameter CNTs in arrays and at such low growth temperatures. CNTs harvested from substrates into solution were deposited onto holey-carbon grids for analysis by transmission electron microscopy (TEM). Figure 1 shows clusters of single (530˚C) and double-wall (550˚C) CNTs. Since CNTs with pure graphene sheet outer walls cluster together in solution via Van der Waal's forces, individual CNT structures can be discerned in transmission only from the edge of a bundle.

Figure 2(A) shows the analysis of the TEM images and finds that CNT diameters increase linearly with growth temperature from 530 – 610 ˚C. Resolution is sufficient to count the number of concentric graphene cylinders in a given nanotube. Plotted in Fig. 2(B), an additional graphene cylinder grows ~ with every 20˚C of thermal CVD temperature. The average wall layer thickness, measures to be the same for every sample at 0.375 ± 0.10 nm, comparing favorably with the 0.335 nm interplanar spacing of graphite. The hollow inner core of the CNTs over this entire range of growth temperature is 0.7 ± 0.1 nm.

Significance—Carbon nanotube arrays have potential for many nano-electronic, thermal, and chem/bio sensing applications. For the first time, we demonstrate precise control of CNTs within arrays with thicknesses ranging from 1 – 6 concentric graphene cylinders. Further, these small-diameter and high-crystalline nanotubes are all grown at temperatures below previous reports. In principle, such precise nano-structural control should vastly improve electrical and thermal properties. Future work needs to identify structure-property relationships to develop a better fundamental understanding.

Sponsor for various phases of this work include: Laboratory Directed Research & Development

Contact: Michael P. Siegal, Advanced Materials Sciences, Dept. 1126
Phone: (505) 845-9453, Fax: (505) 844-4045, E-mail: mpsiega@sandia.gov

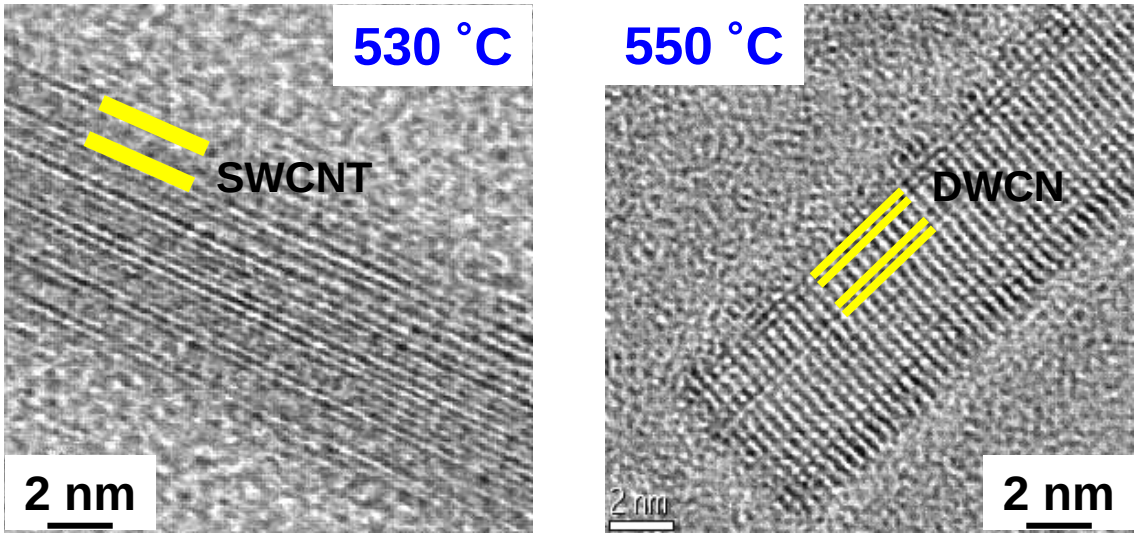

Figure 1. High-resolution TEM images of carbon nanotubes harvested from films grown at 530 ˚C and 550 ˚C. Van der Waal's forces cause the CNTs to agglomerate in bundles; therefore, to discern the structure of individual tubes, attention must be paid to the edge of a bundle where the electrons have the best chance to transmit through only a single nanotube. The 530 ˚C sample yielded single-wall CNTs; the 550 ˚C yielded double-wall CNTs. Examples are highlighted in yellow to guide the eye.

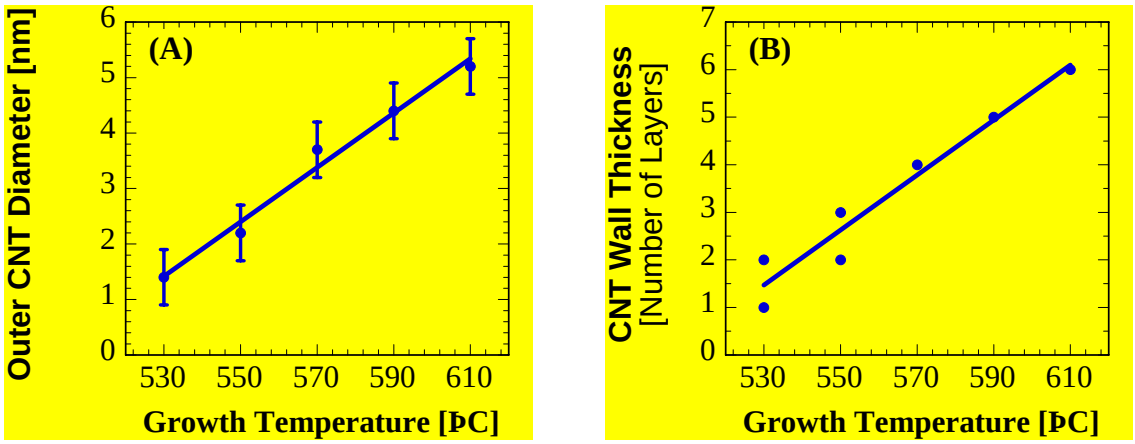

Figure 2. Results from high-resolution TEM images as in Fig. 1. (A) Outer diameters of nanotubes vs. CVD growth temperature. (B) The number of concentric graphene cylindrical sheets per nanotube vs. CVD growth temperature. Note that the wall diameter and number of sheets per wall increase linearly with growth temperature.

Crawler for Microfluidic Systems Based on Switchable Polymers

by **B. C. Bunker, D. L. Huber (SNL), and Ulrich Wiesner (Cornell University)**

Motivation—One of the fundamental problems in microfluidics is the transformation of energy into directed motion and load transport on very small length scales. While it has been demonstrated that active motor proteins extracted from living cells can provide such motion, there are many potential advantages in using synthetic as opposed to biological materials for such systems. Synthetic devices could work in a much wider range of environmental conditions, and be easier to maintain and control. This collaboration between Sandia and Professor Uli Wiesner at Cornell University involves investigating one such transportation system based on the use of a switchable polymer gel called poly (n-isopropyl acrylamide) or PNIPAM.

Accomplishment—The switchable polymer we are investigating for active transport (PNIPAM) is one that Sandia has already utilized for creating programmable surfaces to grab and release species such as proteins. The polymer undergoes a phase transition at 35°C (Fig. 1, left). Above the transition temperature, the polymer is in a collapsed, dense state. Below the transition temperature, the polymer swells in water, increasing its net volume by an order of magnitude. Experiments conducted by the Weissner group at Cornell have shown that this volume change can be exploited to create polymeric plugs that can be programmed to "crawl" through microchannels (Fig. 1, right). This mechanism for motion is inspired from the locomotion of earthworms, which move by making their body "fat" or "thin" at different point in time and space. "Fat" segments provide anchor points and allow for further extension of the "thin" parts. The Weissner group has created nanocomposites of PNIPAM and 30 nm wide hectorite clay particles as stabilizers and demonstrated that composite plugs can transport glass beads at a rate of 15 microns/second in a 1 mm capillary tube. The Wiesner group has also developed a theoretical expression indicating that gel velocities should be inversely proportional to the square of the gel diameter. Uli Weisner is interested in collaborating with Sandia to test this model. Sandia's major contribution to the project involves the developing the means to thermally program the PNIPAM gel on small length scales. Sandia has developed a microdevice (Fig. 2) that is capable of providing highly localized heating (and cooling) on a length scale of around 10 microns. Sandia is also exploring the use of focused IR lasers to provide localized heating to PNIPAM gels in microchannels. Integrated fluidic systems are currently being developed for the PNIPAM experiments, and should be ready to be deployed within a few months.

Significance—Volume phase transitions in polymer gels are diffusion controlled, which means that transition times are dependent on sample dimensions. By reducing the size of our polymer plugs down to microns, we should be able to create a transportation system in which the phase transition could drive objects in microchannels at velocities that could exceed 100 microns/second. Our Cornell-Sandia collaboration will enable us to test theoretical predictions of the transitional velocity of polymer gels, elucidate the length scale at which macroscopic behavior of the gel will break down (e.g. due to gel heterogeneities), and help CINT explore new concepts for microfluidic systems based on engineered nanomaterials.

Sponsors for various phases of this work include: DOE Office of Basic Energy Sciences/Center for Integrated Nanotechnologies (CINT)

Contact: Bruce C. Bunker, Chemical Synthesis and Nanomaterials, Dept. 1816
Phone: (505) 284-6892, Fax: (505) 844-9781, E-mail: bcbunke@sandia.gov

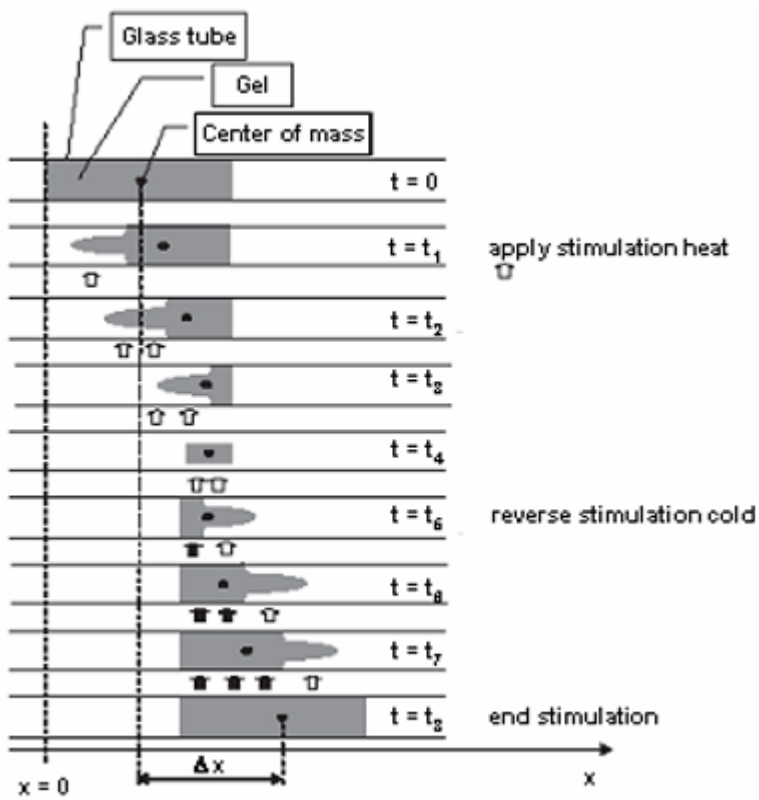

Figure 1. Schematic representation of the translation of a PNIPAM gel plug in a microchannel.

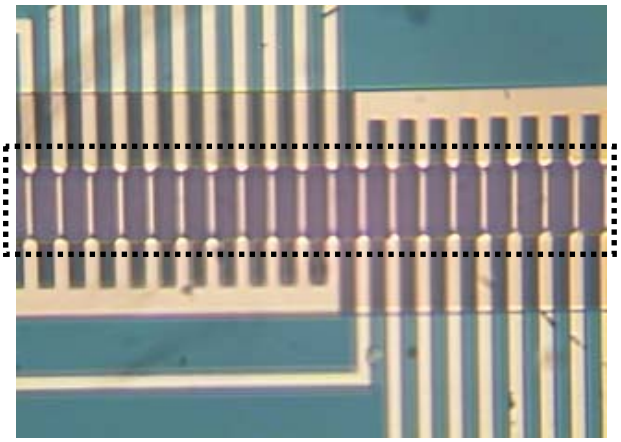

Figure 2. Sandia's micro-hotplate that will be used to program the phase transition in PNIPAM contained in a microchannel above the heater. Each hotline in the center has a diameter of 10 microns and can be independently programmed to induce the translation of the PNIPAM gel.

Growth, Assembly, and Characterization of Zinc Oxide Nanostructures

by **J. W. P. Hsu, N. C. Simmons, T. L. Sounart, J. Liu, D. A. Scrymgeour, D. A. Tallant, L. N. Brewer, J. A. Floro, and J. A. Voigt**

Motivation—ZnO nanostructures are at the forefront of nanomaterials research because of their interesting semiconducting, optical, and piezoelectric properties, combined with their relative ease of growth by various techniques. The next step in making these nanostructures useful requires assembling them on surfaces in a controlled manner. Since conventional lithography techniques are not conducive to patterning of three-dimensional nanomaterials, new approaches need to be developed.

Accomplishment—Microcontact printing was employed to form an organic template in order to direct ZnO nanorod growth from solution on Ag surfaces [Fig. 1(a)]. Solution growth utilizes environmentally benign chemistry and is compatible with the use of organic molecules to control/modify inorganic crystal growth. Organic modifiers were used to create complex ZnO nanostructures. Fig. 1(b) shows an example of these nanostructures assembled on pre-determined locations on surface.

In this experiment, it was observed that the majority of ZnO nanorods orient with the [0001] axis perpendicular to the Ag substrate. The Ag films used were polycrystalline with high (111) texture but no in-plane alignment. ZnO nanorods also display random in-plane orientations. However, when a multi-grain Ag foil was used as a substrate, preferential nucleation on [111] oriented grains was evident [Fig. 2(a)] with ZnO rods orienting perpendicular to the surface and displaying in-plane alignment (modulo 6-fold degeneracy). Since transmission electron microscopy images show that the ZnO-Ag interface is abrupt and contains no foreign materials such as AgO [Fig. 2(b)], there is definitely a crystallographic relation between ZnO and Ag.

The physical properties of these ZnO nanorods were investigated with piezoelectric force microscopy (PFM) and photoluminescence (PL). ZnO has a wurtzite crystal structure, with inversion symmetry broken in the [0001] direction and piezoelectric response parallel to that direction. Using PFM, it was established that these ZnO nanorods are oriented with <0001> directed away from the substrate (Fig. 3). Piezoelectric response was quantitatively measured and found to vary from rod to rod. This variation was not correlated with rod length or diameter. The origin is currently being investigated. PL measurements of as-grown and annealed nanorods reveal that the defects responsible for deep-level luminescence are different from those found in vapor phase grown nanostructures, are not associated with oxygen deficiency, and most likely exist in the bulk, rather than the surface, of the nanorods.

Our efforts in ZnO nanorod growth and characterization have generated several publications in premier journals (including one feature article with cover art), many invited and contributed talks, and a First-place "Art as Science" award at the Materials Research Society Spring 2005 meeting.

Significance—The ability to synthesize controlled ZnO nanostructures is the foundation of our current work on next-generation solar cells based on ZnO nanostructures and conducting polymer matrices. These hybrid solar cells are targeted for light-weight, portable applications, such as consumer electronics.

Sponsors for various phases of this work include: Laboratory Directed Research & Development, Truman Fellowship, and DOE Office of Basic Energy Sciences

Contact: Julia W. P. Hsu, Surface & Interface Sciences, Dept. 1114
Phone: (505) 284-1173, Fax: (505) 844-5470, E-mail: jwhsu@sandia.gov

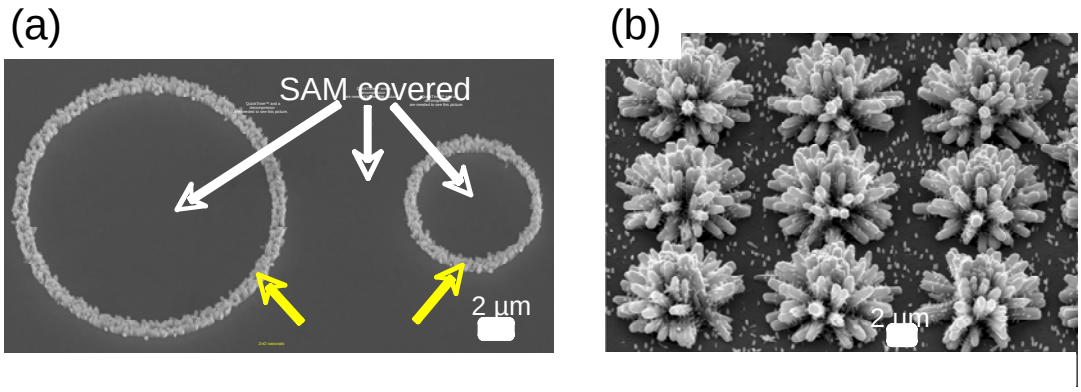

Figure 1. Solution-grown ZnO nanostructures on Ag substrates containing a molecular template. (a) Oriented nanorods assembled in 1.4-micron width rings. (b) Complex ZnO nanostructures clustered at 10-micron square lattices.

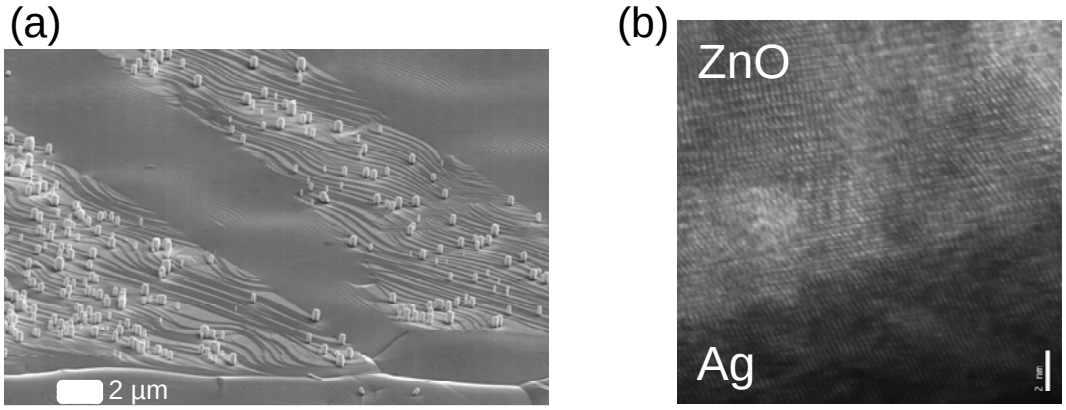

Figure 2. (a) Preferential nucleation of ZnO nanorods on (111) oriented Ag grains. (b) Abrupt and facetted ZnO-Ag interfaces.

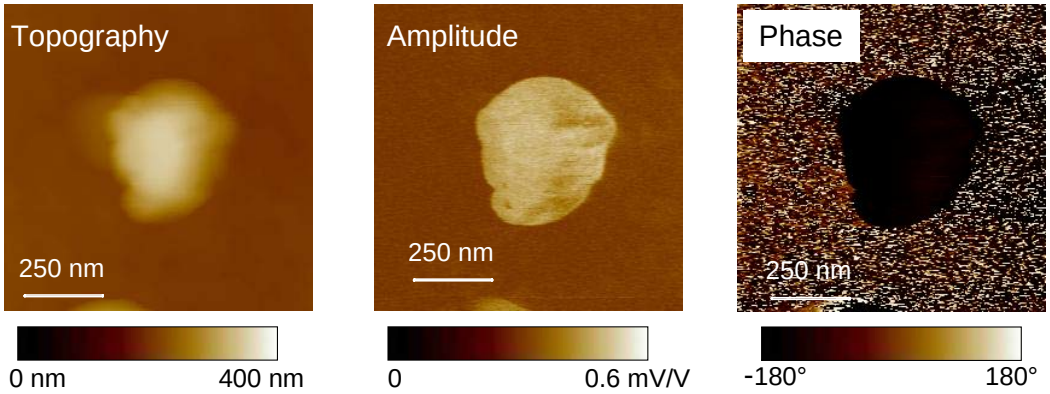

Figure 3. Piezoelectric force microscopy images of a single ZnO nanorod. 0° phase indicates <000$\bar{1}$> orientation and ±180° phase indicates <0001> orientation.

Porphyrin-Based Nanostructures for Electronic Applications

by **J. A. Shelnutt, Z. Wang, H. Wang, and C. J. Medforth**

Motivation—Nanostructures composed of porphyrin molecules were recently discovered at Sandia and their application to important catalytic reactions such as light-assisted water splitting to make hydrogen fuel is being actively investigated. Another unexplored realm of potential use of these multi-functional nanostructures is in nanoelectronics and nanophotonics, as previous research on porphyrin crystals and aggregates have demonstrated conducting and semiconducting properties. Photoconductivity and non-linear optical properties with visible light have also been demonstrated in porphyrinic materials. Now, with the advent of our well-defined porphyrin nanostructures like tubes, spheres, wires, rods, and structures with more complex morphologies, an opportunity presents itself for integration of these functional porphyrin-based nanostructures into electronic and optoelectronic devices.

Accomplishment—A variety of porphyrin nanostructures with different morphologies has been synthesized by ionic self-assembly of oppositely charged porphyrin tectons and by metal-coordination-induced self-assembly of functionalized porphyrins. We have extensively investigated the catalytic properties of these porphyrin nanostructures in the photocatalytic reduction of metal complexes to deposit zero-valent metals. In many cases, the metal deposits onto the porphyrin nanostructure to form a metal composite with the porphyrin nanostructure thus leading to functional nanodevices. For example, we have used porphyrin nanospheres that are platinized to reduce water to hydrogen using visible light as an energy source. Similarly, a porphyrin nanotube containing a gold nanowire and platinum particles on the outer tube surface is being investigated for water splitting to produce hydrogen and oxygen using solar energy. Figure 1 illustrates the water-splitting nanodevice base on the porphyrin nanotube and a transmission electron microscopy (TEM) image of the gold nanowire that has been grown in the nanotube. The photocatalytic activity that allows the nanowires to be grown in the tubes suggests that nanotubes and other porphyrin nanostructures will likely have interesting electronic and optoelectronic properties.

We are now actively investigating the electronic properties of porphyrin nanosheets and nanowires. For example, porphyrin nanosheets (see Fig. 2a) were synthesized and characterized by TEM. Atomic force microscopy (AFM) on conducting surfaces (with HP Palo Alto, CA) was used to determine the conductivity through the 10-nm thick nanosheets. In addition, nanowires composed of porphyrin nanofiber bundles (Fig. 2b) have been successfully deposited electrophoretically onto interdigitated electrodes for conductivity measurements and to determine their surface charge.

Significance—The integration of micro-electronics with unconventional nanomaterials such as self-assembled soft nanostructures is an important processing goal. The porphyrin-based nanostructures offer a unique opportunity for exploring bioinspired functional nanostructures and nanodevices and for discovering the means to incorporate them into conventional electronic and photonic devices.

Sponsors for various phases of this work include: DOE Office of Basic Energy Sciences Core Program and Center for Integrated Nanotechnologies (CINT), and Laboratory Directed Research & Development

Contact: John A. Shelnutt, Surface & Interface Sciences, Dept. 1114
Phone: (505) 272-7160, Fax: (505) 272-7077, E-mail: jasheln@sandia.gov

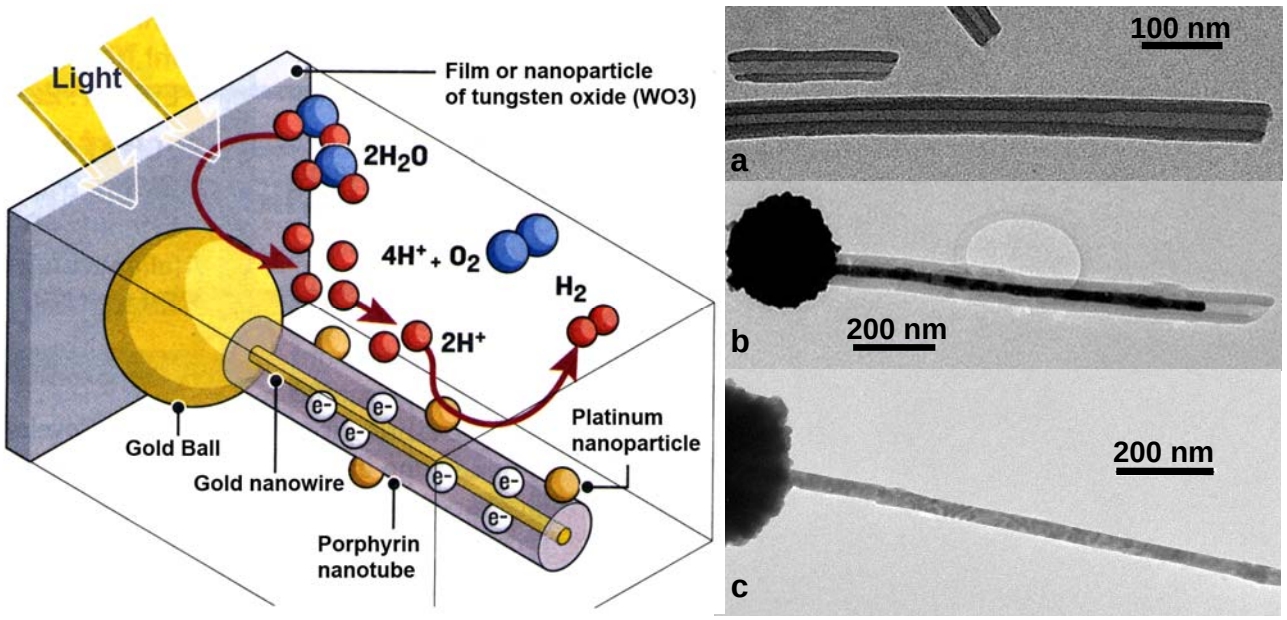

Figure 1. A proposed water-splitting nanodevice based on our photocatalytic porphyrin nanotube, TEM images of a nanotube (a), a gold nanowire grown inside the hollow core of a porphyrin nanotube (b), and a free standing gold nanowire after dissolving the porphyrin nanotube (c).

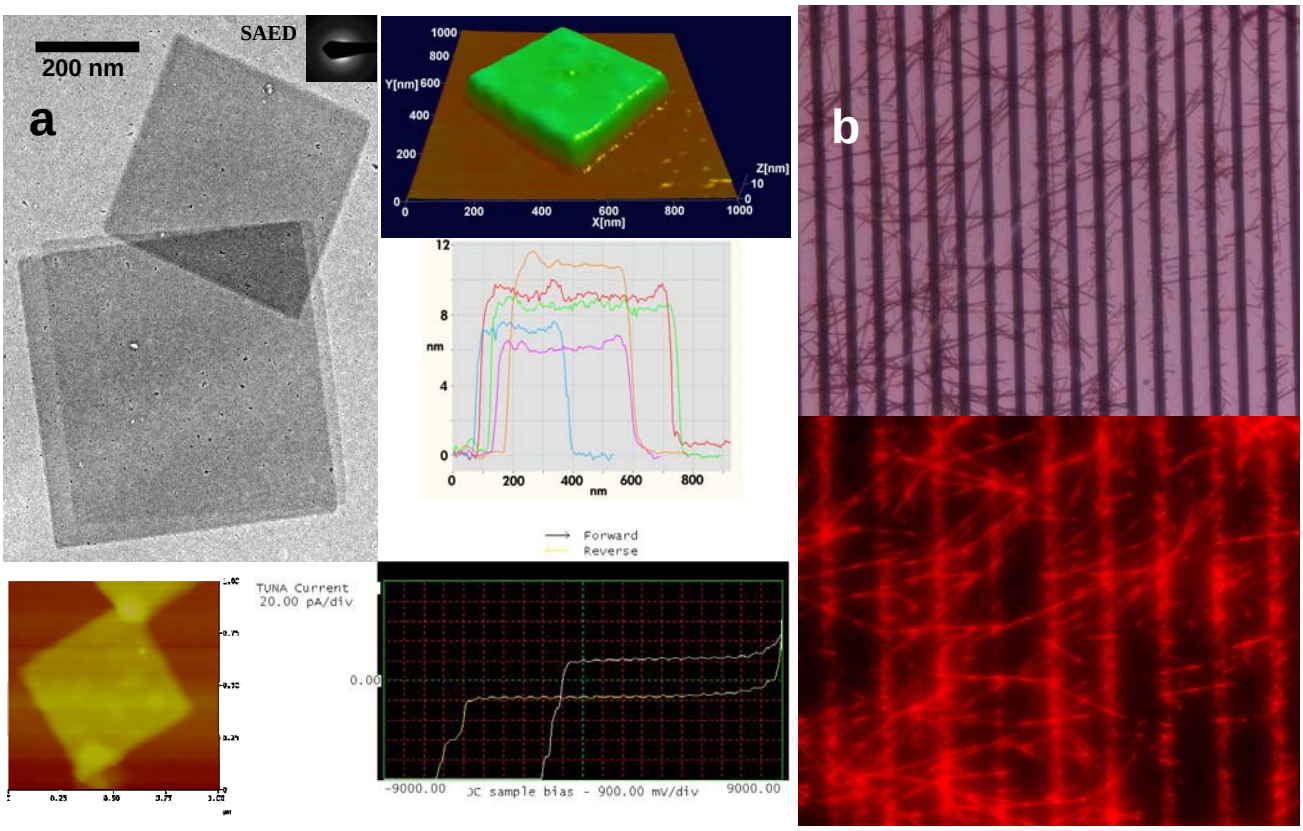

Figure 2. (a) TEM and AFM images of porphyrin nanosheets, AFM thickness profiles, and their current-voltages traces from AFM on silicon. (b) Optical (top) and fluorescence (bottom) microscope images of porphyrin nanofiber bundles electrophoretically deposited onto gold interdigitated electrodes.

Oxidation of the Copper (100) Surface Induced by Local Alkalization

by **N. Vasiljevic, R. G. Copeland and N.A. Missert**
Collaborators: L.T. Viyannalage and N. Dimitrov, SUNY at Binghamton

Motivation—It is generally known that the stability of metal surfaces can be greatly influenced by *localized phenomena* associated with the oxygen reduction reaction (ORR). The ORR is considered as one of the most important electrochemical reactions in the field of corrosion. The kinetics of the ORR processes often determines the general corrosion rate of metals and the damage evolution in many commercially important alloys. As the ORR proceeds on the copper surface, by either consuming hydrogen ions or generating hydroxide ions, the local pH can increase well above the solution bulk value, setting a pH gradient from the surface toward the bulk of the solution. Therefore, the ideal conditions for the oxidation to take place are created locally, even in acidic aqueous media for which the equilibrium thermodynamics rule out the possibility of stable oxide formation.

Accomplishment—Our work presents the first *in-situ* scanning tunneling microscopy (STM) study of the initial stages of Cu(100) oxidation occurring in *naturally aerated acidic solutions*. The presence of dissolved oxygen in the solution results in a very distinctive electrochemical behavior of the Cu(100) surface that is manifested by pairs of pronounced peaks not present in deaerated solutions with identical pH, Fig. 1. The observed difference is a clear manifestation of the kinetic effect of the ORR that results in local solution alkalization. The set of peaks observed in naturally aerated solutions represent the adsorption/oxidation surface processes taking place, while their pH-dependent behavior points toward the important role of oxygen species (O and OH^-) in the process of surface oxide formation. Following the surface structures and morphological changes using an *in-situ* STM, we showed how the extent of local alkalization and the concomitant extent of oxidation depend on experimental conditions: solution pH, potential and time of exposure. We focused our research on the initial stages of copper oxidation, known as underpotential oxidation, in a 0.1 M $NaClO_4$ solution of pH 2 and pH 4, Fig. 2. Quantitative analysis showed that in highly acidic solutions (pH 2), the surface actually experiences much higher pH of almost 7 to 8. *In-situ* STM results in pH 4 solutions revealed a striking similarity with the morphologies usually observed in alkaline solutions of pH 9 to 11. These results confirm the proposed local alkalization mechanism governing the stability of the copper surface.

Significance—In recent years copper surface stability became an increasingly important issue due to its varied applications in many fields of technological importance. Our knowledge of locally-induced copper oxidation will impact the technology of copper processing and design procedures in the electronics industry, help in understanding the corrosion behavior of copper-based alloys and eventually help in improving their corrosion resistance. This work provides an opportunity to generate a new body of knowledge that will enable development of many pH-controlled processes, playing a key role in the fields of solid-state synthesis, corrosion and chemical sensing. From the fundamental point of view, our work opens new pathways in studying and understanding the initial stages of noble metal oxidation.

Sponsor for various phases of this work include: DOE Office of Basic Energy Sciences

Contact: Natasa Vasiljevic, Nanostructure & Semiconductor Physics, Dept. 1112
Phone: (505) 844-0566, Fax: (505) 844-1197, E-mail: nvasilj@sandia.gov

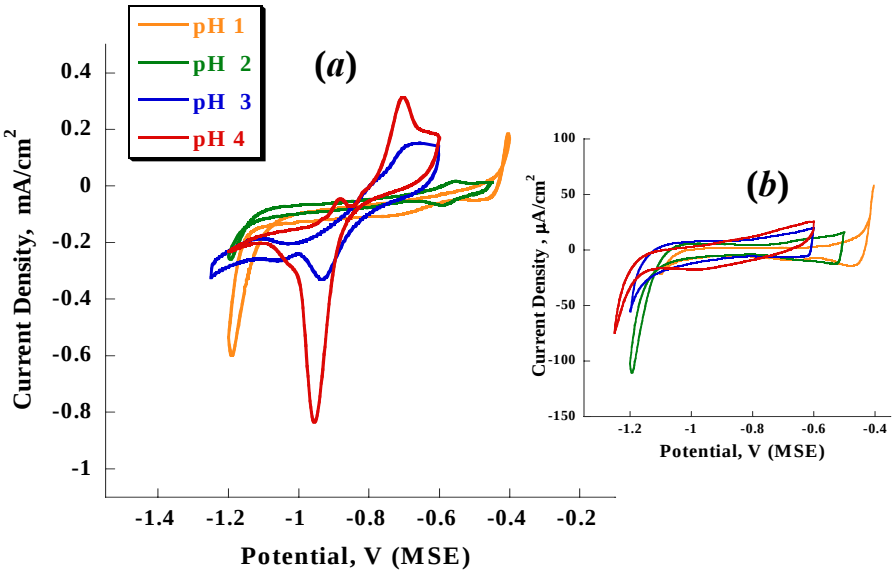

Figure 1. Cyclic voltammetries of Cu(100) in 0.1 M $NaClO_4$ solutions of different pH with a scan rate of 150 mV/s. (a) Naturally aerated and (b) deaerated solutions.

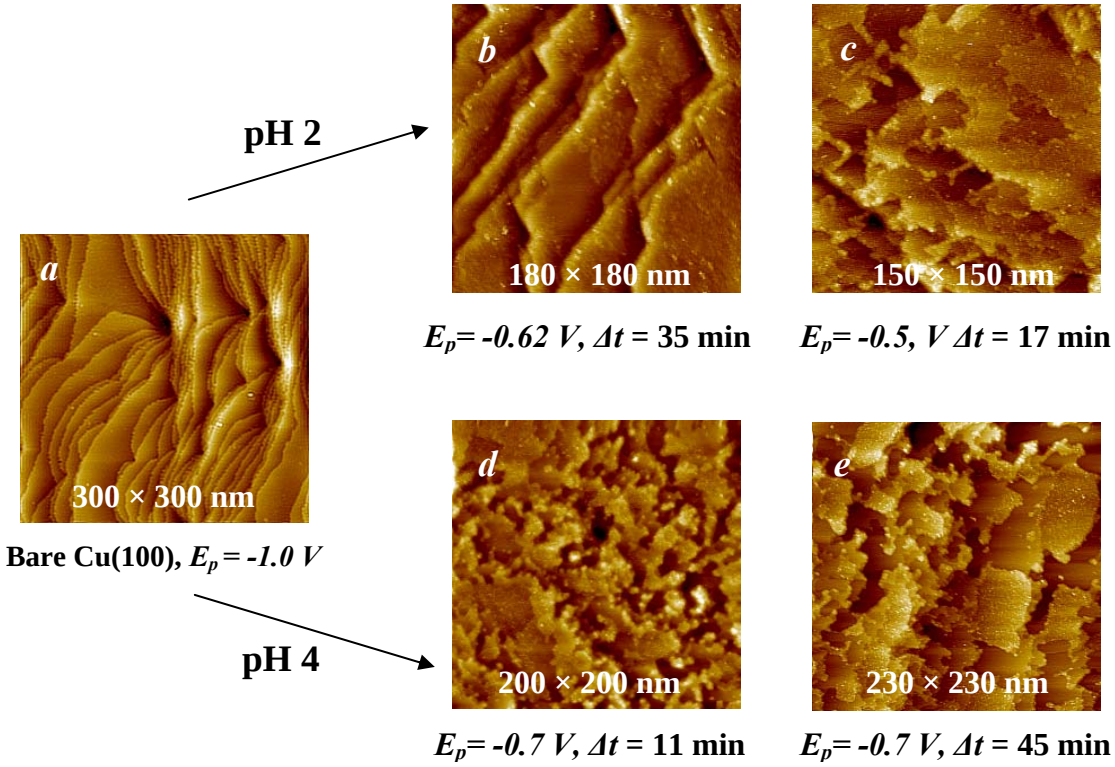

Figure 2. *In-situ* STM images of the Cu(100) surface at different potentials in 0.1 M $NaClO_4$ solutions of pH 2 and pH 4. (a) Bare surface. Potential dependant surface processes: (b) oxygen adsorption and (c) monolayer of underpotential Cu_2O growth in solution pH 2. (d) Underpotential and (e) bulk growth of Cu_2O in pH 4 solution.

Nanomechanics

Correlating Atomic Structure and Material Properties in Erbium Tritide

by **R. R. Wixom and D. R. Jennison**

Motivation—The well-known justifications for storing H in the form of metal hydrides remain valid for storage of deuterium (D) and tritium (T). As such, tritides and deuterides of Sc, Pd, Ti, Zr, and Er are commonly used in the nuclear industry as storage media. Here at Sandia ErT_2 is used to make targets in neutron generators. To ensure proper functionality in this application, it is critical that we understand the transient behavior of the material. A complicating factor is the short half-life (12.3 years) of T, which results in the substantial build-up of impurity He. This is concerning because, as an inert impurity, He is detrimental to the physical integrity of the host tritide and when released from the solid can be catastrophic to component functionality. In addition, O can be introduced during processing, creating unknown changes in material properties. Our goal is to develop a science-based understanding of this material and facilitate a predictive response to production and design needs.

Accomplishment—We have used first-principles density functional (DFT) calculations to study the structure of ErT_2 and atomic processes within the solid. The ideal ditritide has the CaF_2 crystal structure where Er sits at FCC lattice sites, T fills all of the tetrahedral positions, and the octahedral sites remain empty (Fig 1). This is known as the ß-phase, and is stable for a small range (+/- 0.1) of T/Er ratio centered at 2. Our calculations reveal that T prefers the tetrahedral, rather than octahedral, site by 0.75 eV. However, once the tetrahedral sites are filled, additional T loaded into the sample is forced into octahedral positions. Continued loading will eventually drive a phase change, but even small amounts of overloading have significant effects. For example, we found that the mechanism (and barrier) for T migration depends on the T/Er ratio. Morever, the mechanism involves concerted motion of both tetrahedral and octahedral T.

Experimental examination of ErT_2 thin-films indicates significant concentrations of O within the crystal. It is also observed that O-rich inclusions form during annealing. We find that O is most stable in the tetrahedral site, displacing T into the octahedral site and in doing so, O effectively increases the amount of overloaded (octahedral) T, changing the stability of the ß-phase and modifying the behavior of He. In agreement with observations, we predict that O will become mobile at 200 ˚C, and similar to T, the mechanism is one of concerted diffusion. Once O becomes mobile, oxide inclusions will nucleate.

It is known from aging studies, that He forms bubbles within the tritide that will eventually out-gas. However, the mechanisms for bubble formation and growth are not understood. We predict that He prefers to reside in the large empty octahedral sites where the electron density is low, and will diffuse just above room temperature (Fig 2). We are currently studying the formation of He clusters, the mechanism of bubble formation, and how impurities and octahedral T affect these processes.

Significance—Our DFT calculations add significant insight to the sparse literature on this material. Building on the fundamentals, we are moving toward a science-based understanding of how T, He, and O behave during processing and throughout the service life of the product.

Sponsor for various phases of this work include: Nuclear Weapons

Contact: Ryan R. Wixom, Nanostructure & Semiconductor Physics, Dept. 1112
Phone: (505) 845-7253, Fax: (505) 844-1197, E-mail: rrwixom@sandia.gov

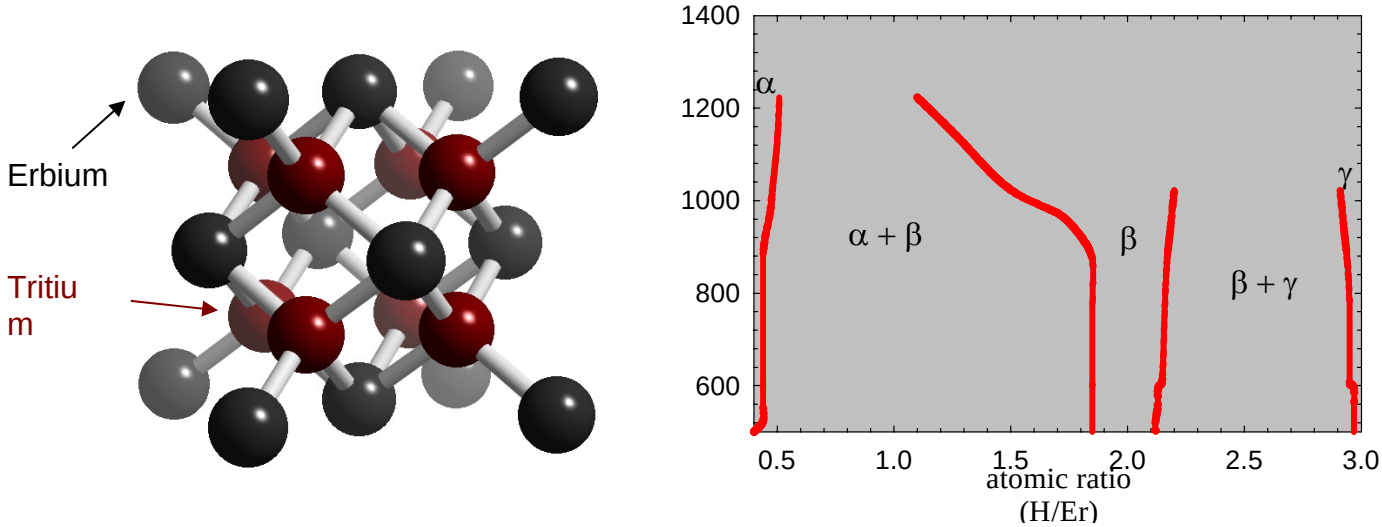

Figure 1. Left: Crystal structure of ß-phase ErT_2 showing ideal occupation of tetrahedral sites by tritium. The octahedral site, in the center of the unit cell, is nominally empty. Right: The phase-diagram of ErT_x.

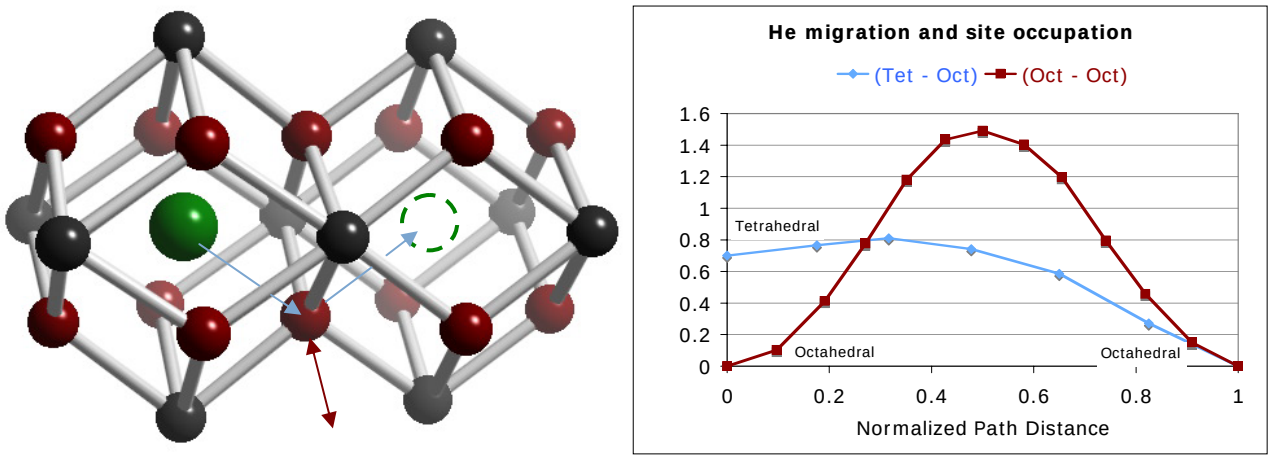

Figure 2. Left: Octahedral occupation of helium (green) and the minimum energy migration path for motion between octahedral sites. The blue arrows represent motion of the helium atom. The red arrow illustrates the temporary displacement of tritium while helium moves through the tetrahedral site into another octahedral position. Right: Data from nudged elastic band DFT calculations showing the relative energy of tetrahedral vs. octahedral site occupation as well as the barriers for two unique diffusion mechanisms. The blue line represents the rate-limiting barrier for the tetrahedral-octahedral mechanism shown left. The red line represents a direct octahedral-octahedral jump.

Mechanical Properties of Aging Erbium Tritide Films

by **J. A. Knapp and J. F. Browning**

Motivation—The mechanical properties of metals containing dispersions of small gas bubbles are of fundamental interest for understanding the effects of nanometer-sized inclusions on strength, and for applying materials to applications involving tritium, such as neutron tubes. The tritium slowly decays into ^{3}He, which is either released from the film, leading to vacuum problems in a sealed tube, or if retained, forms high pressure bubbles that may eventually fracture the film. Not only are the conditions leading to fracture of interest, but the mechanical properties of the layer before fracture are of fundamental importance for understanding how to control early ^{3}He release. We have been using fully tritiated ErT_2 model films deposited on Si to study the property changes to be expected for an aging neutron tube target film.

Accomplishment—We are using ultra-low load nanoindentation, combined with finite-element modeling (FEM) to separate the nano-mechanical properties of the 500 nm ErT_2 layers from those of the underlying substrate. The ^{3}He bubbles which form as the film ages act as barriers to dislocation movement, hardening the material, but not dramatically affecting the elastic properties. Figure 1 shows a TEM micrograph of one of the films 62 days after hydriding with tritium. The ^{3}He bubbles form as thin platelets oriented along (111) planes.

The nanoindentation/modeling approach to measuring the hardness and elastic properties of thin films has been developed over the last several years with application to a number of thin film material studies. These samples are indented in an instrument especially modified for tritium safety concerns, and then the data are fitted using FEM in order to separate the properties of the thin layer from the independently measured substrate properties. By modeling the ErT_2 layer as an isotropic, elastic-plastic solid with the Mises yield criterion, the nanoindentation data is shown to correspond to an increase of nearly 2x in strength after aging for over a year, followed by a slow decrease in strength with further aging. Figure 2 shows the deduced hardness of the layers as a function of aging after hydriding with tritium. The strength saturated at ~8.5 GPa, followed by a slow decrease with further aging.

The nanoindentation procedure also determines the elastic properties of the ErT_2, in particular the Young's modulus, from which the shear modulus can be calculated. The latter is very useful as an input parameter for models being developed to understand film aging, and is not available anywhere else for these materials. While the yield strength and hardness have changed substantially over the course of the study, the elastic properties have remained largely unchanged.

Significance—These measurements provide hitherto unknown information about the mechanical evolution of tritiated films as they age. Such knowledge is providing important insights into the aging process for these films, and when combined with ion beam analyses and electron microscopy, as well as models of film aging, will lead to solutions for problems associated with aging and ^{3}He release.

Sponsors for various phases of this work include: Nuclear Weapons and DOE Office of Basic Energy Sciences

Contact: James A. Knapp, Radiation-Solid Interactions, Dept. 1111
Phone: (505) 844-2305, Fax: (505) 844-7775, E-mail: jaknapp@sandia.gov

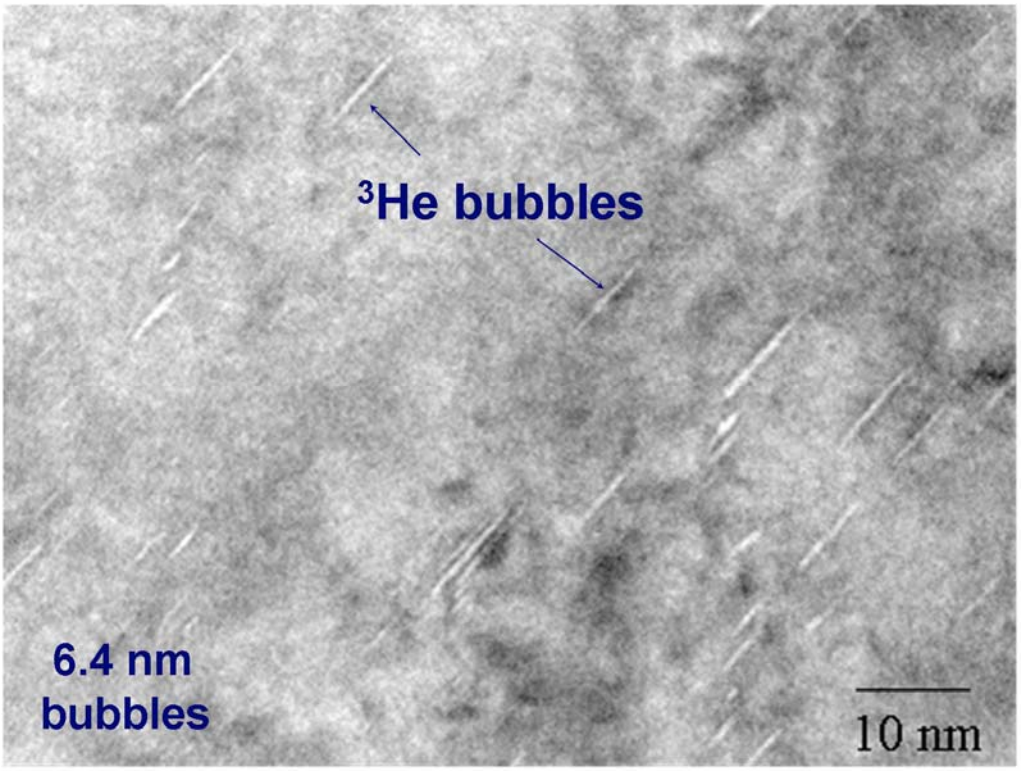

Figure 1. Bright-field Transmission Electron micrograph of ErT_2, in cross-section, along a {110} zone 62 days after hydriding with tritium. TEM done with G. Bond, New Mexico Institute of Mining and Technology.

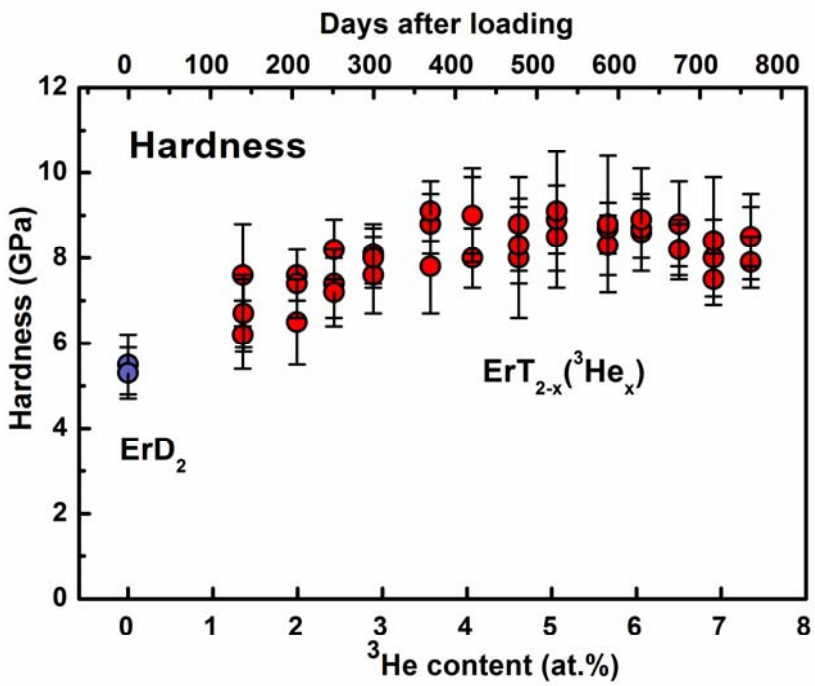

Figure 2. Material hardness determined by finite-element modeling of indentation data for ErD_2 and aging ErT_2.

Dynamical and Mechanical Behavior of Reversible Protein Hydrogels

by **David R. Heine[1] and Gary S. Grest, Sandia National Laboratories**
Darina Danova-Okpetu[2] and James L. Harden[3], Johns Hopkins University

Motivation—Hydrogels are hydrated polymer networks that are highly swollen by water. Natural protein hydrogels, such as the collagen-based extracellular matrix, are found in many biological systems. Recently, biomimetic protein hydrogels have been created from engineered telechelic proteins. Reversible gelation has been demonstrated for these telechelic proteins. These protein hydrogels have a variety of applications, including scaffolds for cell culture, contact lenses, and delivery devices for drugs. However, the molecular origins of gel formation are still poorly understood for these systems.

These engineered telechelic proteins have a triblock architecture composed of a central flexible domain with associating helical groups on each end (Fig. 1a). The helical ends are amphiphilic leucine zippers designed to reversibly assemble into trimeric bundles. As a result, solutions of the triblock proteins reversibly self-assemble into hydrogels (Fig. 1b). Our goal is to develop a coarse grained model to capture the secondary structure and reversible aggregation of these artificial proteins. This would allow us to study systems containing thousands of proteins, which would not be computationally tractable with an explicit atom model.

Accomplishment—We developed a coarse-grained bead-spring model for associating helix-coil-helix protein polymers where each bead represents an amino acid. Each pair of amino acids interacts via a Lennard-Jones potential. The end blocks of the triblock proteins adopt helical conformations as a result of hydrogen bonding along the axis of the helix. This behavior was incorporated into the coarse-grained model by replacing the standard harmonic dihedral potential with an asymmetrical potential that favors a 60° dihedral angle. The hydrophobic face of the amphiphilic helices was modeled by assigning every first and fourth bead of each heptad repeat attractive LJ parameters, which were adjusted to optimize the formation of trimer helix bundles. Subsequently, the self-assembly of three triblock proteins into hydrogels and their response to uniaxial and shear deformation were studied. Figure 2 shows a snapshot of such a hydrogel network. Figure 3 shows the temporal stress response of these hydrogels to a step uniaxial deformation.

The specific aims of this research are to relate the molecular conformation and association behavior of the protein elements to the amino acid sequences of the protein modules, to determine the dependence of hydrogel microstructure and viscoelasticity on the molecular characteristics of the protein constituents, and to study the thermodynamics of the reversible assembly process of the hydrogels.

Significance—Insights gained through this project on the sequence–structure–property relationships can have an immediate impact on the way biomimetic materials are designed. Although a model system, the insights gained from our system should be transferable to many biomaterials. Multi-scale modeling is an essential part of establishing connections between the material properties of the networks at the nanoscale and the molecular behavior of their constituents, as many important molecular and materials parameters span a wide range of time and length scales.

[1]Corning Incorporated; [2]Vrije Universiteit; [3]University of Ottawa
Sponsor for various phases of this work include: DOE Office of Basic Energy Sciences/Center for Integrated Nanotechnologies (CINT)

Contact: Gary Grest, Surface & Interface Sciences, Dept. 1114
Phone: (505) 844-3261, Fax: (505) 844-5470, E-mail: ggrest@sandia.gov

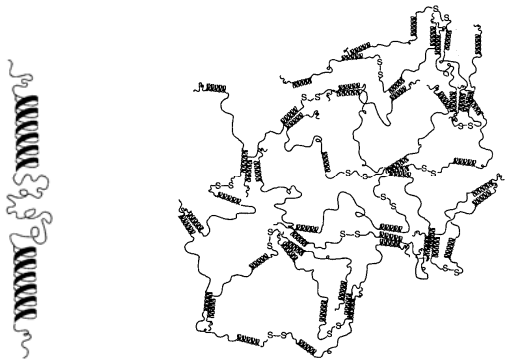

Figure 1. Triblock architecture of artificial protein (left) and proposed structure of associated proteins (right).

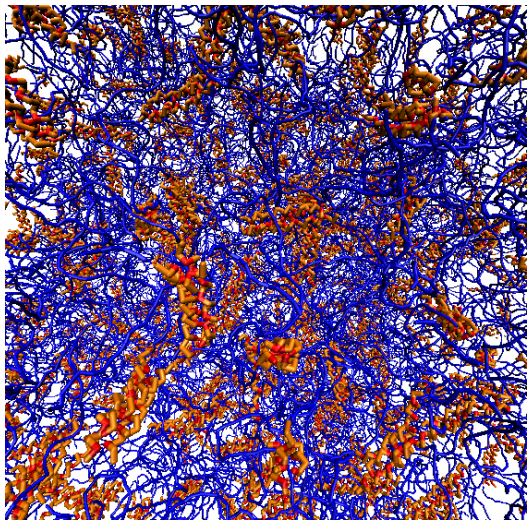

Figure 2. Snapshot from a molecular dynamics simulation showing the formation of doublet and triplet aggregates. The flexible middle segment of each protein is shown in blue and the outer helical segments are orange with the hydrophobic sites colored red.

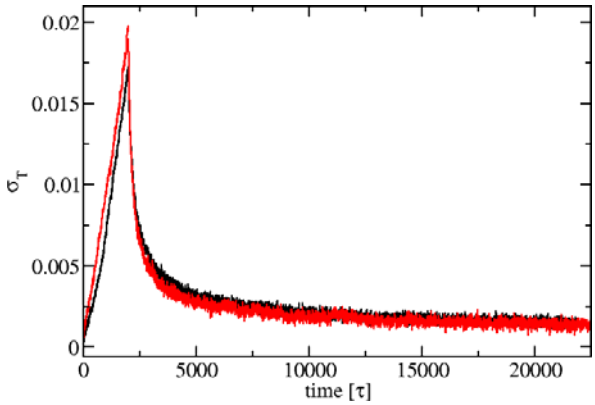

Figure 3. Tensile stress for hydrogels undergoing uniaxial strain for both flexible (black) and stiff (red) middle segments.

*Abnormal Grain Growth in Nanocrystalline Nickel**

by **D. M. Follstaedt, J. A. Knapp, and E. A. Holm**

Motivation—Metals with nanometer-sized grains exhibit improved mechanical properties such as higher strength and hardness. Methods to improve their ductility and toughness are needed, however, and their stability at elevated temperatures needs to be examined. Grain growth in nanomaterials is expected to occur readily due to their high content of grain boundaries, but the mechanism needs to be determined and understood.

Accomplishment—We have imaged nano-crystalline Ni formed by pulsed laser deposition during in situ annealing in the transmission electron microscope (TEM). We found that this material evolves by "abnormal grain growth," in which isolated grains grow into the surrounding nanocrystalline matrix that remains unchanged. This growth was seen at temperatures as low as 225°C and up to 400°C; it proceeded erratically, with radial growth rates of 6×10^{-3} to 6 nm/s. Figure 1 shows partially and fully regrown films. The abnormal growth appears to occur by dissolution of adjacent grains and regrowth, instead of their rotating to align with the atomic lattice of the growing grain as might have occurred. No preferred orientation was found for the abnormal grains. We also found that the 200 kV electron beam of the TEM enhanced the growth rate by imaging either before or during annealing.

A key discovery is that numerous defects were incorporated into the growing grains, including dislocations, stacking faults, twins, and stacking fault tetrahedra (Fig. 2), in contrast with the widely-held expectation of defect-free growth. Stacking fault tetrahedra, which form from vacancies, are especially notable since they have been found only in fcc metals that were quenched from high temperature, irradiated, or perhaps heavily strained. Since we observed them while at modest temperatures, imaged them with electrons too low in energy to displace atoms, and produced only small thermal strains, their presence requires a new formation mechanism.

To understand abnormal grain growth more fundamentally, mesoscale (continuum) simulations of the thermal evolution of nanocrystalline Ni grains that used orientation-dependent grain-boundary energies and mobilities were performed. Simulations using such properties exhibited abnormal grain growth of grains with no preferred orientation, just as observed.

Significance—Our Ni has relatively uniform grain size and few impurities, and is ideal for understanding growth in nanocrystalline metals. In addition to determining the mechanism, our modeling indicates that grain-boundary properties play a key role in producing this abnormal growth. Growth enhancement by the electron beam may result from disrupting oxides on the film surface that might pin grain boundaries. The stacking fault tetrahedra appear specific to grain growth in a nanocrystalline matrix; we hypothesize that the atomic density deficit of the numerous high-angle grain boundaries is a source of vacancies that become trapped within growing grains, leading to the tetrahedra. Atomic-scale modeling of grain growth in nanocrystalline Ni is planned, which may shed light on the detailed processes producing the tetrahedra. Finally, our work indicates that nanocrystalline Ni is unsuited for uses at temperatures of 225°C or more, which would alter its internal structure and properties. However, abnormal growth can be used to tailor structures with large grains in a nanocrystalline matrix, which could exhibit increased ductility.

*Collaborators: K. Hattar and Prof. I. M. Robertson, Univ. Illinois Urbana-Champaign

Sponsor for various phases of this work include: DOE Office of Basic Energy Sciences

Contact: David M. Follstaedt, Radiation-Solid Interactions, Dept. 1111
Phone: (505) 844-2102, Fax: (505) 844-7775, E-mail: dmfolls@sandia.gov

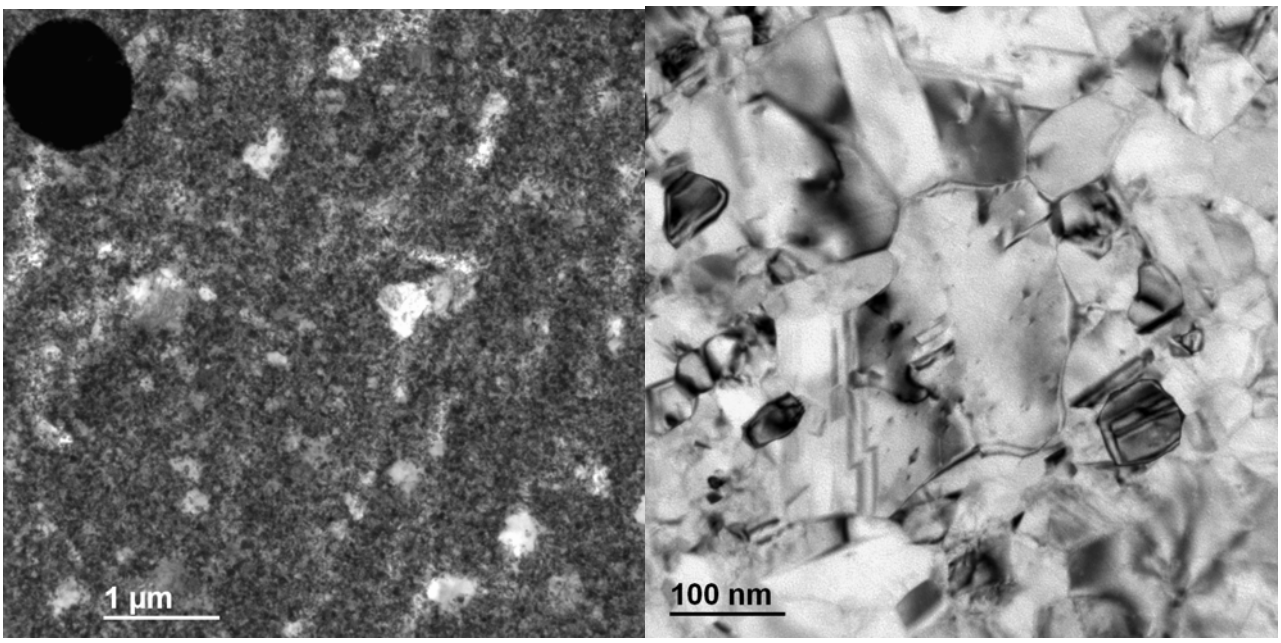

Figure 1. Left: TEM image of abnormal grains (light gray) in the nanocrystalline matrix (speckled); dark spot was used as a marker. The 150 nm-thick film was annealed 20 min. at 275ºC to partially react the film. Right: Image of near-fully reacted 80 nm-thick film, annealed 10 min. at 400ºC.

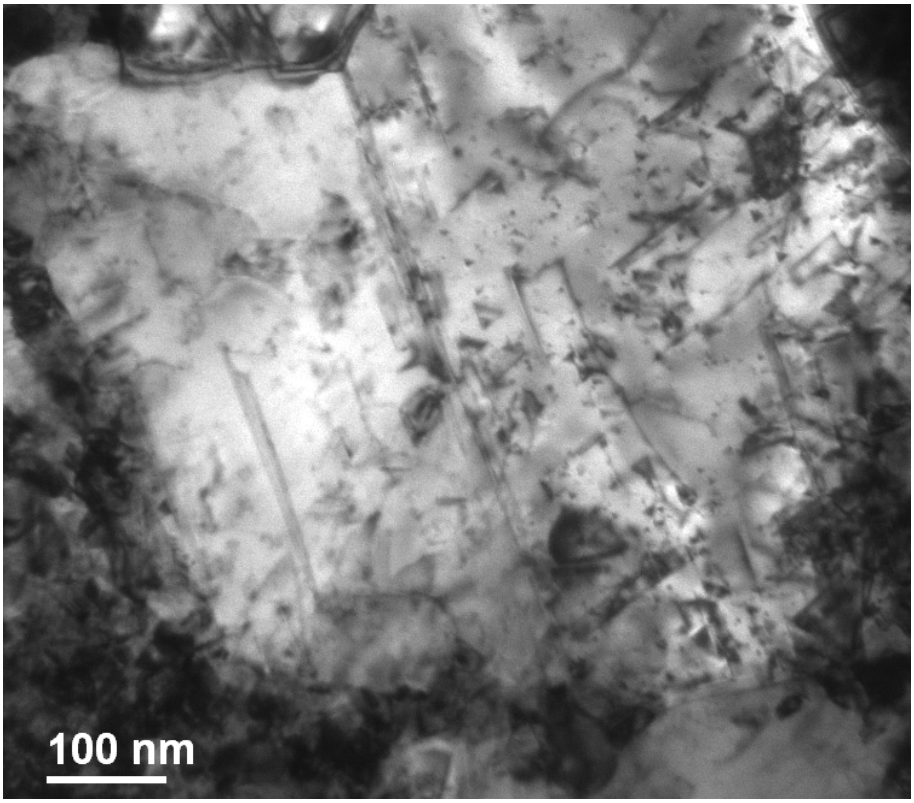

Figure 2. Higher magnification image of a grain from the film of Fig.1-left, showing many defects, including stacking fault tetrahedra (triangles). A large one (with stripes) is at the center.

Studies of the Nanotribology of Interfacial Water

by **J. E. Houston & P. J. Feibelman, in Collaboration with the X.-Y. Zhu Group at U. Minn.**

Motivation—The behavior of water near surfaces is critical to a wide range of important processes, such as protein folding, the stability of colloid suspensions, enzyme activity, swelling in clays and "stiction" in micro-electromechanical systems (MEMS). The nanometer-scale ordering of water near hydrophilic (water-loving) surfaces has been studied extensively using a variety of techniques. The results indicate that a change in intermolecular bonding often occurs, resulting in an increase in molecular ordering. Although thin water films on these surfaces normally don't form solid ice at room temperature, our studies suggest that they do possess properties distinctly different from those of the bulk liquid. An example, involving the viscosity of interfacial water, is presented here.*

Accomplishment—We have used the unique, Sandia-developed Interfacial Force Microscope (IFM), a quantitative and mechanically-stable scanning force-probe technique, to study the viscous properties of adventitious water confined between a tip and substrate, both hydrophilic. The relative humidity (RH) was varied, and measurements of both normal and lateral forces imposed on the tip were recorded as it slowly approached the substrate. The lateral force, or friction force, was measured by modulating the tip position laterally and obtaining the force signal by synchronous detection. We observed a friction force prior to tip/substrate contact, indicating that the interfacial water had a significant level of viscosity, which opposes tip motion. Figure 1 shows the results for a lateral modulation of ~25 Å at a frequency of 100 Hz under a RH of 20%. The red curve shows the normal or adhesive force. The sudden negative jump in force at a relative separation of ~42 Å indicates contact between the water coatings on tip and substrate, giving rise to an attractive meniscus force. This force increases until the two surfaces make contact, then rapidly turns repulsive (positive). A small viscous-friction force is observed due to the meniscus. At ~23 Å, however, the friction force begins a rapid rise, indicating contact between the interfacial water layers. A model fit to this rise, based on a formula derived by P. J. Feibelman (1114), yields a value for the viscosity of the interfacial water a million times greater than that reported for bulk water and implies a significant level of water ordering near the two surfaces. Approximately this same value has been found for four samples differing in substrate material and surface functionalization. In contrast, if the two surfaces are functionalized with hydrophobic (water-hating) monolayers, as shown in Fig. 2, there is no indication of a viscous interfacial layer and the after-contact friction is very low (these monolayers are excellent lubricants). However, the reasons for the friction decrease after the peak at ~19 Å has not yet been fully explained.

Significance—These measurements are the first to show clearly the remarkable tribology of interfacial water. They motivate an expansion of efforts to determine the root cause of the behavior and its implications in many areas where it may have dramatic consequences, e.g., in controlling the flow characteristics of water desalination membranes. Recent IFM developments have resulted in greater sensitivity and simplified operation. One envisioned application of the new capability is the quantitative measurement of friction and drive-train forces at various locations in complex MEMS devices, opening a smooth path to device qualification and facilitating the diagnosis of root causes in a failure–analysis setting. *[Phys. Rev. Lett. **96**, 177803 (2006)].

Sponsors for various phases of this work include: DOE Office of Basic Energy Sciences and Nuclear Weapons/Enhanced Surveillance Campaign

Contact: J. E. Houston, Surface & Interface Sciences Dept., 1114,
Phone: (505) 844-8939, Fax: (505) 844-5470, E-mail: jehoust@sandia.gov

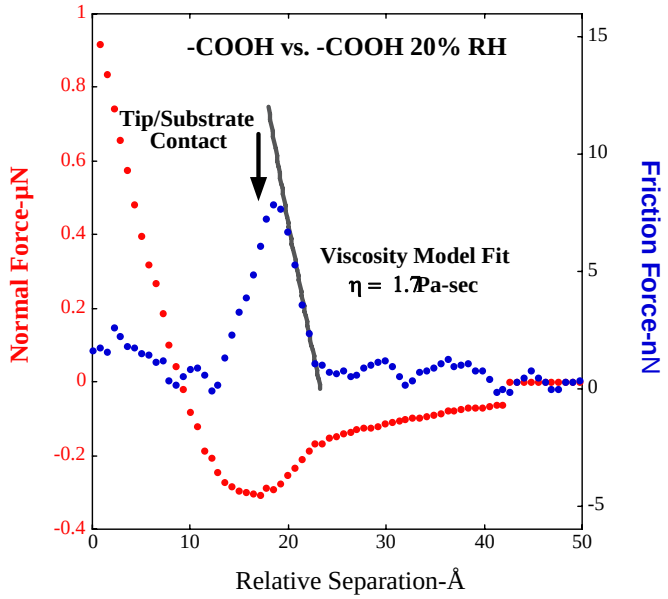

Figure 1. Normal (red) and viscous-friction forces (blue) plotted against relative interfacial separation for an Au tip and substrate functionalized by hydrophilic monolayers having carboxylic acid end groups under a 20% relative humidity. The solid line is a model fit according to the Feibelman formula. The model fit results in an interfacial water viscosity of 1.7 Pa-sec. This value is approximately one million times larger than that reported for bulk water. The significant level of the adhesive interaction is indicative of the hydrogen bonding capabilities of the acid end groups.

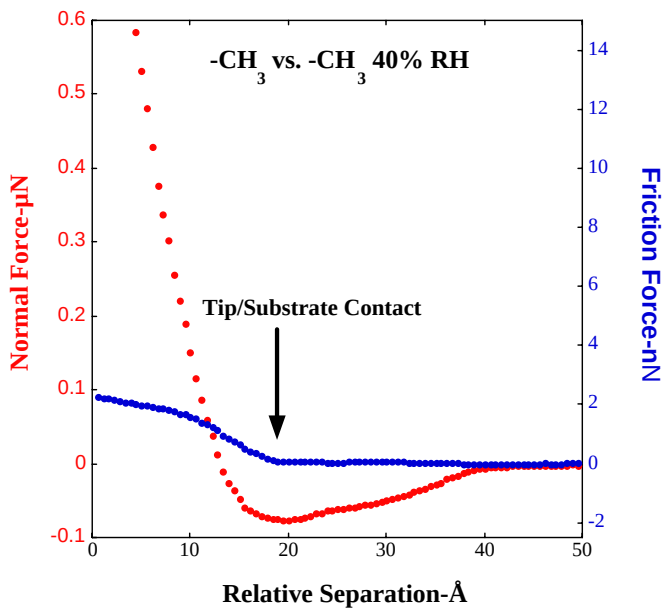

Figure 2. If the monolayers are terminated by hydrophobic (water hating) methyl groups, the friction is very low (even if the data is taken at 40% RH) and is appreciable only after the two surfaces have come into mechanical contact. Notice also, that the adhesive interaction, judged by the maximum negative normal force, is considerably less for the -COOH/-COOH interaction of Fig. 1 due to the lack of chemical bonding in the $–CH_3/–CH_3$ case.

Electromagnetic Radiation: Generation, Detection, & Spectroscopy

Optical Damage Characterization of Pure and Yb^{3+}-doped Fused Silica

by **Arlee V. Smith and Binh T. Do**

Motivation—There are several nonlinear processes that limit the pulse energy that can be transmitted by an optical fiber. They include stimulated Raman and Brillouin scattering, self focusing, and permanent damage to the glass caused by the optical field. These all interact to some extent to limit the transmissible energy. However, optical damage is the process that sets an ultimate limit that cannot be avoided. It is also the least understood and quantified of the processes. The literature on the subject has many contradictory observations and claims. Our goal is to carefully characterize optical damage in pure silica and in the Yb^{3+} doped silica that is used in fiber lasers and amplifiers.

Accomplishment—We fine tuned a Q-switched Nd:YAG laser so it produced exquisite pulses that are highly reproducible from pulse to pulse and have a smooth, nearly Gaussian temporal profile of 8 ns duration, and a lowest order Gaussian spatial profile. Pulses of varied energy are focused to a spot approximately 15 μm in diameter in pure and doped fused silica samples, and the threshold for damage is measured. Bulk damage is observed when the focus is deep inside the sample, and surface damage occurs when the focus lies near the entrance or exit face.

We took micrographs of bulk and surface damage under various conditions. Examples of bulk damage at two energy levels near the damage threshold are shown in Fig. 1. Damage initiates at the point of focus which is the center of the upper bloom in the images. This takes place on a sub nanosecond time scale, and the remainder of the pulse energy causes upstream growth of the damage. The initial damage strikes a plasma at the focus which then absorbs incoming laser energy on the upstream boundary causing upstream damage grow.

Figure 2 shows that the transmitted light is cut off abruptly in less than a nanosecond when the plasma first reaches critical density. Further, as the pulse energy is increased the damage always occurs at the same power, indicating that there is a well defined damage irradiance threshold. The variation of the threshold is 5% or less from one pure silica sample to another. For fiber performs we measured damage thresholds in the cladding which is undoped and in the doped core and find the threshold is approximately 20% higher in the core.

Deriving the damage threshold from these measurements requires a substantial correction to account for self focusing. This is done using numerical models of beam propagation that includes self focusing induced by an instantaneous n_2 from the Kerr effect, to find the degree of irradiance enhancement on the beam axis near the focus. There is another, smaller contribution to n_2 from electrostriction as well.

Significance—A major goal of the fiber laser effort at Sandia is to extract as much energy as possible from a fiber amplifier in nanosecond pulses. Another Sandia application requires efficient transmission of multi-mJ, nanosecond pulses through silica fibers. Self focusing and optical damage limit the energy in this application as well. We have established the precise irradiance limits for pure and doped silica, and we have provided clear explanations of the damage mechanism. Surface damage is important to both of these programs as well, and will be studied next.

Sponsors for various phases of this work include: Laboratory Directed Research & Development and Nuclear Weapons

Contact: Arlee V. Smith; Laser, Optics, & Remote Sensing; Dept. 1128
Phone: (505) 844-5810, Fax: (505) 844-5459, E-mail: arlsmit@sandia.gov

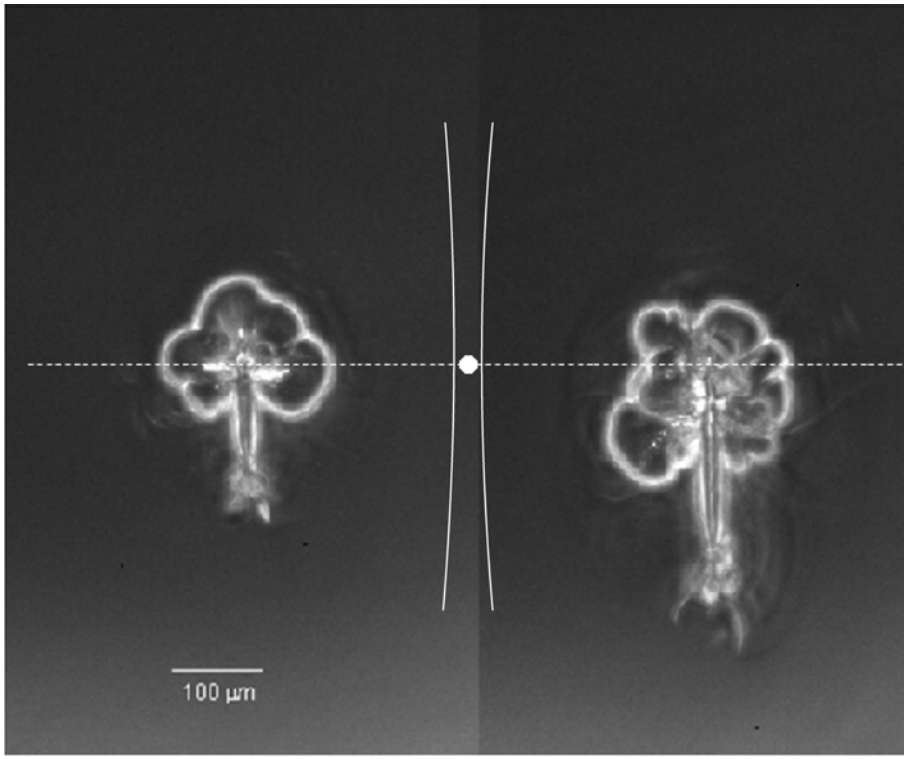

Figure 1. Damage morphology near the damage threshold. Light travels upward with the focal shape indicated by the curved lines. Damage starts at the beam waist and grows downward until the pulse passes or the plasma terminates due to weakening light away from the focus.

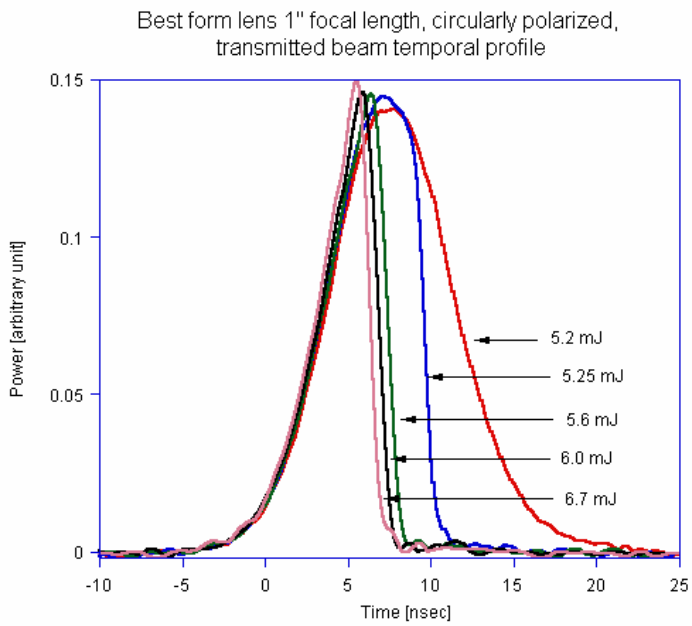

Figure 2. Time profiles of transmitted light pulses of various energy. Damage always occurs at precisely the same irradiance level.

High Efficiency Ultraviolet Light Generation

by **D. J. Armstrong and A. V. Smith**

Motivation—Tunable, high-pulse-energy ultraviolet (UV) light is required for air- or satellite-based remote sensing missions including standoff detection of chem-bio agents, verification of nonproliferation of weapons of mass destruction, and for measuring stratospheric ozone concentration. However, designing tunable UV sources for deployment in these platforms remains a serious technical challenge, where high efficiency and reliable operation under widely varying environmental conditions are of utmost importance. Some light sources can use simple harmonic conversion alone to access the UV, with 355 nm and 266 nm being familiar examples for Nd:YAG. However non-harmonic tunable UV sources require additional nonlinear optical frequency converters such as optical parametric oscillators (OPOs). Most conventional OPO designs fail to meet specifications for conversion efficiency and durability required for airborne or satellite deployment. Recent advancements in OPO technology help address these shortcomings.

Accomplishment—Using the Sandia-patented RISTRA OPO (rotated image singly-resonant twisted rectangle) shown in Fig. 1 we have developed a Nd:YAG pumped UV generation system that is efficient, robust, and resistant to optical damage. The image-rotating RISTRA is ideal for UV generation because of its excellent beam quality. With its non-planar geometry, the RISTRA cavity requires no mirror adjustments so its mechanically stable quasi-monolithic design is ideal for remote sensing applications, as well.

Our UV generation system uses sum-frequency generation (SFG) to mix the 803 nm signal wave of the OPO with the 532 nm pump wave to generate 320 nm light. Its key features include image rotation, which works in conjunction with crystal birefringence to produce excellent beam quality; pulsed injection seeding, which reduces cavity build-up time so the 532 nm pump and 803 nm signal temporal profiles match in time; and the use of large diameter beams with flat-topped spatial profiles for optimum mixing efficiency and reduced risk of optical damage.

Our goal is high conversion efficiency in the OPO and in subsequent SFG stages. The measure of OPO efficiency is pump depletion, which quantifies conversion of pump energy to the OPO signal and idler waves. Figure 2(a) shows unusually high depletion of 88% resulting from pulsed injection seeding and the use of flat-topped beams. High-energy, high-efficiency SFG requires a large diameter flat-topped near-field spatial profile with minimal wavefront distortion, as shown in Figs. 2(b) and 2(c). The optical-to-optical efficiency of our system (1064 nm to 320 m) exceeds 20%, and its maximum UV energy is approximately 200 mJ.

Significance—High-efficiency, high-energy UV generation using stable, mechanically robust RISTRA OPOs opens the door to a variety of remote sensing applications. When combined with diode-pumped all-solid-state pump lasers, RISTRA-based UV generators can achieve high overall system efficiency in small packages that are suitable for deployment in the harsh environments of airborne- or satellite-based platforms.

Sponsors for various phases of this work include: National Aeronautics & Space Administration (NASA) Langley Research Center (LaRC), and Nuclear Weapons

Contact: Darrell J. Armstrong; Lasers, Optics, & Remote Sensing; Dept. 1128
Phone: (505) 844-4757, Fax: (505) 844-5459, E-mail: darmstr@sandia.gov

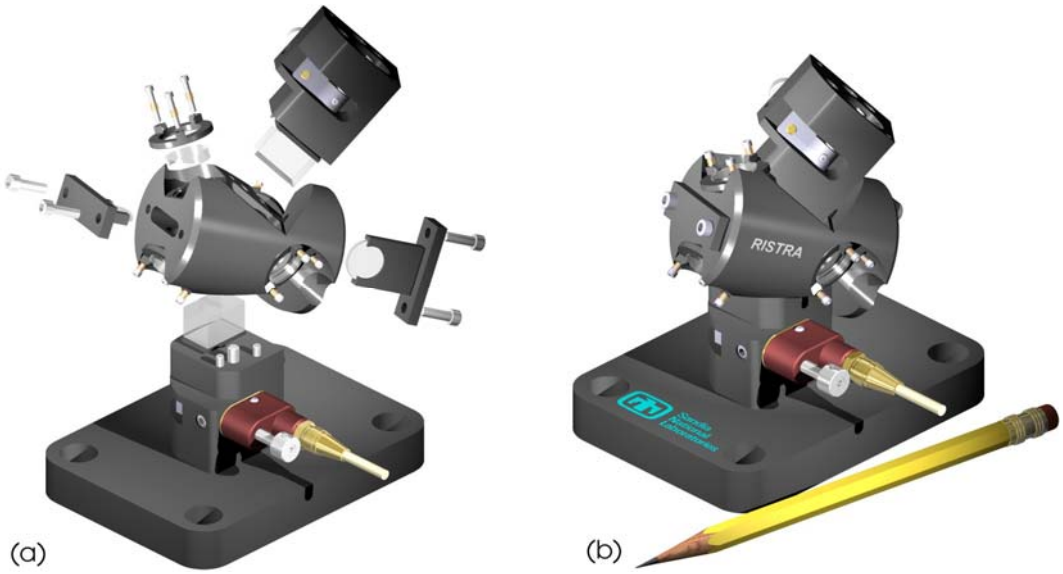

Figure 1. (a) Exploded view of a two-crystal RISTRA OPO, denoting rotated image singly-resonant twisted rectangle. Owing to its non-planar geometry cavity mirrors of the RISTRA require no tilt adjustments and are held against machined faces on the cylinder by spring-loaded retainer rings. λ/2 retardation plates insert into each end of the cylinder to control intra-cavity polarization. For UV generation the OPO is pumped by 532 nm light from an injection-seeded Nd:YAG laser, with potassium-titanyl-arsenate crystals generating an 803 nm signal and 1576 nm idler. The OPO is pulse-injection-seeded for high efficiency, and the pump and pulsed-seed beams have flat-topped spatial profiles. (b) Assembled two-crystal RISTRA OPO. The length of the cylindrical body is 1.97 in.

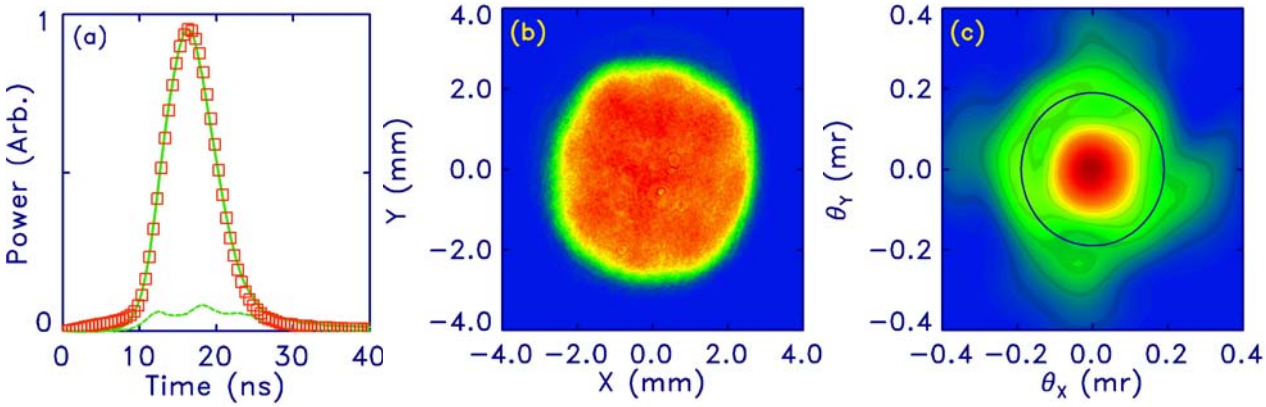

Figure 2. (a) A comparison of depleted (dashed) and undepleted (solid) pump pulses showing 88% conversion of pump energy to the signal and idler waves. Red boxes show the resulting signal pulse, normalized to the undepleted pump. Near identical pump and OPO signal temporal profiles enhance SFG efficiency through their increased temporal overlap. (b) Flat-topped near-field OPO signal spatial fluence profile, and (c) corresponding far field spatial fluence profile. The blue circle in (c) denotes the first Airy null for the near-field profile in (b) and contains approximately 60% of the energy in the far-field. Using an OPO beam having a flat-topped spatial profile and low wavefront distortion also enhances SFG efficiency.

Gas-phase Absorption Spectrum of 2, 4 DNT Explosive from 0.05 to 1.5 THz Using THz Time-Domain Spectroscopy

by **R. Foltynowicz and R.E. Allman**

Motivation—Terahertz (THz) spectroscopy is emerging as a powerful technique to identify and characterize molecular species. Due to recent advances in femtosecond lasers and optical materials, the THz radiation band from 0.1 to 10 THz is now routinely accessible. Spectroscopically, this is a new and unexplored portion of the spectrum that is rich in unique molecular information. In addition, the propagation properties of THz radiation through the atmosphere are potentially attractive for remote sensing of explosives.

From our previous studies on the propagation of THz radiation through the atmosphere, we have learned that the atmosphere is not as opaque as once thought. There are many THz transmission windows within the atmosphere. However, to capitalize on the THz transmission properties of the atmosphere for explosive vapor sensing, it is important to determine if spectra exist for these molecules within these windows. Therefore, our interests lie in characterizing gas-phase explosive materials to guide the development of novel THz devices for remote sensing of explosives.

Accomplishment—Recently, we have measured the first known gas-phase absorption spectrum of the explosive 2, 4 dinitrotoluene (DNT) from 0.05 to 1.5 THz using time-domain spectroscopy. Figure 1 shows the characteristic signature of 2, 4 DNT with a spectral resolution of 3 GHz. The broad absorption profile from 50 GHz to 600 GHz is the pure rotational spectrum of 2, 4 DNT. Due to the large moments of inertia for the DNT molecule, the density of lines in the rotational spectrum is large, which consequently produces broad absorption. The broad absorption profile in the DNT spectrum was validated by calculating the pure rotational spectrum using an asymmetric rotor model. The result from the calculation is shown in Fig. 2. The calculation reproduced the measured spectral width of the broad absorption, and it peaked at 275 GHz compared to 240 GHz from the measured spectrum.

The DNT spectrum displayed unexpected fine structure that was superimposed on the broad absorption profile. This structure could be due to the interaction between the internal rotation of the substituent groups and the torsional modes of vibration in the molecule. The presence of these features may provide an opportunity to uniquely identify explosives based upon their absorptions in the THz region of the spectrum.

The explosive material used in the experiments was pure crystalline solid which was converted into the gas phase by heating a unique temperature-controlled gas cell to 145° C. At this temperature, most of the explosive material was converted into the gas phase, and the static pressure measurements were made utilizing 250 to 610 mtorr of DNT.

Significance—Our gas phase absorption measurements of 2, 4 DNT are the first of their kind in the spectral region 0.05 to 1.5 THz. In the terahertz community, many have proclaimed terahertz spectroscopy as the tool to detect and identify explosive material, but no gas phase work has been done. Our results demonstrate the potential of using terahertz spectroscopy for explosive detection and identification. This work will guide the development of novel THz sensors and detectors capable of detecting explosive vapors.

Sponsors for various phases of this work include: Nuclear Weapons, Laboratory Directed Research & Development, and Work for Others/Transportation Security Administration & Technical Support Work Group

Contact: Robert Foltynowicz; Lasers, Optics, & Plasma Sciences; Dept. 1128
Phone: (505) 844-8148, Fax: (505) 844-5459, E-mail: rjfolty@sandia.gov

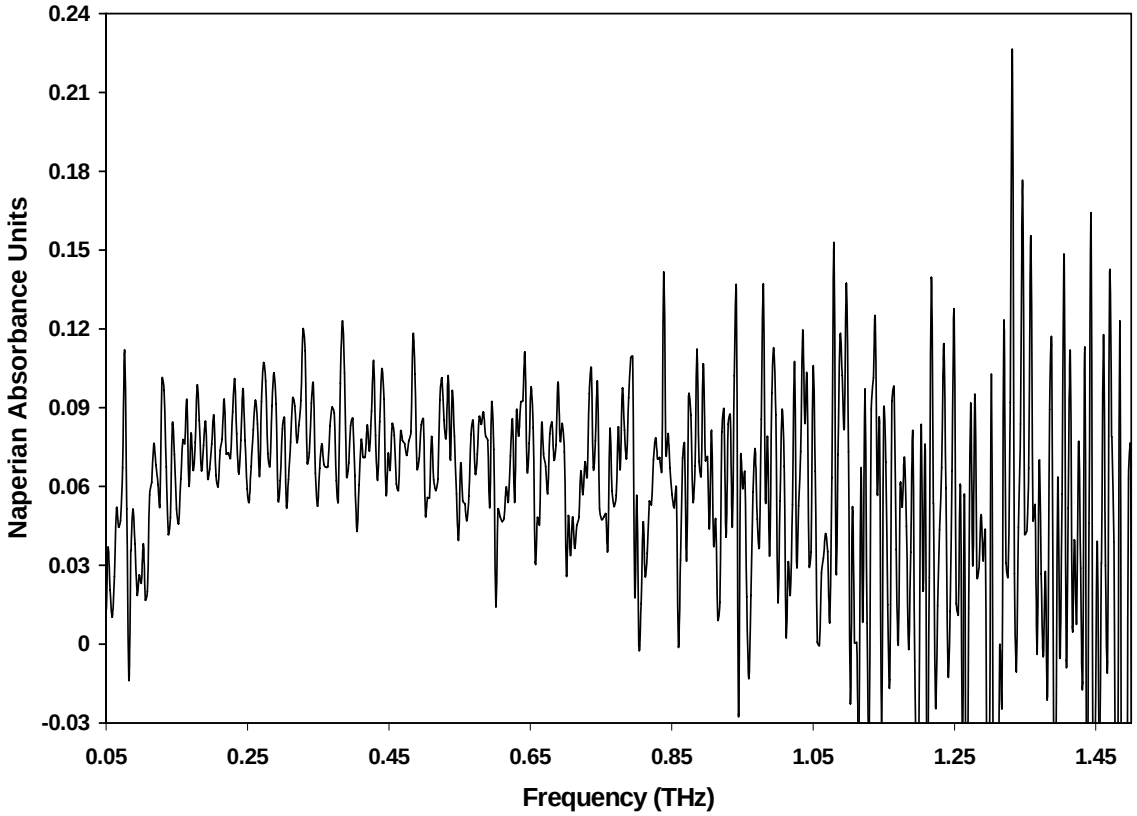

Figure 1. Measured absorption spectrum of gas-phase 2, 4 DNT from 0.05 to 1.5 THz.

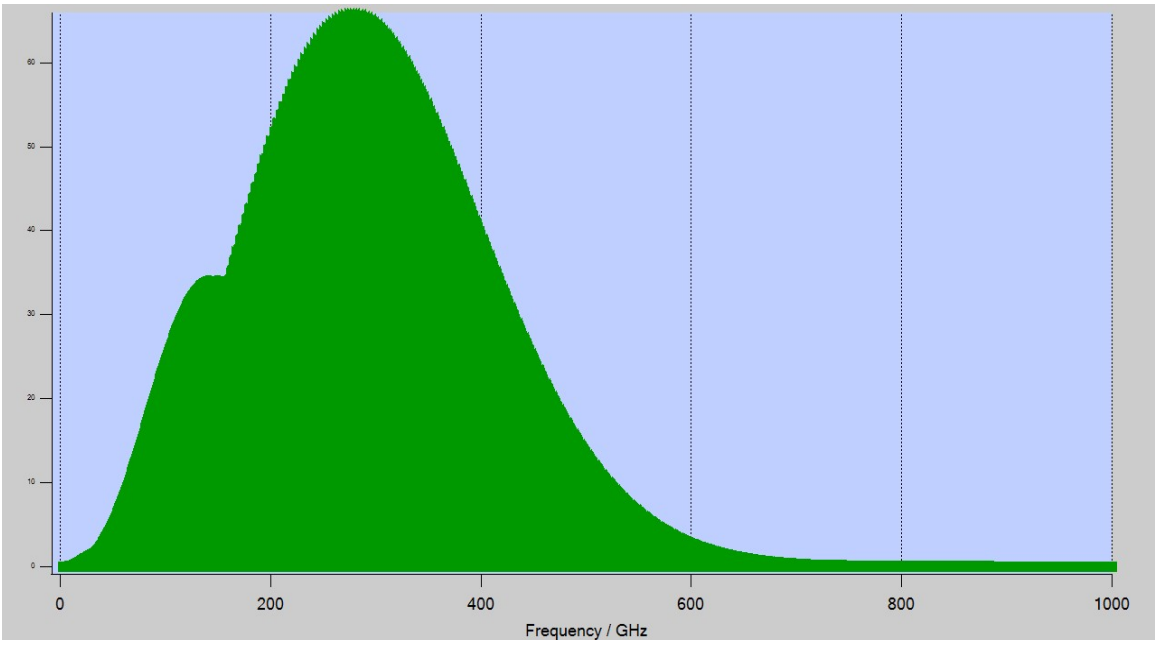

Figure 2. Calculated pure rotational spectrum of gas-phase 2, 4 DNT from 0.05 to 1.5 THz utilizing an asymmetric top model.

Single Quantum Well THz Split Grating-Gate Detectors

by **E. A. Shaner**

Motivation—The terahertz (THz -300μm wavelength or 10^{12}Hz) portion of the frequency spectrum lies in a gap between where conventional electronics can be driven and where optical transitions in materials and devices can be easily manipulated. There is a great deal of interest in the THz generation and detection as it enables a variety of national security applications from seeing through clothing to explosives detection. On the detection side of this problem, plasmon based grating-gate detectors have been explored as a tunable detector of THz radiation.

Accomplishment—The split grating-gate detector is a depletion mode field-effect transistor (FET) structure fabricated from high mobility modulation doped single or double quantum well material (inset Fig. 1). As shown, the device consists of source and drain electrical contacts along with a set of 3 gates; a source gate, drain gate, and a finger gate which is just a single strip dissecting the device. Plasmons are collective excitations of electrons that can resonate at frequencies orders of magnitude higher than can be reached by conventional electronics. The resonant frequency of a plasmon is set by the carrier density underneath the source and drain gates. The finger gate is independently biased beyond the pinchoff voltage in the material and it tunes the responsivity of the detector. IV traces are shown in Fig. 1 at several different finger gate biases. Beyond the pinchoff voltage (approximately -0.7V), the device takes on diode-like characteristics.

Previous work demonstrated that plasmon detectors using only a single gate worked as tunable THz detectors. However, the noise equivalent power (NEP), which defines how good a detector really is, was only 10^{-5} W/√Hz; our goal is to reach an NEP of 10^{-9}-10^{-10} W/√Hz.

The photoresponse of the single well split gate detector to 432μm radiation, at several different device operating points, is shown in Fig. 2a. The resulting responsivity of several V/W and an NEP of 10^{-7} W/√Hz is a 3 order of magnitude improvement in the photoresponse magnitude and 2 orders of magnitude improvement in NEP when compared to the standard single gate plasmon detector (inset Fig. 2a). By measuring detectors of various sizes, we have also found that only a very small portion of the detector, as low as 5% around the single finger gate, is optically active. This bodes well for other device designs that can take advantage of the split gate mechanisms while maintaining a larger active area. For example, a suspended version of this detector has been made from double well material (which does not perform as well as single well material) and demonstrated a NEP of 10^{-8} W/√Hz. In the past year, we also demonstrated video-rate spectral sweeps using the single well split-gate detector as shown in Fig. 3.

Significance—Plasmon detectors have been demonstrated as on-chip THz spectrometers with no moving parts. The primary obstacle to their practical use is the NEP. This recent work made several large steps towards our targeted NEP of 10^{-9}-10^{-10} W/√Hz. We currently see no obstacles to further developing these detectors to reach this goal.

Sponsors for various phases of this work include: Laboratory Directed Research & Development and Defense Advanced Research Projects Agency (DARPA)

Contact: Eric Shaner, Semiconductor Material & Device Sciences, Dept 1123
Phone: (505) 284-5636, Fax: 844-3211, E-mail: eashane@sandia.gov

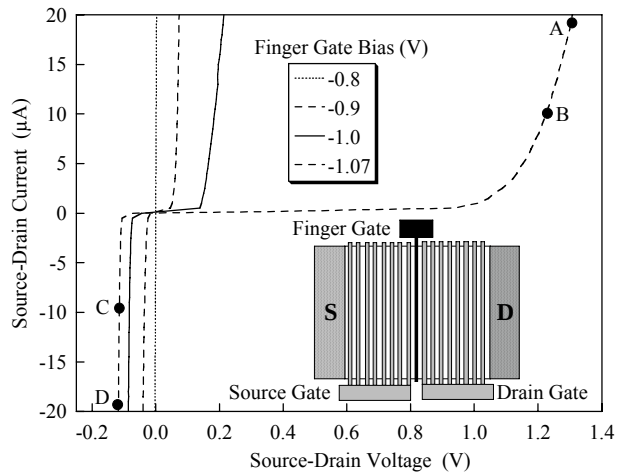

Figure 1. Source-drain current-voltage characteristics (in the dark) of the QW FET in split-gate operation at various values of the finger gate bias with respect to the drain. A, B, C, and D indicate operating points for the FIR response measurements shown in Fig. 2(a). Inset: schematic plan view of the QW FET split-gate configuration (not to scale).

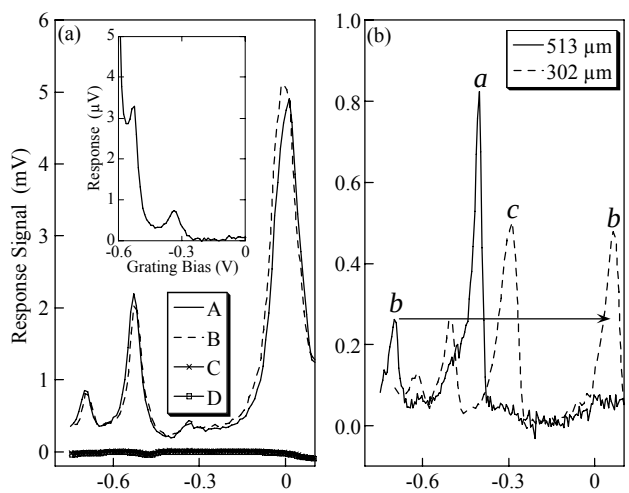

Figure 2. (a) FIR response to 432 μm as a function of grating gate bias in the two operating modes. Inset shows response in single-gate mode. Main figure shows operation in split-gate mode with finger bias = –1.07 V. The curves A. B. C. and D correspond to the source-drain dc operating biases shown in Fig. 1. (b) FIR response of the same device in split-gate mode to 513 and 302 μm. Peak labels *a, b, c* indicate the harmonic mode to which each peak corresponds as mapped out in Fig. 3 inset. The arrow indicates how the *b* mode peak moves as wavelength is decreased.

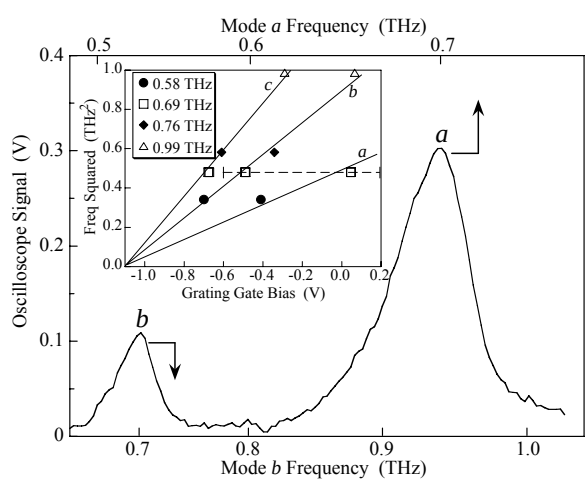

Figure 3. Inset: Plasmon mode map showing how resonances fit to the dispersion relation of (1). The line fits *a, b,* and *c* group the data into three modes. The dashed line indicates the range of the gate bias sweep used to generate the main figure, which covers two 432 μm modes. Frequency scales in the main figure are obtained from gate bias via the slopes of the *a* and *b* lines. Main: Spectrum of two plasmon modes excited by 432 μm light. The grating gate was swept from –0.6 to +0.2 V in 12.5 ms. The peak labeled *a* corresponds to the *a* line of the inset and uses the upper frequency scale, while the peak labeled *b* corresponds to the *b* line of the inset and uses the lower frequency scale.

Microelectronic Terahertz Receiver / Transceiver

by **Mark Lee, Michael C. Wanke, and John L. Reno**

Motivation—The "unconventional" terahertz (THz) electromagnetic spectrum between microwaves and infrared offers unprecedented, disruptive advantages for national security, defense, scientific, and industrial missions. However, THz technology infrastructure still remains immature compared to microwave electronics and infrared photonics. A central component of THz technology, a heterodyne receiver or transceiver, has until now relied on large, expensive, high-maintenance molecular gas tube lasers to supply coherent THz radiation with sufficient power. Clearly any widely practical THz system requires a semiconductor-based microelectronic technology instead. Only recently has this become feasible with the invention of high-power microelectronic THz quantum cascade lasers (QCLs), in which Sandia played a major role. THz QCLs are currently the only solid-state sources of coherent THz radiation with > 1 mW of continuous power. However, it remains to be seen whether the power, mode structure, and noise/stability characteristics of QCLs are sufficiently good that they can serve as useful local oscillators (LOs) and/or coherent illumination sources with microelectronic THz mixers to form an all-solid-state THz receiver or transceiver.

Accomplishments—To test whether a THz QCL can work as an LO source with a solid-state THz mixer we had to develop both a QCL and a semiconductor mixer with compatible frequency ranges and power characteristics. To this end, 2.8 THz QCLs were successfully grown by molecular-beam epitaxy, fabricated, and tested at Sandia to be used as the microelectronic THz LO source. It was estimated that these lasers output between 1 and 2 mW continuous power.

On the mixer end, a Schottky diode mixer that works at the QCL frequency was successfully designed and fabricated through collaboration with NASA's Jet Propulsion Lab at Cal Tech. A photo of the mixer is shown in Fig. 1. This mixer operates from 2.5 to at least 3.1 THz (defined by the LO source frequency) with excellent low-noise characteristics. To achieve optimal noise figure requires 5 to 8 mW of power from an LO source.

Initial tests of how well the QCL operates with the Schottky mixer showed that the mixer can generate a difference frequency signal between two closely spaced coherent modes of the QCL, see Fig. 2. This indicates that the QCL outputs enough power to cause the Schottky to mix with reasonable conversion efficiency. Because the intrinsic linewidth of the Schottky response is very sharp, the Schottky was also used to determine that the linewidth of the QCL is less than 10 kHz, without being stabilized. However, we have not yet been successful in coupling enough power from the QCL to the mixer to operate the mixer at its minimum noise figure.

Significance—These ongoing experiments are the first effort to explore the integration of both semiconductor microelectronic THz sources and mixer to develop a microelectronic THz heterodyne receiver / transceiver. It is highly encouraging that the Schottky mixer can mix two modes of a QCL. Additional power requirements for optimal mixer operation have been identified.

Sponsor for various phases of this work include: Laboratory Directed Research & Development

Contact: Mark Lee, Semiconductor Material & Device Sciences, Dept. 1123
Phone: (505) 844-5462, Fax: 844-3211, E-mail: mlee1@sandia.gov

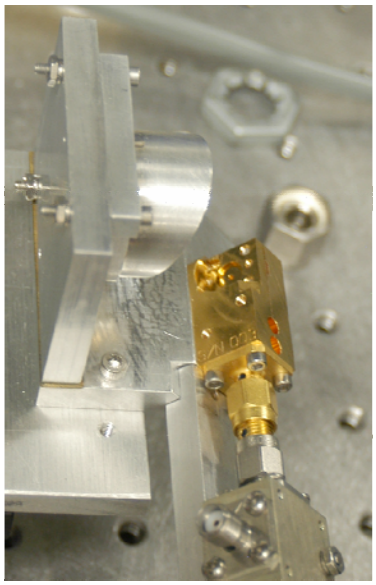

Figure 1. Photo of the Schottky mixer. The actual mixer diode is housed inside the gold-colored block. This mixer block faces an aluminum coupling mirror (approximately 1 inch diameter) that focuses THz light from the QCL LO source into the mixer block. The component below the mixer block supplies electrical bias to the mixer.

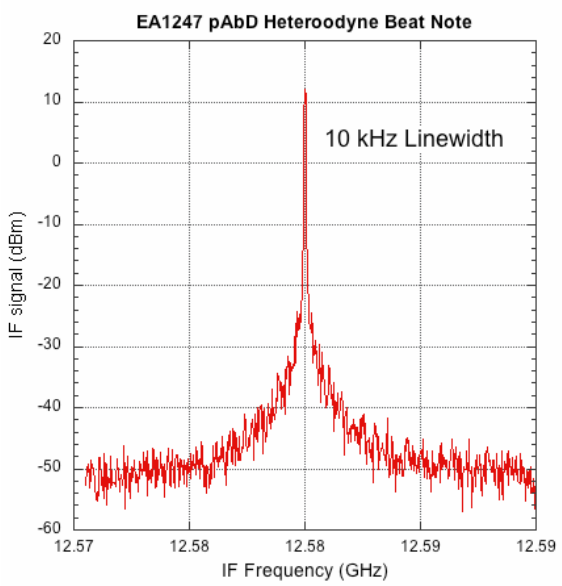

Figure 2. Schottky mixer signal showing the down-converted 12.58 GHz difference frequency between two modes of the 2.8 THz QCL. The width of the mixer signal peak indicates that the QCL output linewidth is no broader than 10 kHz.

Materials in Extreme Environments

Using Large-Scale Simulations to Advance Understanding of Defects in Silicon

by **A. F. Wright and N. A. Modine**

Motivation—When the Sandia Pulsed Reactor (SPR-III) is decommissioned in 2006, a considerable gap will exist between the threat environment for which electronic components in nuclear weapons must be qualified and available testing environments. To bridge this gap, the Qualification Alternatives to the Sandia Pulsed Reactor (QASPR) program is developing new modeling capabilities that will be used in concert with experiments to qualify weapons. The goals of the QASPR program are ambitious in that the response of complicated circuits to neutron and gamma irradiation must be accurately predicted at short time scales. This requires, among other things, a thorough scientific understanding of the behavior of the defects generated in silicon (Si) devices during neutron irradiation.

Accomplishment—We have used density-functional theory to compute the energy levels and diffusion activation energies of the silicon vacancy and self-interstitial. In the calculations, periodic boundary conditions are applied to a supercell containing a defect surrounded by bulk material, effectively producing an infinite, periodic array of defects. The use of periodic boundary conditions yields an efficient computational scheme, however it also introduces spurious electrostatic and strain interactions, between the defect and its periodic replicas, which are difficult to quantify and may vary significantly with the size of the supercell. To remove these spurious interactions, we perform calculations in three different sized supercells and extrapolate the results to an infinite sized supercell. The calculations are performed in nominal 216-, 512-, and 1000-atom supercells and the results are then fit to the equation

$$E^f\left[D^q;L\right] = E^f\left[D^q;L\to\infty\right] - \frac{\alpha q^2}{\varepsilon L} + \frac{A_3}{L^3} \qquad (1)$$

where $E^f\left[D^q;L\right]$ is the formation energy of defect D^q in the supercell with length L, $E^f\left[D^q;L\to\infty\right]$ is the formation energy in an infinite sized supercell (determined from the fit), α is a Madelung constant, ε is the static dielectric constant of Si, and A_3 is the coefficient determined from the fit.

The fits of the supercell data to Eqn. 1 are very good as illustrated in Fig. 1. We have also examined how the results depended on two different forms of exchange and correlation; the local-density approximation (LDA) and the generalized-gradient approximation (GGA). In agreement with experimental results, the GGA yields a vacancy configuration with C_{2v} symmetry in the –1 charge state, whereas the LDA yields D_{3d} symmetry. Furthermore, the experimentally observed negative-U behavior of vacancy donor states is reproduced in the GGA results, but not in the LDA results. Both the LDA and GGA predict negative-U behavior for the vacancy acceptor states.

The formation energies of stable self-interstitial structures and the activation energies for transitions between these structures have been used as input to a Kinetic Monte-Carlo code, which is used to determine the diffusion rates as a function of temperature and carrier concentrations. For non-equilibrium carrier concentrations, fluctuations in the charge state of the self-interstitial lead to non-Arrhenius behavior via a modified Bourgoin-Corbett mechanism.

Significance—Developments in massively parallel software and computational techniques have enabled state-of-the-art calculations that provide key parameters critical to the future qualification of nuclear weapons components.

Sponsors for various phases of this work include: Nuclear Weapons/Qualification Alternatives to the Sandia Pulsed Reactor (QASPR) and Advanced Simulation & Computing (ASC)

Contact: Alan F. Wright, Nanostructure and Semiconductor Physics, Dept. 1112
Phone: (505) 845-0445, Fax: (505) 844-1197, E-mail: afwrigh@sandia.gov

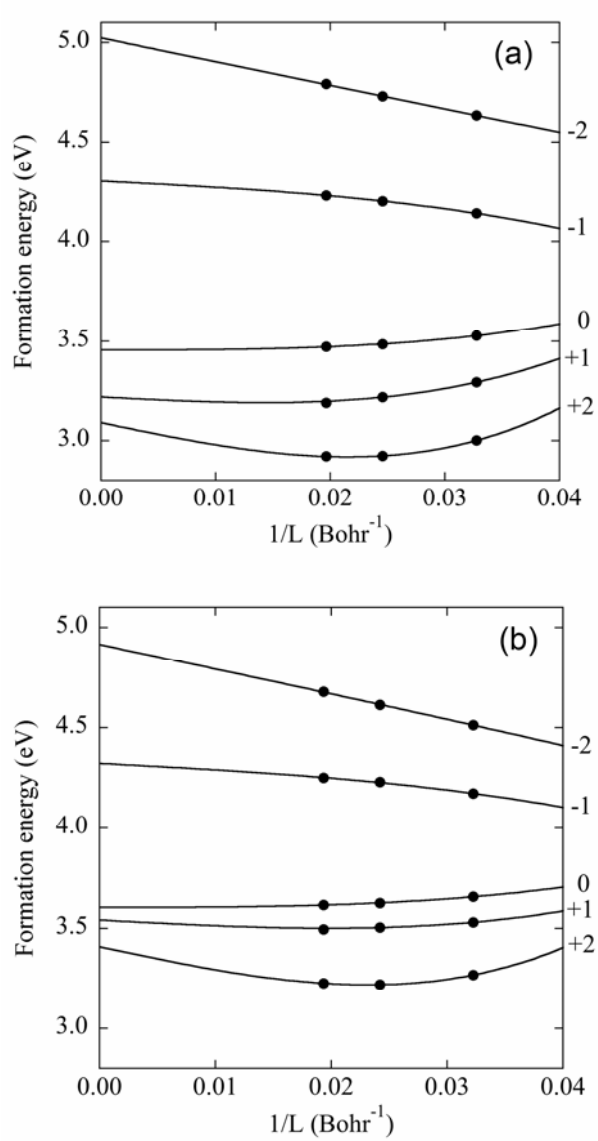

Figure 1. Plots of Si vacancy formation energies (in eV) versus 1/*L* (Bohr^{-1}) where *L* is the cubed root of the supercell volume. Filled circles indicate the formation energies computed in 215-, 511-, and 999-atom supercells. Lines show fits of the supercell data to Eqn. 1. The charge states, *q*, are given along the right side of the plot. a) Results obtained using the LDA. b) Results obtained using the GGA.

Measurements of Defects in Neutron-Irradiated Silicon Bipolar Transistors Using Capacitance Spectroscopy

by **R. M. Fleming, C. H. Seager and D. V. Lang**

Motivation—A central concept of the Qualification Alternatives to the Sandia Pulsed Reactor (QASPR) program is to establish a "damage equivalence" that allows one to model a device's response to fast neutrons from the Sandia Pulsed Reactor (SPR) by measuring its response in alternative radiation sources, e.g., ion beams. The development of high fidelity models requires input from experimental measurements of displacement-defect levels in devices irradiated in all facilities, both SPR and alternative sources. The requirements of QASPR are particularly challenging in that data are needed at short times after neutron irradiation, data on actual devices (here silicon bipolar transistors) with high neutron damage levels that produce clusters of damage rather than uniform damage. To meet these challenges we have developed a suite of measurement and analysis techniques used after in-situ, low-temperature irradiation including deep-level transient spectroscopy (DLTS), thermally stimulated capacitance spectroscopy (TSCAP) and capacitance-voltage (CV) measurements.

Accomplishment—An experimental measure of the number of defects as a function of time after neutron damage is not possible on the desired time scales. We mitigate this difficulty by performing isochronal anneals after neutron irradiation at 5 K, using the changes in defects as a function of annealing temperature to understand the time dependence at room temperature. An example of an isochronal annealing sequence of an npn 2N2222 collector after neutron irradiation at SPR is shown in Fig. 1 where we show several DLTS spectra (proportional to the numbers of defects) after annealing steps between 130 K and 500 K. Each peak in the DLTS spectrum corresponds to a trap within the silicon band gap with deeper traps appearing at higher temperatures. The di-vacancy trap (VV), which has two charge states and peaks at both 134 and 233 K, and the vacancy-phosphorus (VP) trap at 233 K are prominent. Note that the 134 K VV trap shows growth, particularly after the 353 K anneal, that we ascribe to changes in the amount of charge within a cluster. Models have indicated that VP traps at the base/emitter junction are particularly important in understanding gain degradation since they act as recombination centers and increase the base current. We have measured the base current in operating transistors (both npn and pnp irradiated at the same time) following isochronal anneals above room temperature. The results are shown in Fig. 2 along with a normalized plot of the number of VP defects measured in the collector of an npn transistor. The scaling of the base current recovery with the measured number of VP defects confirms the modeling results and indicates that much of the gain degradation of a silicon bipolar transistor can be ascribed to VP defects.

Significance—These data represent some of the first attempts to describe device performance starting at an atomistic level, taking into account defect clustering that is characteristic of neutron damage. The technique is a significant expansion of the DLTS technique that includes measurements at low temperature on actual devices at high damage levels. These data provide a level of detail heretofore unavailable that will enable a description of the damage equivalence between various types of radiation sources.

Sponsor for various phases of this work include: Nuclear Weapons/Qualification Alternatives to the Sandia Pulsed Reactor

Contact: Robert M. Fleming, Semiconductor Materials & Device Sciences, Dept. 1123
Phone: (505) 284-8460, Fax: (505) 844-1197, E-mail: rmflemi@sandia.gov

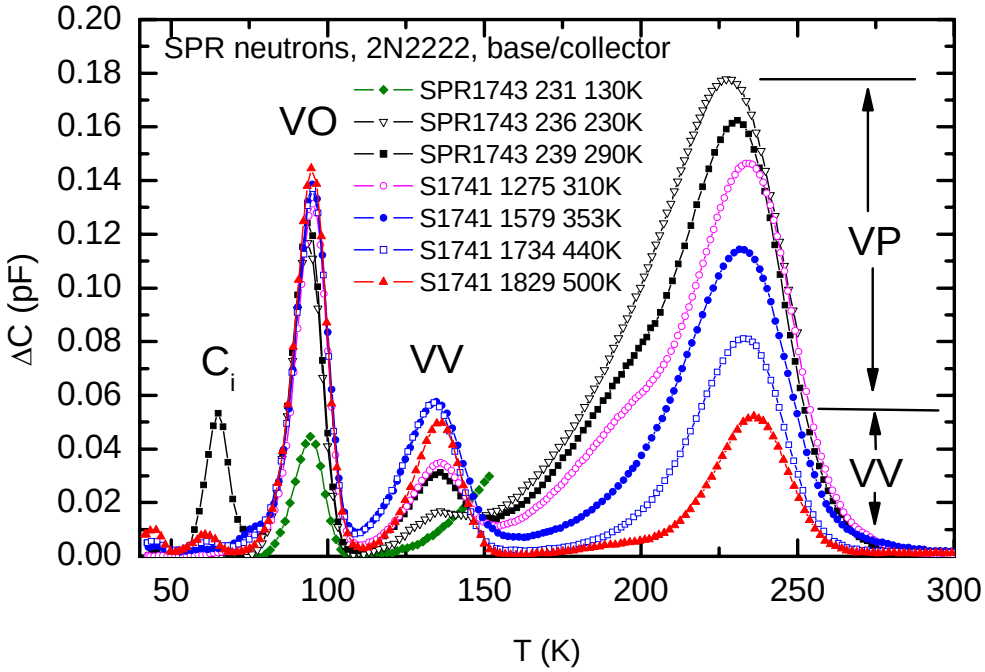

Figure 1. DLTS following 5K irradiation and isochronal anneals at the temperatures indicated. Peaks resulting from the carbon interstitial, vacancy-oxygen, vacancy-vacancy and vacancy-phosphorus defects are shown. As the device is annealed, a major change is the loss of the VP defect.

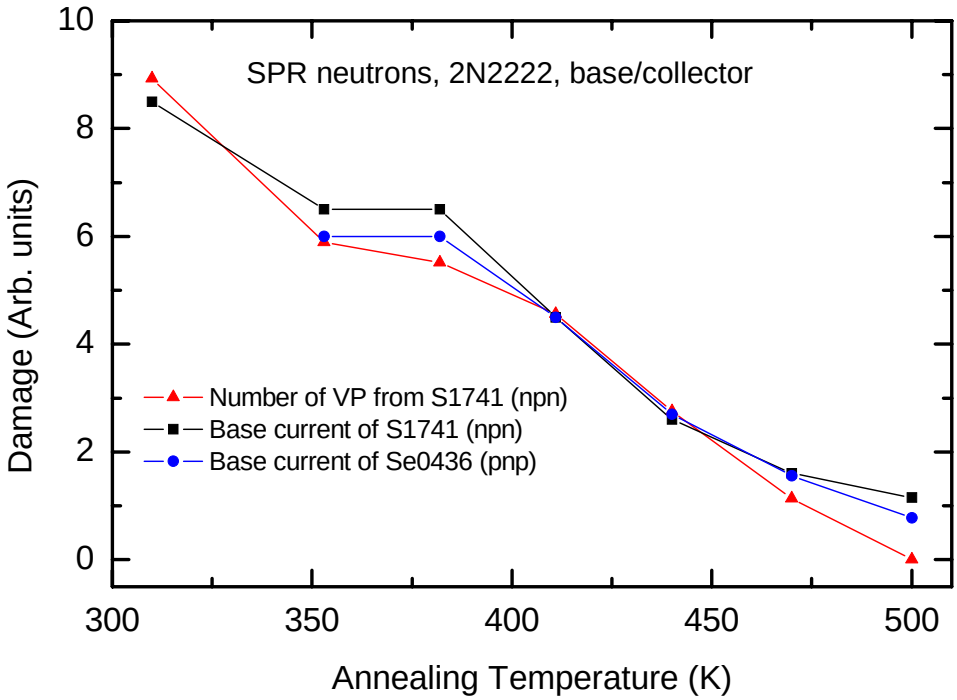

Figure 2. Damage as measured by the number of vacancy-phosphorus defects from DLTS of an npn collector as a function of annealing temperature. This indicates that the vacancy-phosphorus is a key component of gain degradation in these devices.

Modeling Neutron-Irradiated Transistors: From Atomic Collisions to Carrier Flow

by **S. M. Myers and W. R. Wampler**

Motivation—Shutdown of Sandia's SPR-III pulse reactor necessitates the qualification of electronics for transient neutron exposure via irradiation testing less representative of threat conditions. New qualification protocols are the objective of the Qualification Alternatives to the Sandia Pulsed Reactor (QASPR) program. Central to this program is the development of science-based modeling to bridge the now greater differences between accessible testing and threats. Such modeling must encompass multiple physical processes, beginning with the generation and propagation of irradiation particles, followed by the creation and time-evolution of defects and their interactions with carriers, and culminating in the altered operation of devices and circuits. Silicon bipolar transistors are most sensitive to displacement damage and hence a focus of QASPR. The greatest scientific challenge, and the subject of this brief, is the treatment of defect and carrier reactions within the Si matrix.

Accomplishment—We are developing three computational procedures to model the chain of events within the Si transistor following the creation of primal vacancies (V) and self-interstitials (Si_I) by neutron irradiation. The starting point is illustrated in Fig. 1, which shows the distribution of defects produced within a representative micrometer cube by a maximum SPR pulse, as calculated by Philip Cooper using the binary-collision Monte-Carlo code MARLOWE. The defects are concentrated in collisional cascades rather than randomly distributed, with consequences both for the time-evolution of the defects and for their interactions with carriers. Pursuant to modeling of the local behavior near such clusters, the first of the aforementioned computational procedures is to develop statistically averaged, radially symmetric concentration profiles of V and Si_I extending out to R ~ 0.5 µm. This is done by, first, evaluating V-V and Si_I-Si_I spatial pair correlation functions from the output of the Monte-Carlo MARLOWE code, and then devising radial concentration profiles with the same correlation functions. This exercise is exemplified in Fig. 1, which shows the correlation functions associated with the adjacent defect map. The resulting strongly peaked radial concentration profiles provide the basis for the second computational procedure, a continuum-model treatment of the local diffusion and reactions of the defects and the influx of carriers. The array of defect reactions is summarized in Fig. 2. The results are compared with parallel calculations for uniformly distributed defects, thereby quantifying differences that can be used to adjust the computationally much simpler uniform case. Finally, the macroscopic bipolar device is modeled for the same reaction set but without local clustering, and the above corrections for clustering are applied. These procedures are currently being refined through comparison with a wide range of QASPR model-development data. Interim results for an n-p-n transistor exposed in the fast-burst reactor at White Sands Missile Range are shown in Fig. 2, where the consistency between modeling and experiment is seen to be good. Similarly satisfactory comparisons have more recently been made for irradiations in SPR.

Significance—Sandia's modeling of neutron damage in bipolar devices was previously limited to empirical fits unsuitable for extrapolation beyond testing. The present work is a promising first step toward prediction.

Sponsor for various phases of this work include: Nuclear Weapons

Contact: Samuel M. Myers, Nanostructure & Semiconductor Physics, Dept. 1112
Phone: (505) 844-6076, Fax: (505) 844-7775, E-mail: smmyers@sandia.gov

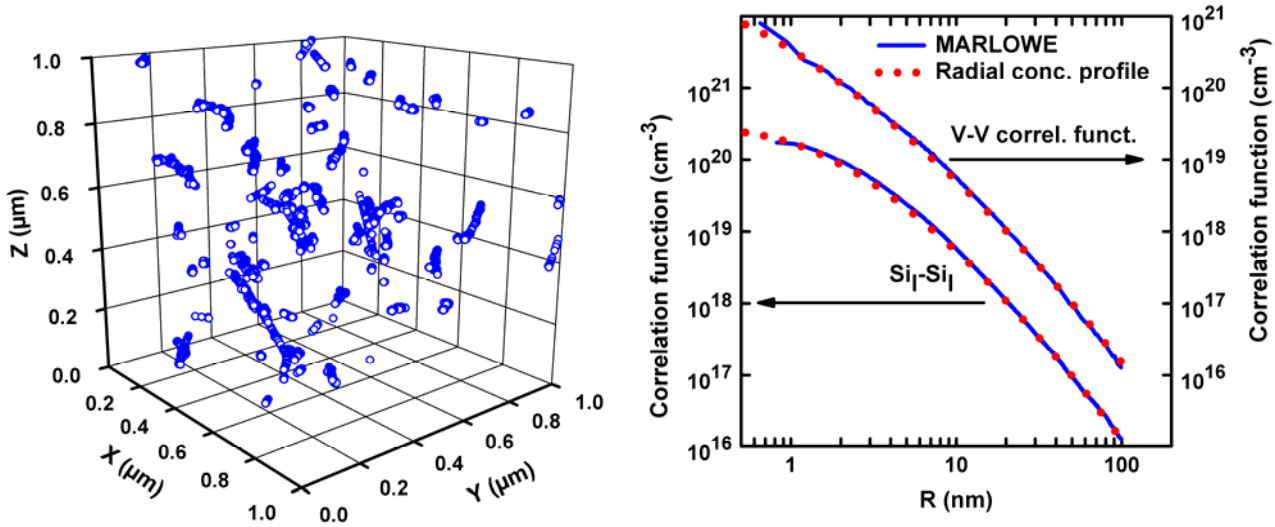

Figure 1. *Left panel*: Vacancy distribution from the MARLOWE code for the irradiation conditions of a maximum SPR pulse; the micrometer cube contains 11,330 Frenkel pairs. *Right panel*: Defect pair correlation functions from MARLOWE output and from the radial concentration profiles used to model cluster behavior; in the absence of clustering, the correlation functions are horizontal lines.

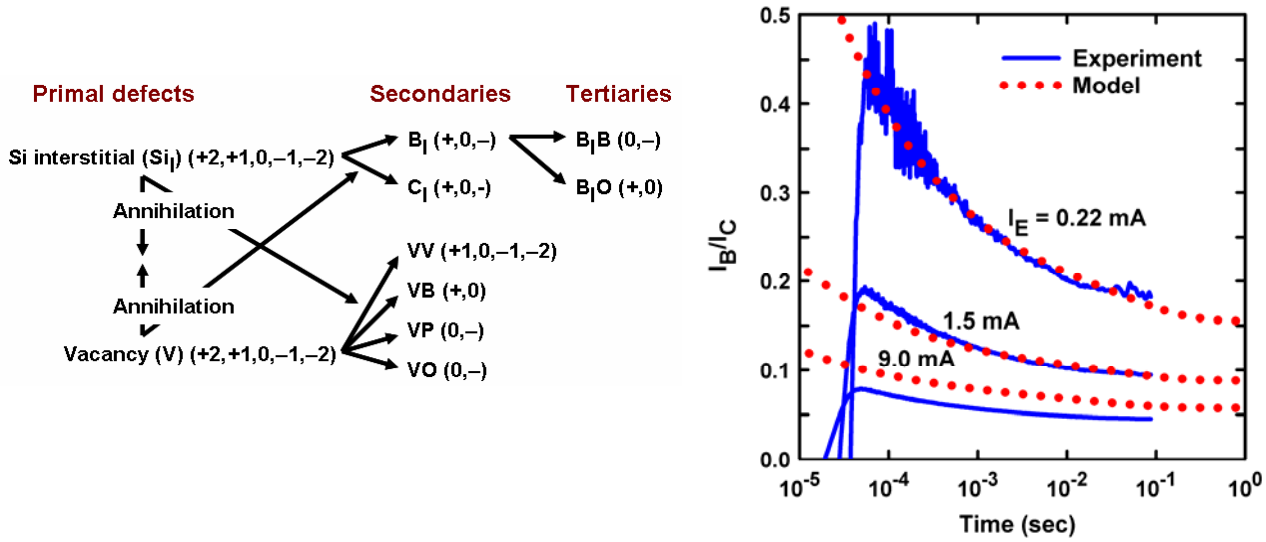

Figure 2. *Left panel*: Principal defect reactions active in Si up to room temperature, as taken from the literature and from Sandia calculations using density-functional theory; charge states are indicated in parentheses. *Right panel*: ratio of base current to collector current versus time in an n-p-n transistor following a 50 μs neutron pulse from the fast-burst reactor at White Sands Missile Range, as obtained from measurement and from the theoretical model for three emitter currents; two poorly known carrier-capture cross-sections in the model were adjusted to improve the agreement with the uppermost experimental data.

Dielectric Properties of the Lead Zirconate/Titanate Composition PZT 95/5 During Shock Compression at High Fields

***by* R. E. Setchell, S. T. Montgomery, and D. E. Cox**

Motivation—Shock-induced depoling of the ferroelectric ceramic lead zirconate/titanate composition PZT 95/5 (PZT 95/5) is utilized in pulsed power devices. High fields can be generated within a PZT 95/5 element during shock transit if the depoling current passes through an external circuit with a large resistive load. Under these conditions, a portion of the depoling current is retained on the element electrodes to account for capacitance. This effect is governed by the dielectric properties of both unshocked, normally poled material (ahead of the shock) and shocked, depoled material (behind the shock). The retained current is "lost" in terms of delivery to the external circuit, and can represent a significant fraction of the original bound charge produced when the element was poled. Previous studies have used simple models for a relaxing dielectric to predict load currents from a single, normally poled PZT 95/5 element experiencing shock transit with high field generation. However, these load currents not only reflect the combined dielectric behavior of both unshocked and shocked material simultaneously, but could be influenced by field effects on depoling kinetics.

Accomplishment—New experimental methods have been developed to better isolate dielectric properties in both unshocked and shocked PZT 95/5. We are using shock-driven circuits containing multiple, small PZT elements that are displaced both parallel and perpendicular to the shock motion. As shown in Fig. 1, this allows different elements to be subjected to uniaxial-strain shock compression and release at different times during a single experiment. Shock depoling of the first element produces a current in a circuit consisting of the second element and a load resistor in parallel, as shown in Fig. 2. Current through the load resistor produces a common voltage across both PZT elements, and a portion of the depoling current provides displacement currents to both elements as their corresponding electric fields develop. Current-viewing resistors (CVRs) measure currents in each circuit segment. In one type of experiment, the second element is an axially poled disc with a large diameter-to-thickness ratio resulting in a capacitance much larger than that of the first element. This allows the dielectric response of the second element (poled, unshocked PZT) to be accurately measured prior to shock arrival as a function of different field conditions. Figure 3 shows a comparison of measured load currents from these experiments with currents predicted using a simple model for a relaxing dielectric (Debye approximation). Some variation in the model parameters is necessary to get good agreement in each case. In a second type of experiment, the second element is a normally poled sample identical to the first. Figure 4 shows recorded currents from such an experiment. As the shock transits each element, the displacement current charging the other element is recorded as the field develops and then terminates. These experiments are providing the first direct measurements of dielectric properties in shocked, depoled PZT 95/5.

Significance—Improved understanding of dynamic dielectric properties is required for further development of predictive models for the electrical response of PZT 95/5. Our experiments are providing measurements that will enable dielectric response models that account for more than field-independent, simple relaxation to be developed and assessed. Future experiments using the new configurations will include initial temperature effects.

Sponsors for various phases of this work include: Nuclear Weapons/Dynamical Materials Properties Campaign

Contact: Robert E. Setchell, Radiation-Solid Interactions, Dept. 1111
Phone: (505) 844-3847, Fax: (505) 844-7745, E-mail: resetch@sandia.gov

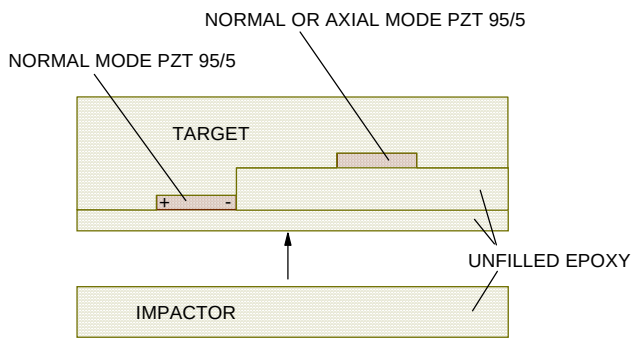

Figure 1. Configuration used for gas-gun experiments to investigate the dynamic dielectric properties of unshocked and shocked PZT 95/5.

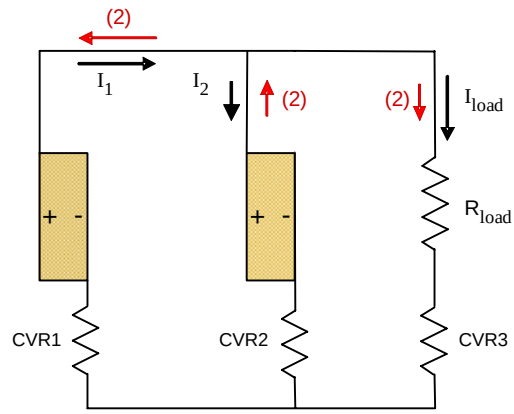

Figure 2. Electrical circuit for PZT 95/5 dielectric measurements. Red arrows indicate current flow when the shock transits the second element.

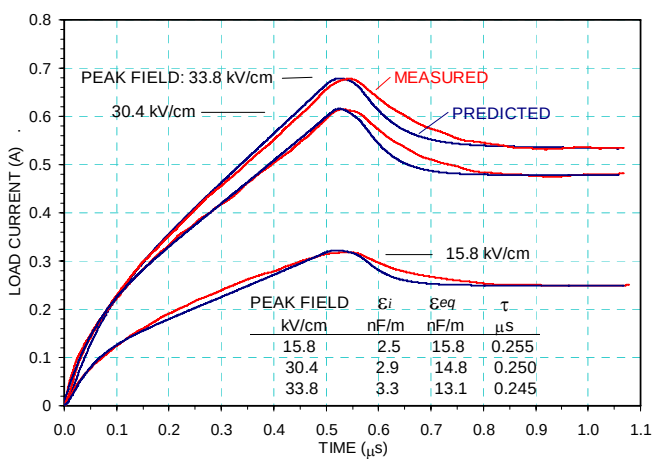

Figure 3. Comparisons between measured load currents in experiments using axial mode second elements and corresponding currents predicted using a simple model for a relaxing dielectric.

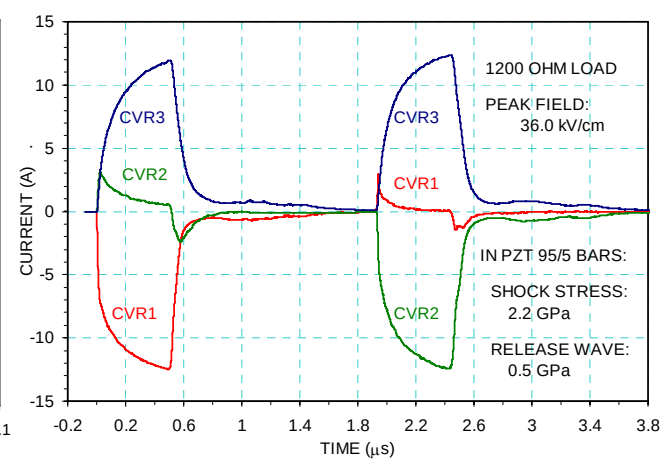

Figure 4. Measured currents in an experiment using identical, normally poled first and second elements. Currents generated during shock transit in the second element provide direct measurements of dielectric properties in PZT 95/5 that has been shocked then unloaded.

Ion Beam Induced (IBIC) Studies of SiGe Heterojunction Bipolar Transistors (HBTs)

by **G. Vizkelethy, R. A. Reed[*], P. W. Marshall[+], and J. A. Pellish[*]**

Motivation—SiGe HBTs are potential candidates for parts used in space vehicles. The performance of these devices is comparable to III-V devices. At the same time these devices are compatible with today's standard Si technology. As a bonus they are inherently radiation hard concerning total dose effects. Unfortunately, SiGe HBTs were found to be susceptible to Single Event Effects (SEEs). Broad beam tests found the SEE cross section to be significantly larger than the active device area. IBIC is an ideal tool to determine the source of this high cross section.

Accomplishment—At the Sandia nuclear microbeam facility we conducted a series of IBIC tests on SiGe HBTs from different vendors using a 36 MeV oxygen beam focused to 1 μm^2. The collector, the base, and the emitter were kept at 0 V while the substrate was set to 5 V to simulate the worst case scenario. The induced charge on all four electrodes was measured simultaneously with the *x* and *y* coordinates of the ion hit. Figures 1a and 1b show the 2D charge induction maps of the collector and the base electrodes. The charge induction map of the substrate electrode was very similar to that for the collector, while there was no detectable signal on the emitter. The collector map shows a very well defined high charge collection area, which coincides with the size and location of the deep trench isolation area. The base map shows a lower, but still well defined area, which is the shape and size of the p-type SiGe base. In addition, the collector map shows a much larger, lower charge induction area surrounding the active area in a shape of an ellipse. To interpret these images we need to apply the Gunn-theorem to the device structure shown in Fig. 2. According to the Gunn-theorem, in order to induce current in an electrode, the charge carriers have to move in a region where the electric field changes when the voltage changes on that electrode. Now it is obvious why we did not detect a signal from the emitter. A voltage change on the emitter does not change the electric field in the device apart from a tiny region under the emitter electrode. On the other hand, the change in the voltage on the base causes the field to change in the junction between the p-type SiGe base and n-type collector; changes in the collector or substrate voltage change the electric field in the full width of the device, especially at the n+p- junction at the bottom of the device. This explains the well-defined areas where the carriers drift through the fielded regions, while the charge induction from hits outside the deep trench is due to the carriers diffusing into the junction and then drifting through it.

Significance—These IBIC experiments on the SiGe HBTs prove the theory that charge induction from hits outside the deep trench isolation area is significant and can cause unexpectedly high SEE cross sections. This has led to the development of different mitigation techniques. One of them – creating a charge-blocking buried layer below the end of the trenches – promises significant reduction of the induced charge due to diffusion according to TCAD simulations. In addition, these experiments have helped calibrate and validate the TCAD codes used to simulate SiGe HBTs.

***Vanderbilt University; [+]NASA Goddard Space Flight Center**

Sponsor for various phases of this work include: Defense Threat Reduction Agency

Contact: Gyorgy Vizkelethy, Radiation-Solid Interactions, Dept. 1111
Phone: (505) 284-3120, Fax: (505) 844-7775, E-mail: gvizkel@sandial.gov

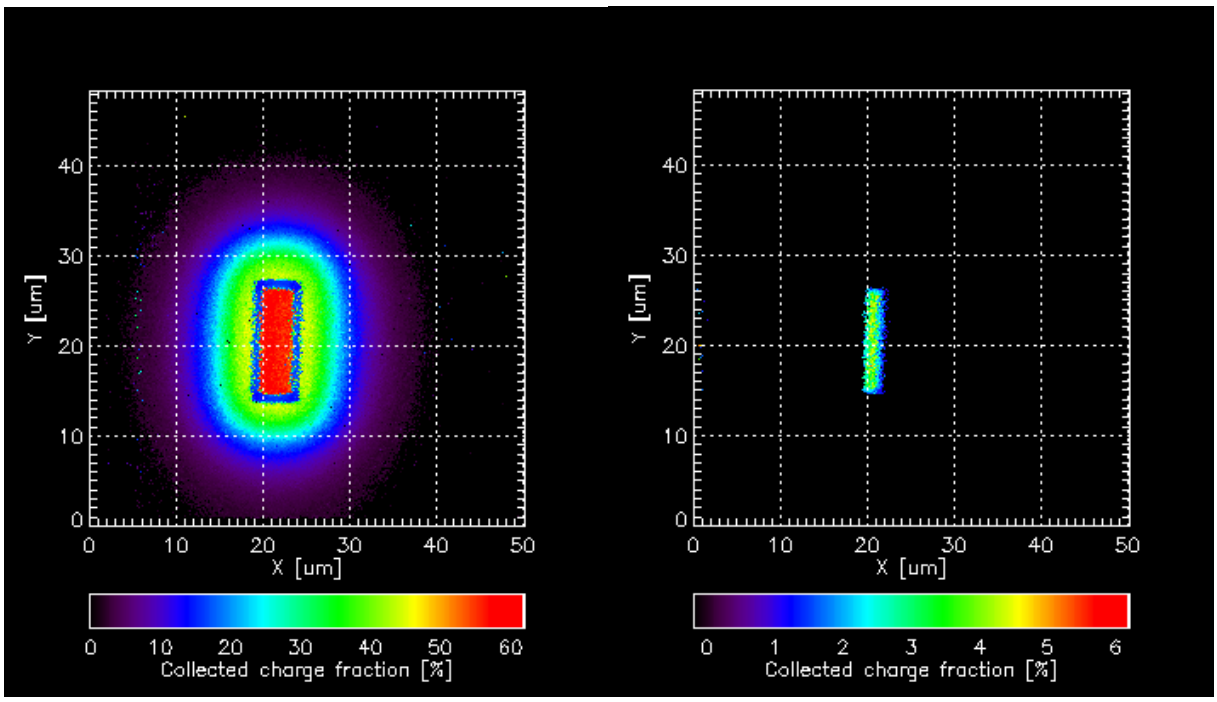

(a) (b)

Figure 1. 2D charge induction maps of the collector (a) and base (b) electrodes of SiGe HBTs.

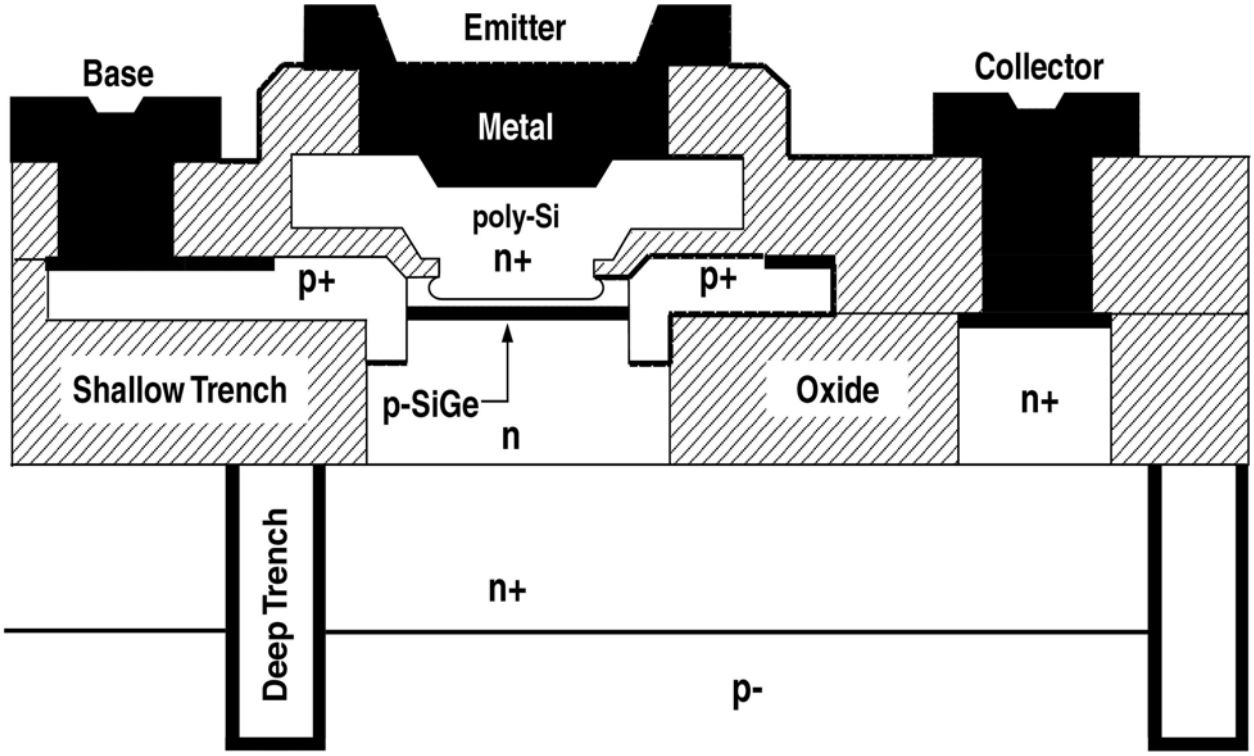

Figure 2. Cross section of a SiGe HBT (not to scale), J.D. Cressler and G. Niu, Silicon-Germanium Heterojunction Bipolar Transistors, Artech House, Boston, 2003.

The Relaxational Properties and Phase Behavior of $Pb(Sc_{0.5}Ta_{0.5})O_3$

by **E. L. Venturini and G. A. Samara**

Motivation—Many oxides with the ABO_3 perovskite structure exhibit large dielectric constants and strong electromechanical coupling. These properties arise from an easily polarized (soft) crystal lattice due to a low-frequency transverse optic phonon. Of particular interest are perovskites with chemical disorder due to mixed cations on the A sites (corners of a simple cube) or the B sites (center of the cube). One example is $Pb(Sc_{0.5}Ta_{0.5})O_3$ or PST with disordered Sc and Ta on the B site and two distinct phases, a high-temperature cubic phase with local non-cubic distortions (polar nanoregions) and a low-temperature polar or ferroelectric phase. We have employed hydrostatic pressure to better understand the dielectric response and phase behavior of PST.

Accomplishment—The size of the polar nanoregions (PNRs) and correlations between them are determined by the polarizability of the host lattice. In particular, the polarizability can increase with decreasing temperature (T), leading to larger polar regions and stronger correlations. In PST these regions reach macroscopic size at low temperature, and a spontaneous transformation to a ferroelectric (FE) state occurs. This phase transition is reflected in the dielectric constant ε′ for a PST ceramic sample versus increasing T at ambient pressure (P) shown in Fig. 1. As T increases, there is a rapid rise in ε′ near 250 K with little frequency dependence. This rise marks a transition from a FE state with macroscopic polar domains to a relaxor (R) state with dynamic PNR's and a strong frequency dependence in the dielectric constant. At higher temperatures, the thermal fluctuations in these PNRs increase, resulting in a dispersive peak (T_{max}) in ε′. The inset in Fig. 1 shows the thermal hysteresis expected in the first-order FE transition but not in the R state.

Hydrostatic P decreases the polarizability of the lattice, thus decreasing both the size of the PNR's and correlations between them and suppressing the FE transition. This suppression is shown in Fig. 2 where we compare ε′ versus increasing T at 1 bar, 4 kbar and 9 kbar. There is no evidence for a FE state at the two elevated pressures. Data at 2 kbar (not shown) show a small anomaly in ε′ (T) near 235 K, indicating that the FE transition is still present.

The phase behavior of PST is summarized on the Temperature-Pressure phase diagram in the inset of Fig. 2. Both the temperature of the ε' peak, T_{max}, in the R state (shown at 10^4 Hz) and the FE transition temperature, T_c, decrease with increasing P. The FE transition decreases at a faster rate, extending the R state over a wider T range, and completely vanishes between 2 and 4 kbar (shown as a star), allowing a continuous FE-to-R crossover (from point A to point B) without crossing a phase boundary.

Significance—The results show that the R state is the ground state of disordered PST at high P (reduced volume). The termination of a phase line at a point (the star in the inset of Fig. 2) is a very unusual feature in the phase diagram of a solid. From a thermodynamic point of view it is akin to the gas-liquid critical point for a fluid; however, in the present case it is associated with a pressure-induced FE-to-R crossover. Its existence allows one to define a path such as A-B that allows PST to undergo the crossover without crossing a phase boundary.

Sponsor for various phases of this work include: DOE Office of Basic Energy Sciences

Contact: Eugene L. Venturini, Nanostructure & Semiconductor Physics, Dept. 1112
Phone: (505) 844-7055, Fax: (505) 844-1197, E-mail: elventu@sandia.gov

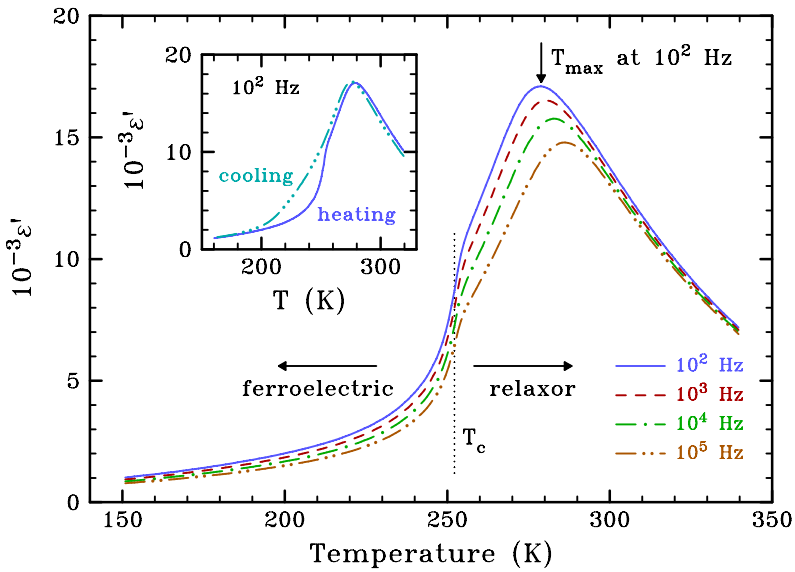

Figure 1. Dielectric data ε′ (T) measured during heating reveal a transition from a ferroelectric (FE) state below T_c (near 250 K) to a relaxor (R) state above T_c. The inset shows the thermal hysteresis expected in the first-order FE transition but not in the R state.

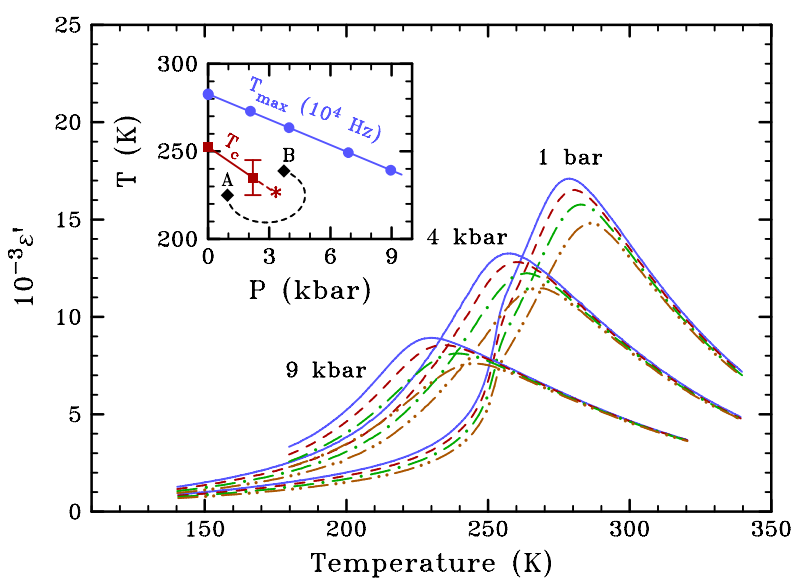

Figure 2. Hydrostatic pressure decreases ε′ (T) and suppresses the FE state. Isobaric heating data at 4 and 9 kbar show only the R state at all temperatures, in contrast to the data at 1 bar. Inset: The temperature of the ε′ peak, T_{max}, in the R state and the FE transition, T_c, during heating decrease with pressure. The FE transition vanishes between 2 and 4 kbar (indicated by a star), allowing a continuous path from point A to point B without crossing a phase boundary.

Ion-Neutron Equivalence: Ion Beam Laboratory (IBL) and Los Alamos Neutron Science Center (LANSCE)

by **E. Bielejec, G. Vizkelethy, and B. L. Doyle**

Motivation—Damage equivalence between different irradiation sources on silicon bipolar junction transistors (BJTs) has been studied for some time. Recently, there is a new demand to determine ion-to-neutron damage equivalence since pulsed nuclear reactors producing high flux short neutron pulses are becoming less and less accessible. An alternative to pulsed neutron beams is to use a pulsed ion beam that produces the same displacement damage. As a first step in this process we will establish the damage equivalency at late times, when the transistor gain is no longer changing.

Accomplishment—We report the first results of our damage equivalency studies on 2n2222 BJTs. We use the Ion Beam Laboratory (IBL) at Sandia National Laboratories to irradiate the BJTs with short, high flux ion pulses and measure the gain degradation as a function of accumulated fluence. We compare the results to similar measurements carried out with ultra-short high neutron flux pulses at the Los Alamos Neutron Science Center (LANSCE). The results are compared to calculations based on SRIM-2003. A comparison between ion irradiated and LANSCE-irradiated samples is an excellent starting point for establishing heavy ion-to-neutron damage equivalency.

In both the ion and neutron irradiations the gain of the transistor is determined from the collector and base currents continuously before and after the irradiation. Using the Messenger-Spratt equation we can relate the inverse gain degradation to the incident fluence through the damage factor (k) for each particle:

$$\frac{1}{G_{final}} - \frac{1}{G_{initial}} = k \cdot \Phi$$

where Φ is the fluence, and G_{final} and $G_{initial}$ are the final and initial gain values. Figure 1 shows the inverse gain degradation as a function of fluence for Si ion and a 12 MeV He ion irradiation (inset). All three Si curves follow the Messenger-Spratt equation, and the damage factors are calculated by a linear fit to the data sets. The 12 MeV He irradiation shows non-linear behavior at low fluence. This non-linearity is attributed to the trapped charge in the passivation and field oxide layers. This effect is noticeable for He since the ionization-to-displacement damage ratio is significantly higher for light ions than for heavy ions. The damage factors from the linear fits for the ion irradiations are then scaled by the ratio of the ion-to-neutron damage factors. This allows conversion between the measured ion fluence and an equivalent 1 MeV neutron fluence. Figure 2 shows the inverse gain degradation as a function of the calculated 1 MeV neutron equivalent fluence. The Si data sets are linear, while the He data shows super-linear behavior for low fluence and a linear response for high fluence. For high fluence, where the ionization effect is saturated, the linear response is due to displacement damage which follows the Messenger-Spratt equation.

Significance—In addition to relating the ion to neutron irradiations we have determined the ion-to-neutron equivalency by comparing the measured damage factor ratios to a calculated Non-Ionizing Energy Loss (NIEL) calculation using SRIM-2003 as seen in Fig. 2.

Sponsors for various phases of this work include: Nuclear Weapons/Readiness in Technical Base & Facilities and Laboratory Directed Research & Development

Contact: Edward Bielejec, Radiation-Solid Interactions, Department 1111
Phone: (505) 284-9256, Fax: (505) 844-7775, E-mail: esbiele@sandia.gov

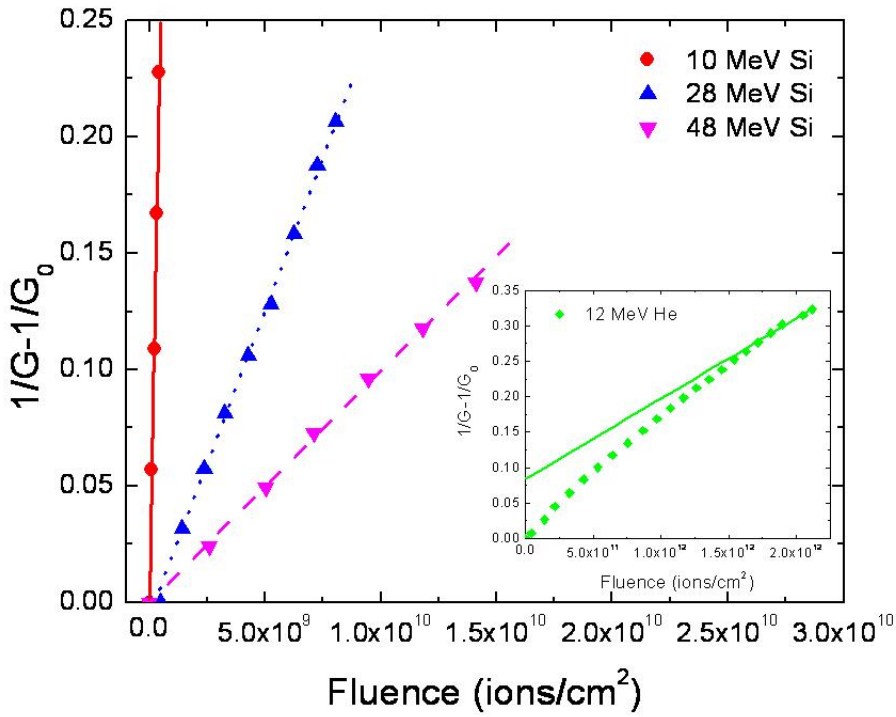

Figure 1. The linear relationship between the inverse gain degradation for three different energy Si ions as a function of fluence. Inset: The non-linear behavior of the inverse gain degradation for 12 MeV He irradiation.

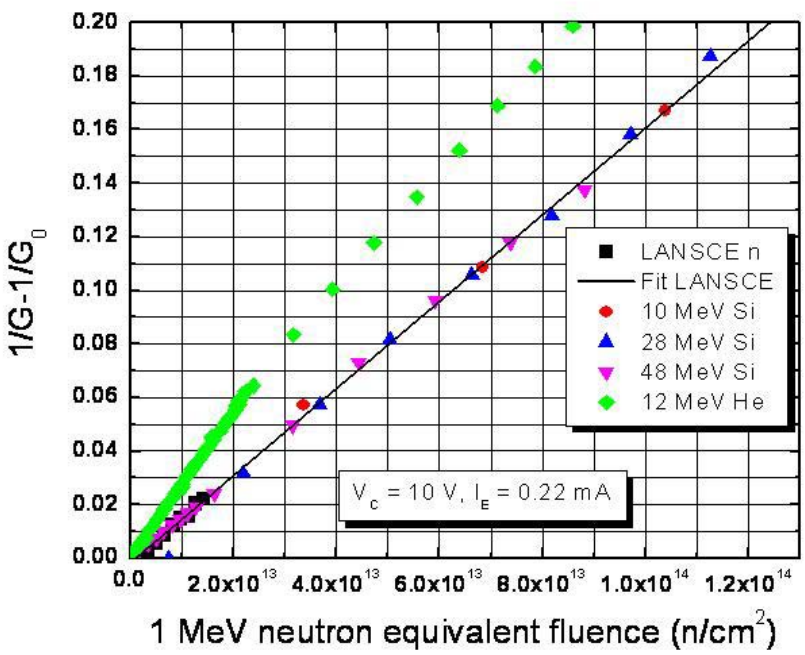

Particle	k/k_n	$NIEL/NIEL_n$
LANSCE	1	1
He (12 MeV)	70	84
Si (10 MeV)	330,000	480,000
Si (28 MeV)	18,000	22,000
Si (48 MeV)	8,100	10,000

Figure 2. Inverse gain degradation for both IBL and LANSCE irradiations as a function of 1 MeV neutron equivalent fluence. The non-linear response at low fluence for He corresponds to ionization effects. Table: Comparison of the experimentally measured damage factor ratio compared to the calculated NIEL ratio for Si and He beams.

Recent Awards & Prizes

Recent Awards & Prizes

National and International Awards

2005 — **American Academy of Arts and Sciences Election:** "For outstanding contributions in her profession." (Julia Phillips)

2004 — **National Academy of Engineering (NAE) Election:** "For leadership and distinguished research in the epitaxy of dissimilar materials." (Julia Phillips)

Other Awards

2006 — **American Physical Society (APS) Division of Atomic and Molecular Physics (DAMOP) Fellow Appointment:** "For investigations of, and contributions to, the science of atomic and molecular processes in plasmas through development of innovative optical, microwave, and rf diagnostics." (Greg Hebner)

2005 — **American Physical Society (APS) Fellow Appointment:** "For experiments advancing the understanding of electron correlation and electrodynamic response in oxide superconductors, ferromagnets, Coulomb glasses and nonlinear optical polymers." (Mark Lee)
— **Materials Research Society (MRS) "Science as Art" Competition First Prize Award:** "For Garden of ZnO Nano-Yuccas." (Julia Hsu, Tom Sounart, Neil Simmons, Jim Voigt, and Jun Liu)
— **R&D100 Award:** "For the development of Ion Photon Emission Microscope (IPEM)." (Barney L. Doyle, Michael Mellon, Floyd D. McDaniel, and Paolo Rossi)

2004 — **American Vacuum Society (AVS) Fellow Appointment:** "For developing innovative optical, microwave, and electrical diagnostics of plasma sources." (Greg Hebner)
— **Optical Society of America (OSA) Fellow Appointment:** "For contributions to the field of nonlinear optics." (Arlee V. Smith)
— **R&D100 Award**: "Cantilever Epitaxy and Growth of Low-Dislocation Gallium Nitride." (Inventors: C. I. H. Ashby, D. M. Follstaedt, C. C. Mitchell and J. Han; Developers: A. A. Allerman, K. H. A. Bogart, K. Cross, A. J. Fischer, K. Fullmer, L. Griego, D. D. Koleske, N. A. Missert, M. P. Moran, A. K. Norman, A. Ongstad, G. M. Peake, P. Provencio, and J. Sergeant)
— **Wilbur Lucius Cross Medal Recipient** – highest award of the Yale University Graduate School Alumni Association: Cited for "scientific achievements, leadership in research management, outstanding service to the nation, and inspiration as a role model for young women in science and engineering." (Julia Phillips)

2003 — **2003 President's Silver Quality Award:** "Weapon Program Phase 7 Process Development" Team. (David Walsh)

— **AAAS Fellow Appointment:** Elected Fellow of the American Association for the Advancement of Science (AAAS) for his "research advances, particularly the development and exploitation of interfacial force microscopy, leading to fundamental understanding of the interaction of solid surfaces with the environment." (Jack Houston) — **APS Fellow Appointment:** Elected Fellow of the American Physical Society (APS) "for his pioneering and continued contributions to the metal-organic chemical vapor deposition of compound semiconductors, especially strained layer superlattices and Bragg reflectors for use in optoelectronic devices for industrial applications." (Bob Biefeld)

— **Humboldt Research Award** for early experimental research on electrical discharge excimer lasers and for recent accomplishments on the microscopic theory of semiconductor lasers. (Weng Chow)

Patents Awarded

2006

— Patent 7,119,245
Title: Synthesis of an Un-supported, High-Flow ZSM-22 Zeolite Membrane
Originators: Steven G. Thoma and Tina M. Nenoff

— Patent 7,064,817
Title: A Method to Determine and Adjust the Alignment of the Transmitter and Receiver Fields of View of a LIDAR
Originators: Philip J. Hargis, Jr., Tammy D. Henson, Leslie J. Krumel, and Randal L. Schmitt

— Patent 7,041,616
Title: Enhanced Selectivity of Zeolites by Controlled Carbon Deposition
Originators: Mutlu Kartin, Tina M. Nenoff, and Steven G. Thoma

2005

— Patent 6,980,354
Title: A Self-Seeding Ring Optical Parametric Oscillator
Originators: Darrell J. Armstrong and Arlee V. Smith

— Patent 6,964,936
Title: Method of Making Maximally Dispersed Heterogeneous Catalysts
Originator: Dwight R. Jennison

— Patent 6,866,560
Title: Method for Thinning Specimen
Originators: David M. Follstaedt and Michael P. Moran

— Patent 6,844,378
Title: Method of Using Triaxial Magnetic Fields for Making Particle Structures
Originators: James E. Martin, Robert Anderson, and Rodney Williamson

2004

— Patent 6,790,476
Title: Method of Adhesion Between an Oxide Layer and a Metal Layer
Originator: Dwight Jennison

— Patent 6,775,314
Title: Distributed Bragg Reflector Using AlGaN/GaN
Originators: Stephen Lee, Karen Waldrip, and Jung Han

— Patent 6,775,054
Title: Image Rotating 4-Mirror Ring Optical Parametric Oscillator
Originators: Arlee Smith and Darrell Armstrong

— Patent 6,718,821
Title: Laser Interferometry Force-Feedback Sensor for an Interfacial Force Microscope
Originators: Jack E. Houston and William L. Smith

— Patent 6,716,275
Title: Gas Impermeable Glaze for Sealing a Porous Ceramic Surface
Originators: Tina M. Nenoff, Scott T. Reed, Ronnie G. Stone, Steven G. Thoma, and Daniel E. Trudell

— Patent 6,627,048
Title: Laser Interferometry Force-Feedback Sensor for an Interfacial Force Microscope
Originators: Jack Houston and William L. Smith

2003

— Patent No. 6,665,329
Title: Broadband Visible Light Source Based on AlInGaN Light Emitting Diodes
Originator: Mary H. Crawford

— Patent No. 6,647,034
Title: Method To Improve Optical Parametric Oscillator Beam Quality
Originator: Arlee V. Smith

— Patent No. 6,647,033
Title: Optical Parametric Oscillators with Improved Beam Quality
Originators: Arlee V. Smith and William J. Alford

— Patent 6,627,048
Title: Reductive Precipitation of Metals Photosensitized by Tin and Antimony Porphyrins
Originator: John A. Shelnutt

— Patent 6,608,846
Title: Bistable Laser with Multiple Coupled Active Verticle-Cavity Resonators
Originators: Arthur J. Fischer, Weng W. Chow, and Kent D. Choquette

— Patent 6,600,761
Title: Semiconductor Laser with Multiple Lasing Wavelengths
Originators: Arthur J. Fischer, Weng W. Chow, and Kent D. Choquette

— Patent 6,599,362
Title: Substrate Texturing for Cantilever Epitaxy of III-N and Other Materials
Originators: Carol I. Ashby, Christine C. Mitchell, David M. Follstaedt, and Jung Han (Yale University)
— Patent 6,596,254
Title: Niobate-Based Octahedral Molecular Sieves
Originators: Tina M. Nenoff and May D. Nyman
— Patent 6,570,333
Title: A Method for Generation of Surface Plasma Using Radio-frequency Power Across Pairs of Insulator Conductors where the Plasma Can Cover a Variety of Flat or Curved Surfaces, such as Aircraft Surfaces in High-altitude Flight Operation
Originators: Paul A. Miller and Ben P. Aragon
— Patent 6,567,454
Title: Coupled-resonator Vertical-cavity Lasers with Two Active Gain Regions
Originators: Arthur J. Fischer, Weng W. Chow, and Kent D. Choquette
— Patent 6,552,338
Title: Ion Photon Emission Microscope
Originator: Barney L. Doyle
— Patent 6,504,859
Title: Light Sources Based on Semiconductor Current Filaments
Originators: Weng Chow, et al.
— Patent 6,479,919
Title: Solid-state Nuclear-to-electric Energy Conversion: Beta-voltaic Cells of Icosahedral Borides
Originators: Terrence L. Aselage and David Jacob Emin
— Patent 6,406,931
Title: Conductivity Control of GaN Using LT AlN Buffer Layers
Originators: Jeffrey J. Figiel and Jung Han (Yale University)

Government Advisory Boards & Professional Societies/International Committees/Journals

Government Advisory Boards

Argonne National Laboratory

— Materials Science Division External Review Committee; Julia Phillips, Chair; 2003

Department of Energy, Office of Basic Energy Sciences

— Council of the BES Division of Materials Sciences & Engineering; Julia Phillips, member; 2006-2008
— BES Advisory Committee Subcommittee on Grand Challenges in BES; Julia Phillips, member; 2006-2007
— Workshop on Basic Research Needs for Solid State Lighting: Julia Phillips, Workshop Chair; Jerry Simmons, Panel Chair; Mary Crawford, Panel Member; 2006
— Scientific User Facilities Division Committee of Visitors; Julia Phillips, member; 2004
— Review of Nanoscience Research Center Operational Plans; Julia Phillips, member; 2004
— Materials Sciences and Engineering Program Committee of Visitors; Julia Phillips, member; 2003
— Workshop on Issues in Nanomechanics; Charles Barbour, Panel Chair; 2003

Lawrence Berkeley National Laboratory

— Accelerator and Fusion Research/Directors Review Committee; Barney Doyle, member; 2003

Lawrence Livermore National Laboratory

— Chemistry and Materials Science Directorate Review Committee; Julia Phillips, member; 2004-present

National Academy of Engineering

— U. S. Frontiers of Engineering Program: Julia Phillips, Chair, 2005-2008; Mary Crawford, participant, 2005; Julia Hsu, participant, 2003
— Draper Prize Committee; Julia Phillips, member; 2005-2007

National Research Council

— Committee on Benchmarking the Research Competitiveness of US Chemical Engineering; Julia Phillips, member; 2006
— Committee on Nanophotonics Assessability and Applicability; Jerry Simmons, member; 2006-2007
— Review Panel, National Research Council Associateship Program: Diane Peebles, Neal Shinn, and Greg Hebner, members; 2006
— Committee to Assess the Impact of the MRSEC Program; Julia Phillips, BPA liaison; 2005-2006
— National Materials Advisory Board; Julia Phillips, Chair; 2002-2004
— Board on Physics and Astronomy; Julia Phillips, member; 2000-2006

National Science Foundation

— Advisory Committee, Mathematics and Physical Sciences Directorate; Julia Phillips, member; 2000-2003

Professional Societies/International Committees/Journals

Air Force Office of Scientific Research (AFOSR)

— Plasma-assisted Combustion AFOSR Review Panel; Greg Hebner and Paul Miller, members; 2004

American Association for Crystal Growth

— 20th American Conference on Crystal Growth and Epitaxy; Sean Hearne, Symposium Chair; 2006
— Executive Committee; Bob Biefeld, member; 2005-present

American Association for the Advancement of Science (AAAS)

— Council; Julia Phillips, member; 2003-2005
— Physics Section Nominating Committee: Julia Phillips, member, 2003-2004; Chair, 2005
— Physics Section; Julia Phillips: Chair-elect, Chair, Past Chair; 2003-2005

American Chemical Society (ACS)

— COLL Division; Tina Nenoff, Councilor; 2006-2008

American Physical Society (APS)

— Division of Condensed Matter Physics (DCMP): Julia Phillips, Vice-Chair, 2005; Chair-Elect, 2006; Chair, 2007
— Forum on Industrial & Applied Physics (FIAP): Mark Lee, Vice-Chair, 2005; Chair-Elect, 2006; Chair, 2007
— Committee on Minorities; Carlos Gutierrez, Chair; 2006
— Division of Materials Physics (DMP) Executive Committee; Julia Hsu, Member-at-Large; 2004-2006
— Symposium; Brian Swartzentruber, Organizer; March 2004
— Committee on Meetings; Mark Lee, member; 2003-2006

American Vacuum Society (AVS)

— Neal Shinn, President; 2007
— 53rd International Symposium; Neal Shinn, Vice Chair; 2006
— Distinguished Lecture Series Committee; Neal Shinn, Chair; 2004-2006
— Board of Directors; Neal Shinn, member; 2003-2006
— 39th Annual Meeting of the New Mexico Chapter; Kate Bogart, Symposium Chair; 2003

ASM International - The Materials Information Society

— Events Committee; Dan Barton, member; 2003-present
— Electronic Device Failure Analysis Society (EDFAS): Dan Barton, Board of Directors member, 1998-present; Vice-President, 2005

Chemistry of Materials

— Editorial Board; Tina Nenoff, member; 2006-2009

Professional Societies/International Committees/Journals Cont'd

Conference on Magnetism and Magnetic Materials
— Scientific Advisory Board; Carlos Gutierrez, member; 2006

Electrochemical Society
— Symposium; Nancy Missert, Organizer; 2006
— Corrosion Division, Nancy Missert: Student Travel Grant Coordinator, 2005-2006; Executive Committee member and member-at-large, 2006-present
— Nash Miller Award Committee; Nancy Missert, member; 2005
— Individual Membership Committee; Nancy Missert, member; 2003-2006

Fifteenth International Conference on Crystal Growth
— Bob Biefeld, Program Co-Chair; 2006-2007

Gaseous Electronics Conference (GEC)
— 56th Annual Meeting; Greg Hebner: Chair-elect, Chair, Past Chair; 2003-2006

Gordon Conference
— Zeolite Gordon Conference; Tina Nenoff, Vice-Chair; 2008

Institute of Electrical and Electronics Engineers (IEEE)
— *Transactions on Plasma Science*, 4th issue on Images in Plasma Science; Greg Hebner, Guest Editor; 2004-2005
— *Transactions on Device and Materials Reliability (TDMR)*; Dan Barton, Guest Editor; 2002 - present
— International Reliability Physics Symposium; Dan Barton, Management Committee member; 2001-present

International Conference on Applications of Accelerators in Research and Industry
— Barney L. Doyle, Chairman; 2004, 2006

International Conference on Defects in Semiconductors
— Alan Wright; International Advisory Board, Co-organizer; 2005-2007

International Conference on Ion Beam Analysis
— Gyorgy Vizkelethy and Barney L. Doyle, Chairmen; 2003
— International Committee; Gyorgy Vizkelethy and Barney L. Doyle, members; 2003

International Conference on Low Energy Electron Microscopy/Photoemission Electron Microscopy (LEEM/PEEM)
— International Advisory Committee; Gary L. Kellogg, member; 2000-present

International Conference on Nuclear Microscopy Technology and Applications
— International Committee, Barney L. Doyle; 1990-2004

Professional Societies/International Committees/Journals Cont'd

International Conference on Particle-Induced X-Ray Emission and its Analytical Applications
— International Committee, Barney L. Doyle; 1990-2004

International Conference (4th) on Porphyrins and Phthalocyanines
— Symposium; John Shelnutt, Organizer and Chair; 2006

International Journal of PIXE (IJPIXE)
— Editorial Board, Barney Doyle; 1996-present

International Union for Vacuum Science, Technique, and Applications (IUVSTA)
— 17th International Vacuum Congress; Neal Shinn, Program Committee member; 2007
— 16th International Vacuum Congress; Neal Shinn, Program Committee member; 2004
— Surface Science Division: Neal Shinn, Chair, 2004-2007; Secretary, 2001-2004
— Surface Science Electoral College; Neal Shinn, United States Representative; 2001-2007

International Zeolite Association (IZA)
— Commission on Synthesis Committee; Tina Nenoff, member; 2004-2007

Ion Beam Modification of Materials Conference
— International Committee; Charles Barbour, member; 1996-present

Journal of Chemical Physics
— Jim Martin, Editorial Board; 2003-2006

Journal of Crystal Growth
— *Journal of Crystal Growth* for subject areas: "Epitaxial Growth and Nanostructures"; Bob Biefeld, Associate Editor; 2004-2006

Journal of Materials Research
— Editorial Advisory Board; Julia Phillips, member; 2004-present

Materials Research Society (MRS)
— Operational Oversight Committee; Julia Hsu, Treasurer and member; 2006-2007
— *MRS Bulletin*: H2 Production; Tina Nenoff, Co-Editor; October 2006
— Symposium: Neal Shinn and John Sullivan, Organizers; Spring 2006; Barney Doyle, Organizer, Fall 2005
— Meetings: Charles Barbour, Chair, Spring 2006; Julia Hsu, Chair, Fall 2004
— Board of Directors: Charles Barbour, member, 2007-2009; Julia Hsu, member, 2005-2007; Jerry Floro, member, 2002-2004
— Technical Program Committee; Julia Phillips, Chair; 2005-present
— Web Advisory Committee: Sean Hearne, member, 2005-2006; Chair, 2006-present
— Electronic Services Task Force; Sean Hearne, member; 2005
— Membership Committee: Sean Hearne, member, 2004-2006; Charles Barbour, Chairman, 2001-present

Professional Societies/International Committees/Journals Cont'd

— External Relations and Volunteer Involvement (ERVI) Committee; Jerry Floro, Chair; 2004
— Task Force on Meeting Program/Board of Directors Interactions; Julia Phillips, Chair; 2003
— Public Affairs Committee/Women in Materials Science and Engineering; Tina Nenoff, member and semi-annual organizer; 2001-2004

Microelectronics Reliability (Elsevier Journal)
— Editorial Advisory Board; Dan Barton, member; 2000 - present

Nanotechnology
— Editorial Advisory Board; John Shelnutt, member; 2005-2007

New Mexico State University
— Physics Advisory Board: Neal Shinn, member, 2004-2006; Alan Wright, member, 2002-2004, 2006

Nuclear Instruments and Methods in Physics Research, Section B: Beam Interactions with Materials and Atoms
— Editorial Board; Barney Doyle, member; 2003-2006

Pacifichem (Honolulu)
— Symposium; John Shelnutt , Organizer and Chair; 2005

Physical Review E
— Gary Grest, Senior Editor; 2002-present

Radiation Effects in Insulators Conference
— Charles Barbour, International Committee member; 1997-present

Solid State Communications
— Julia Hsu, Editorial Board; 2005-present

Texas State University
— Materials Science & Engineering Advisory Board; Carlos Gutierrez, member; 2006-2008

The Minerals, Metals, and Materials Society (TMS)
— Electronic Materials Committee: Bob Biefeld, member, 2002-present; Secretary, 2002-2004; Vice Chair, 2005-2007; Chair, 2007-2009; Past Chair, 2009-2011; Julia Hsu, member, 2000-2006
— Symposium Organizer, Sean Hearne; March 2004 meeting

Thirteenth US-Organometallic Vapor Phase Epitaxy Workshop
— Organizing Committee; Bob Biefeld, member; 2006-2007

Wessex Institute of Technology (UK)
— Scientific Committee; Frank Van Swol, member; 2006-present

Resources & Capabilities

Resources & Capabilities
Physical, Chemical, & Nano Sciences Center

— Diagnostics and Characterization —

Atomic-Level Imaging and Spectroscopy

We have developed technical capabilities in:

- Atomic Force Microscopy (AFM) for imaging, force profiling, electrical measurements, and manipulation of individual biomolecules in fluid environments with simultaneous fluorescence detection.
- Atom Probe Microscopy (APM) with pulsed laser desorption capability.
- Interfacial Force Microscopy (IFM), with ultra-sensitive laser-interferometer deflection sensing and capacitive electrostatic force feedback, which represents the first scanning probe technique available with quantitative and independent 2D force sensing. This capability allows detailed studies at the nano-meter level of adhesion, friction, and mechanical properties. The force-feedback feature enables the IFM sensor to be non-compliant, eliminating the serious "snap to contact" problems found in all present interfacial-force techniques (e.g., the AFM and the Surface Forces Apparatus).
- Piezoelectric force microscopy (PFM) for measuring spatial variation in piezoelectric properties, determining the piezoelectric coefficient and piezoelectric crystal orientation, and for imaging ferroelectric domains with lateral resolution in the range of tens of nanometers. The high-resolution PFM is also useful for inferring the crystal orientation on the surface of nanostructured piezoelectric materials.
- Scanning Tunneling Microscopy (STM) capabilities with the ability to track the diffusion of single atoms on surfaces. Nanomanipulator in a SEM for imaging and characterization of individual nanostructures.
- Low Energy Electron Microscopy (LEEM) with nanometer spatial resolution and real-time spectroscopic imaging capability at sample temperatures from 125K to over 1750K, with UHV access to joint Scanning Tunneling Microscopy (STM) capability.
- Field Ion Microscopy (FIM) with single atom resolution and accurate temperature control to 1 Kelvin.

Chemical Vapor Deposition (CVD)

Our experimental tools for investigating CVD include optical probes (such as reflectance-difference spectroscopy and emissivity correcting pyrometry) for gas-phase and surface processes, a range of surface analytic techniques, molecular beam methods for gas/surface kinetics, and flow visualization techniques. These tools are integrated in a unique manner with research CVD reactors and with advanced chemistry and fluid models.

Electrochemical Scanning Probe Microscopy

We have developed the ability to study nanoscale changes at surfaces during oxidation and dissolution of metal surfaces under electrochemical control using scanning tunneling microscopy and atomic force microscopy. These studies can be performed in a variety of electrolytes in order to determine the mechanisms governing passive film growth and dissolution.

Interfacial Force Microscopy Metrology

We have developed a unique wide-field scanning Interfacial Force Microscope (IFM) with calibrated force detection for the dynamic measurement of normal and lateral forces of micro-electrical-mechanical system (MEMS) components in operation. IFM measurements permit studies of static and dynamic friction behavior, contact compliance, and wear. The IFM has been recently upgraded with an enhanced sensitivity laser interferometer-based sensor (US Patent No. 6,085,581), Field-Programmable Hybrid Instrumentation, and an improved software interface.

Ion Beam Analysis

Two accelerator facilities in the Center are used for quantitative high-energy ion beam analysis of materials. These are the 2.5 MV Van de Graaff and the 6.5 MV Tandem Pelletron. Light elements (hydrogen to fluorine) are depth concentration profiled using heavy ion elastic recoil detection (ERD) and nuclear reaction analysis (NRA), while heavier elements are measured using backscattering spectrometry (e.g. RBS) and proton induced x-ray emission (PIXE). An external Micro Ion Beam Analysis (X-MIBA) capability enables multi-elemental analysis and ion irradiation of samples, which are vacuum incompatible or extraordinarily large and are currently a main component of the Center's Homeland Security program where it is being used to detect radioactive particulates and measure compositional signatures. The Nuclear Microprobe is used to study materials with 1 micron lateral resolution.

KMAP X-ray Diffractometer

Based on double crystal x-ray diffractometry in combination with position sensitive x-ray detection, our KMAP x-ray diffraction analysis is used to determine the lattice constant, strain relaxation, composition, layer orientation, and mosaic spread for a large variety of advanced epitaxial semiconductor material systems.

Lasers and Optics

We provide characterization and advanced understanding in the area of solid-state lasers and non-linear optics, especially as coherent sources of broadly tunable light in rugged, compact geometries. We also have established expertise in long-term and transient radiation effects characterization of optical materials. Capabilities include the widely used (approximately 2000 users worldwide) SNLO (Sandia Non-Linear Optics) code, which is a lab-tested code for predicting the performance of non-linear optical components. In the area of integrated optical materials, our laboratories produce new types of photosensitive materials (processing patent applied for) for directly-writeable waveguides and reconfigurable optical interconnects.

Low-Temperature Plasma Analysis

We have state-of-the-art capabilities for the analysis of low-temperature plasmas as found in commercial processing reactors. These include emission spectroscopy, electrical characterization, laser and microwave-based measurements of species concentrations, in situ electric field measurements, and others. Sandia is the only lab that combines new diagnostics, relevant process chemistries (complex mixtures), and massively parallel (MP) computer models for simulation of continuous and transient plasmas.

Materials Microcharacterization

Our capabilities in this area include optical microscopy, scanning, electron microscopy, analytical transmission electron microscopy, double crystal x-ray diffraction, ion beam analysis of materials (RBS, channeling, ERD, PIXE, NRA), Hall measurements, microcalorimetry, photoluminescence, light scattering, electronic transport, deep level spectroscopy, magnetization, and dielectric and magnetic susceptibilities.

MEMS-based Tensile Testing

We have developed the capability to perform pure uni-axial loading of metal MEMBS test structure in situ and ex situ of a TEM. The technique has been demonstrated using Al, Ni and Cu, but is applicable to a wide range of other materials.

MESA

Sandia's compound semiconductor clean room operations and associated characterization laboratories will be moving into new facilities starting in 2006. These facilities are part of the new $450 million MESA (Microsystems and Engineering Sciences Applications) complex that is currently under construction. Part of the MESA project includes a budget for upgrading equipment as well as new facilities and new,

enhanced capabilities. This complex when completed will enable a quick turnaround for innovative compound semiconductor device prototypes at Sandia. The arrangement of this facility will also encourage collaboration among diverse organizations to enable a more efficient working environment.

Nanoelectronics Laboratory

We have the capabilities for fabrication of nanoscale quantum device structures, together with capabilities for ultra-low-noise measurement of transport from 25 m Kelvin to ambient at high magnetic fields.

Optical Spectroscopy

Our capabilities in characterizing semiconductor materials by photoluminescence and magnetoluminescence extend down to low temperatures by optical laser imaging and laser microscopy, by laser excitation spectroscopy, and by the time-resolved measurements of optical emission. We also have developed a high lateral resolution, near-field scanning optical microscopy (NSOM) capability with time and frequency resolution.

Photovoltaic Device Characterization Laboratory

We have developed characterization capabilities in support of prototyping photovoltaic research. Capabilities include spectrally resolved photocurrent and photocapacitance measurements and a solar simulator for device characterization.

Radiation Effects Microscopy

We have facilities for nuclear microscopy and radiation effects microscopy based on a 6.5 MV tandem Pelletron ion accelerator and 1.9 MeV/amu Radio Frequency Quadrupole LINAC Booster. We generate ion species from hydrogen to gold for radiation effects research. The Sandia Nuclear Microprobe with micrometer size high-energy ion beams is used to microscopically study radiation effects in devices ranging from discrete transistors to state-of-the-art integrated circuits. Three advanced diagnostic techniques were invented at Sandia: Single-Event-Upset Imaging, Ion-Beam-Induced-Charge-Collection Imaging (IBICC), and time-resolved IBICC. A recent development is the Ion Electron and Ion Photon Emission Microscopes (2001 and 2005 R & D-100 Award winners), which can perform radiation microscopy using very highly ionizing particles without focusing the ion beam. Most recently we have developed a dedicated endstation to expose discrete transistors to intense pulses of high energy heavy ions (e.g., 40 MeV Si ions) to simulate and study neutron damage effects using in situ Deep Level Transient Spectroscopy (DLTS).

Scanning Cathodoluminescence Microscopy

We have developed the ability to measure and image cathodoluminescence from insulators and semiconductors on the submicron scale in order to understand how defects influence the emission of light from the ultraviolet to the visible. Individual spectra are also obtained at controlled locations in order to identify heterogeneities.

Simultaneous Measurement of H, D, and T in Materials

We have designed and implemented a new ion beam analysis (IBA) system to simultaneously measure the absolute quantities of H, D, and T in materials using an elastic recoil detection (ERD) technique. The technique uses an E-dE detector arrangement, or particle telescope, to provide for accurate separation of the H, D, and T signals. The system can also simultaneously acquire information about medium and high -Z elements in the sample using Rutherford backscattering spectrometry (RBS). Measurement of other light elements is possible using the nuclear reaction analysis (NRA) technique, which is isotope specific. The system will have an accuracy of < 2% for measuring the composition of solids.

— Synthesis and Processing —

400 keV and 300 keV Ion Implanters

These systems are equipped with a variety of sources (gas, sputter, and metal vapor). This facility provides ion species from hydrogen to bismuth that can be used for studying fundamental irradiation mechanisms and selective chemical doping in semiconductors, metals, ferroelectrics, and superconductors. The 300 keV implanter is capable of both ambient and high temperature implants up to 600°C and ion currents up to 50 micro-A.

Crystal and Thin Film Growth

Capabilities in this area include pulsed laser deposition chambers, a high vacuum metal deposition chamber, a thin film oxide deposition chamber, a diamond-like carbon deposition chamber, a hot filament chemical vapor deposition chamber, and various apparatus for single crystal growth. Our capabilities for stress relief of diamond-like carbon films and structures produced by pulsed laser deposition are not available elsewhere.

High Pressure and Shock Wave Physics and Chemistry Laboratories

Our capabilities in this area include large volume static high pressure apparatus which can be operated at temperatures ranging from 2 to 700 K and in magnetic fields, as well as gas gun and explosive loading facilities with state-of-the-art, time-resolved diagnostics. Recovery fixtures have been developed for use with the gas gun and explosive shock loading facilities that allow unique material synthesis over broad ranges of shock pressures and temperatures.

Metal-Organic Chemical Vapor Deposition (MOCVD)

We maintain research facilities with capabilities in MOCVD of III-V compound semiconductor materials including GaN-based materials and self-assembled quantum dots. These capabilities include research reactors designed specifically for studies of CVD chemistry, fluid dynamics, the development of advanced in situ diagnostics, and the development of advanced semiconductor heterostructures and devices.

Molecular Beam Epitaxy (MBE)

We have research semiconductor growth laboratories for ultra-pure and ultra-flexible MBE growth of III-V materials. In addition, we have research systems for Group IV semiconductor growth.

Soft Nanolithography

Soft nanolithography refers to patterning techniques that complement UV and electron beam lithography. These approaches avoid the chemical and radiation exposure often used in conventional lithography processing, making soft nanolithography particularly useful for bio, organic, and molecular materials. Current capabilities include micro-contact printing, nanotransfer printing, and dip-pen nanolithography.

Stress Evolution During Electrodeposition

We have developed the capability to measure stress evolution during thin film electrodeposition and have used it to measure stress during patterned and unpatterned film growth. Our studies range from fundamental mechanisms that create stress during island coalescence to materials-specific systems, such as electrodeposited Ni, Cu, Sn, Ag, and their alloys.

Synthetic Organic Laboratory

Novel surfactants and other small molecules are prepared in this laboratory via synthetic organic techniques. The laboratory is also capable of forming and characterizing self-organized structures (e.g., micelles and self-assembled monolayers) generated with the newly synthesized molecules in pure or mixed molecular systems.

— Theory and Simulation —

Ab-Initio Molecular Dynamics (AIMD)

We have custom-modified versions of existing AIMD codes that have been used to perform some of the largest scale free energy calculations of chemical reactions in the aqueous phase and in water-filled nanopores.

Chemical Processes

We have extensive capabilities, including massively-parallel computation, to model complex chemically reacting flows such as occur in chemical vapor deposition manufacturing processes. Our numerical simulations can include the coupled gas-phase and gas-surface chemistry, fluid dynamics, heat, and mass transfer to provide predictive models of a chemical process.

Low-Temperature Plasmas

We have extensive capabilities in massively parallel codes to simulate the time and space evolution of low-temperature plasmas, focusing on new theoretical techniques for achieving rapid convergence and on direct comparisons with experimental results.

Molecular Dynamics Simulation

Large scale, classical molecular dynamics simulations using the massively-parallel code LAMMPS (Large-scale Atomic/Molecular Massively Parallel Simulator) are being used to model a wide variety of systems. These classical simulations cover the length and time scale intermediate between quantum and continuum calculations. Systems of current interest include adhesion and friction in self-assembled monolayers, degradation of polymer adhesives, wetting and spreading of multi-component fluids and transport in polymer membranes for fuel cells. Modifications of the algorithm to include particle rotation and friction have been implemented to study granular materials. We have also custom-modified versions of existing Ab-Initio Molecular Dynamics (AIMD) codes that have been used to perform large scale free energy calculations of chemical reactions in the aqueous phase and in water-filled nanopores.

Monte Carlo Simulations

We have classical force field-based Monte Carlo capabilities for atomistic simulations that predict phase equilibria and the permeation of molecular species into nanopores.

Optical and Wave Propagation

We have developed advanced simulation codes for understanding wave propagation in optical parametric oscillators and amplifiers for the purpose of designing highly efficient, tunable laser sources. We also have capabilities in novel optical designs, including resonators for compact laser geometries. These capabilities are coupled to in-house micro-optics construction facilities and state-of-the-art optics testing.

Quantum Mechanics

We have developed state-of-the-art massively parallel quantum mechanics codes that utilize plane wave basis sets and either norm-conserving pseudopotentials or projector-augmented wave functions. These codes are used to develop fundamental understanding of physical phenomena and atomic processes in materials. Specific areas of interest include point defects and impurities in silicon and compound semiconductors, adsorbate interactions on surfaces, bonding at metal-oxide interfaces, and enhanced reactivity of nanoparticles. Recent advances include implementation of exact exchange within density-functional theory.

Physical, Chemical, & Nano Sciences Center - FY06 Budget

Physical, Chemical and Nano Sciences Center FY06 Budget - by Customer

Operating ($40.6M)

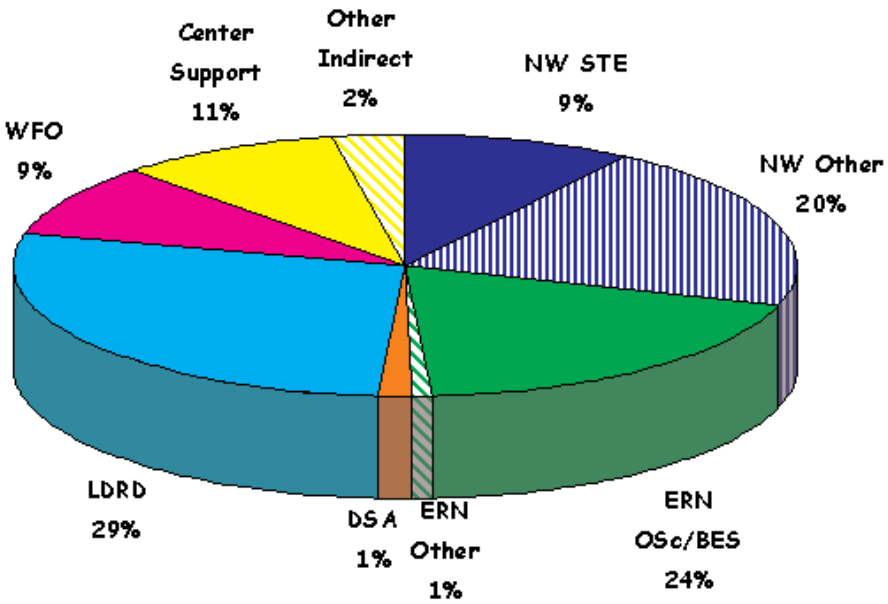

Capital ($1.6M)

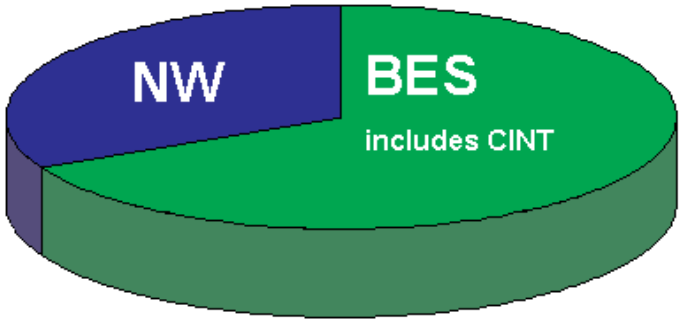

NW - Nuclear Weapons ERN - Energy, Resources & Nonproliferation DSA - Defense Systems & Assessments WFO - Work for Others
STE - Science, Technology & Engineering OSc/BES - Office of Science/Basic Energy Sciences LDRD - Laboratory Directed Research & Development

SAND2006-7502P: *Research Briefs* for the Physical, Chemical, & Nano Sciences Center is published by Sandia National Laboratories, a multiprogram laboratory operated by Sandia Corporation, a Lockheed Martin Company, for the United States National Nuclear Security Administration and the Department of Energy under Contract DE-AC04-94AL85000.

Printed 2006